Correlated Electron States in Coupled Graphene Double-layer Heterostructures

A DISSERTATION PRESENTED
BY
XIAOMENG LIU
TO
THE DEPARTMENT OF PHYSICS

IN PARTIAL FULFILLMENT OF THE REQUIREMENTS
FOR THE DEGREE OF
DOCTOR OF PHILOSOPHY
IN THE SUBJECT OF
PHYSICS

HARVARD UNIVERSITY
CAMBRIDGE, MASSACHUSETTS
October 2018

Thesis advisor: Professor Philip Kim Xiaomeng Liu

Correlated Electron States in Coupled Graphene Double-layer Heterostructures

Abstract

Graphene have grown to be a major experimental platform for studying two-dimensional (2D) physics due to its high quality, versatility and tunablity. Created by stacking graphene with other 2D materials, 2D heterostructures expand the possibility for exciting physics beyond graphene itself. This dissertation reports new phenomena observed in graphene double-layer heterostructures. In our devices, two graphene layers are placed in close proximity but separated by a thin hexagonal Boron Nitride (hBN) insulator, such that the two layers interact through Coulomb interaction while direct tunneling is prohibited.

We used Coulomb drag effect to characterize the interactions between layers as well as probe interlayer correlated phases. Experimental effort in graphene double-layer device fabrication and Coulomb drag measurements are presented. In the high temperature and weak coupling regime, we studied frictional drag effect due to interlayer Coulomb scattering. By correlating the drag signal with transport behavior of each individual layer, we furthered our understanding of magneto- and Hall-drag effect in the quantum Hall regime.

The most exciting possibility enabled by a double-layer electronic system is the exciton condensation (EC). Through Coulomb attraction, electrons in one layer and holes in the other layer bind

into interlayer excitons, which are capable of establishing Bose-Einstein condensate under low temperatures. Graphene double-layer heterostructure, being highly tunable and strongly interacting, is a perfect system to realize this exotic superfluid state. EC of quasi-electrons and quasi-holes is first achieved between two partially filled Landau levels (LLs) in the same band in bilayer graphene double-layers. By studying the EC phase transition induced by perpendicular electric field, the conditions for LLs to establish EC is acquired.

In monolayer graphene double-layers, a novel EC phase can be established between an electron-doped graphene and a hole-doped graphene with equal carrier densities. We call this state exciton insulator, as each layer is found to be insulating when the other layer is open-circuit. However, they become conducting if current is allowed to flow in the drag layer. A perfect drag current arises at the same time. This exciton insulator phase is similar to EC under zero magnetic field.

Superfluids caused by condensation of fermion pairs, such as the exciton condensate, have two distinct types: Bose-Einstein condensation (BEC) and Bardeen–Cooper–Schrieffer (BCS) condensation. Tuning interlayer coupling strength, we observed BEC-BCS crossover of the exciton condensate. In the BEC limit, tightly bound excitons pairs first form exciton gas and subsequently condense at a much lower temperatures. Oppositely, when the coupling is weak (BCS), excitons, similar to Cooper pairs in a BCS superconductor, pair and condense simultaneously. This observation provides useful insight in studying other superfluids, such as high-Tc superconductors.

With improved sample quality, more intricate interlayer correlated states at fractional filling factors arise. Some of them can be described by the integer quantum Hall effect of composite fermions (CFs), with intralayer and interlayer Chern-Simons field coupling. The others corresponding to

half integer CF fillings, are regarded as exciton condensation of CFs. Away from equal density, semi-quantized fractional Hall state, where a full CF LL couples to a continuously varying partially filled LL, can be understood by pairing of integer or fractional charged quasi-particles.

Contents

Dedicated to my parents, Li Chen and Lihong Liu.

Acknowledgments

For the past six years, I feel extremely lucky to be in a leading group and work on projects that I am truly passionate about. I am helped and inspired by many people along the way, and I made some of my best friends. My thesis would not be possible without them.

Most importantly, I owe them to my advisor Philip Kim. Philip always gave me the right amount of guidance and support while allowing me to pursuit the projects that I am interested in. Not only he offers me great independence, but he is also always there to when I need him. As busy as Philip, his door is always open, when I want to pitch him an idea, ask for suggestions or resources. Philip also built up a great atmosphere in the group. I will never forget the summer BBQ, foliage trips and Christmas parties.

I want to thank Prof. Bertrand Halperin, this thesis will be much more shallow and puzzling without him. Bert helped us understand many key discoveries and explained them to us with great patience. I really enjoyed working with him as he communicate with us using languages and intuitive pictures that we could understand.

I am thankful to Patrick Maher who mentored me and taught me a great deal when I just entered the lab. I thank Kin Chung Fong for involving me into the Coulomb drag project and educating me on cryogenics, measurements and data processing.

Thanks to Cory Dean, who pioneered graphene double-layer research in our group. My work is directly build on his early effort and we kept a good relationship whether we are working independently or collaborating. I want to thank Jia Li for working together with me on a large potion of this thesis. I enjoyed the maglab trips with you that are filled with thought-provoking discussions and exciting progresses.

Thanks to Jesse, for involving me in your project and been a really fun deskmate. Thanks to Jing, Ke, Zeyu and Eunice, for the pleasure of working closely together. Also thanks to my other collaborators: Guangxin Ni, Lei Wang, Yuanda Gao, Yuya Shimazaki. Thanks to Prof. Yacoby, Didi Wei and Monica Allen for sharing their knowledge and recipes. Thanks to Hannah Belcher and Carolyn Moore, for going beyond your job to help us. Thanks also to Kenji Watanabe and Takashi Taniguchi for providing the hBN crystal that are essential for my research.

I have met some of my best friends in our lab. I want to thank Jing, Austin, Frank, Gilho, Kate, Zeyu, Ke, Jesse, Andy, Hyobin, Katie, for the great friendships and making my past six years colorful. I also want to thank my other friends over the years: Ting Cao, Kangmei Li, Jia Guo, Jieqiang Wu, Boxin Xue, Xiaoming Yu, Zhaoyi Li, Dennis Wang, Junru Li, Kevin Jiang. During the time in the group, I also had the pleasure of knowing and interacting with Wei, Jayakanth, Mehdi, Laurel, Rebecca, Luis, Yuval, Fereshte, Didi, Hechen, Chunhui, Tony, Nicola, Young Jae, Artem, Kwabena, Hiroshi, JD, Carlos, Dmitri, Jonah and Tom.

At last, I want to thank my family, for always supporting me through my up and downs. I cannot imagine a more loving and supportive parents than my own.

Previous publications and list of authors

Results presented in Chapter 2 were published in:

> "Frictional Magneto-Coulomb Drag in Graphene Double-Layer Heterostructures". Xiaomeng Liu, Lei Wang, Kin Chung Fong, Yuanda Gao, Patrick Maher, Kenji Watanabe, Takashi Taniguchi, James Hone, Cory Dean, Philip Kim. Physical Review Letters, 119 (5), 056802 (2017).

Results presented in Chapter 3 were published in:

> "Quantum Hall drag of exciton condensate in graphene". Xiaomeng Liu, Kenji Watanabe, Takashi Taniguchi, Bertrand Halperin, Philip Kim, Nature Physics, 13, 746–750 (2017).

The following authors contributed to Chapter 4:

> Jia Li, Kenji Watanabe, Takashi Taniguchi, Cory Dean, Philip Kim.

The following authors contributed to Chapter 5:

> Jia Li, Kenji Watanabe, Takashi Taniguchi, Bertrand Halperin, Cory Dean, Philip Kim.

Results presented in Chapter 6 were posted on preprint:

> "Interlayer fractional quantum Hall effect in a coupled graphene double-layer". Xiaomeng Liu, Zeyu Hao, Kenji Watanabe, Takashi Taniguchi, Bertrand Halperin, Philip Kim, arXiv: 1810.08681 (2018).

Ph.D. is a journey, not a destination.

1

Introduction

A common misconception about physics is that it is solely about the fundamental laws. As if all elementary particles and the laws governing their motions are discovered, there would be no mystery left in the universe. However, just as P. W. Anderson put it,"More is different."[1] When we put a large number of particles together, even with the simplest interactions, complicated behavior can emerge in totally unexpected ways. Classic example of this includes superconductivity, ferro-

magnetism and quantum Hall effect. These phenomenon are not only important for the study of physics but also enables countless applications.

Just before I started my Ph.D., graphene as a novel two-dimensional (2D) material platform have been studied extensively and produced many important results[2,3,4,5,6,7,8,9,10,11]. Beyond the special properties associated with massless Dirac electron behavior, graphene are also used as a general platform for 2D physics[5,12,13,14,15,16]. Comparing with traditional two dimensional electron gases, graphene is a true two-dimensional system and has much more tunablity. Using a simple application of gate, carrier density and carrier type can be easily controlled. In bilayer graphene, even the band structure can be manipulated with dual top and bottom gates.[17,18]. At the same time, with the introduction of hexagonal Boron Nitride (hBN) encapsulation, the quality of graphene start to rival that of traditional two-dimensional electron gases[19,20]. Furthermore, stacking different 2D materials to create 2D heterostructures opens up a whole new world of possibilities[21,22]. Different layers of 2D materials can be coupled to each other through tunneling, Coulomb interaction, exchange interaction and proximity effect to enable new properties and phenomena. All these can be achieved with a unified stacking method, unlike in MBE grown heterostructures, each design requires developments of new recipes and is often subject to limitations such as material compatibility and matching lattice constants.

Just when I entered Philip's group in my first year, I was contemplating possible projects that can be enabled by 2D material heterostructures. Inspired by Cooper pairing caused by weakly attractive interaction, I thought of similar pairing and superconductivity can be stablized in a graphene double-layer. Bringing an electron-doped graphene into proximity with a hole-doped graphene, the

holes in one layer can mediate an attractive coupling between electrons in the other layer through the Coulomb interaction, similar to phonon mediated BCS superconductor. After bringing this idea to Philip, he told me there is indeed a theoretical proposed superfluid state in graphene double-layers that is called exciton condensate. Moreover, in the lab, Cory Dean, Lei Wang, Patrick Maher and Kin Chung Fong just started the study of graphene double-layer system. Although I was mainly working on the gate defined quantum point contact project at the time, KC got me involved in this effort as well. After KC had left, I took over the study, which later became my main project. Superfluids and superconductors are something that always fascinate me and I feel very lucky that I have worked on this project.

Graphene double layer is not the first electronic double-layer system being studied. Interaction driven phenomena were extensively investigated in GaAs double quantum well. Notably, exciton condensation between Landau levels has been demonstrated in this system[23]. However, due to the large interlayer separation (∼20 nm), Coulomb interaction between layers is greatly reduced. With the week interlayer interaction, the observed exciton condensation is only stable under extremely low temperatures. And people have failed to identify a clear superfluid transition in these semiconductor heterostructures. At this distance, the tunneling between layers is still quite significant, complicating the results. In graphene double-layer with hexagonal Boron Nitride as interlayer barrier, two graphene layers can be as close as 2 nm without tunneling between layers[24,25]. The strong coupling, combined with large tunablity, makes graphene double layer a ideal platform to study emergent interlayer correlated phases, such as exciton condensation.

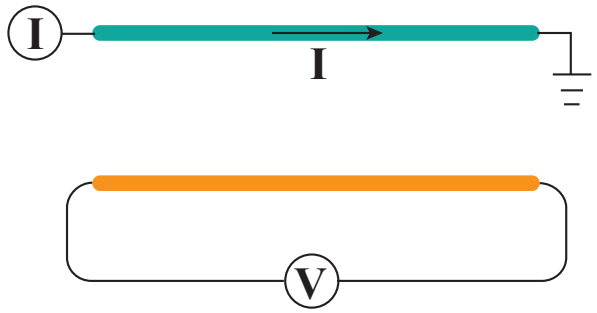

Figure 1.1: When two conductors are placed close to each other with a insulating barrier in between, driving current on the top layer (cyan) induces voltage on the bottom layer (orange).

1.1 Coulomb drag

One of the most important tool in studying a double-layer system is the Coulomb drag measurement. When two conducting layers are placed close to each other, driving current I_{drive} in one layer can induce voltage V_{drag} in the other layer. This effect is called Coulomb drag and is a result of interlayer Coulomb interaction [26]. Drag resistance is defined as the ratio between drag voltage and drive current: $R_{drag} = V_{drag}/I_{drive}$. If there is no interaction between layer, the measured drag resistance would be zero. Coulomb drag not only is useful for studying the interaction between layers, but also provide information on the electronic structure of each layer. More importantly, strong Coulomb drag effect is the smoking gun evidence for interlayer correlation when it emerges.

In the weakly coupled regime at a finite temperature T, the drag resistance $R_{drag} = V_{drag}/I_{drive}$ is typically dominated by momentum transfer through interlayer electron-electron (e-e) scattering. Driven by applied voltage, electrons moving on the drive layer transfer part of their momentum to electrons on the drag layer, causing them to move in the same direction. As the drag layer is in

open-circuit, an electrical field is developed to counter the frictional force electrons experience from interlayer Coulomb scattering. This electrical field response on the drag layer is measured as the drag resistance.

It is useful to have some qualitative understanding of how the drag resistance would behave respect to different factors in the simple case of a Fermi liquid[26]. First, the drag resistance grows with temperature T, $R_{drag} \propto T^2$, as it is proportional to the electron-electron scattering rate. The scattering rate increase with temperature due to the enlargement of the available phase space for scattering events. Second, the drag resistance is larger at lower carrier densities as it is ultimately caused by fluctuations of charge density. If the charges are uniformly distributed in both layers, they produce an uniform electrical field that generate no lateral force for drag effect. Thus the Coulomb drag effect is more pronounced when the charges are more discrete at low carrier densities. Last, the drag resistance is negative when the carrier types of both layer are the same and is positive when the carrier types of both layers are the opposite. The sign of drag is hinged on the current-momentum relationship. If the current-momentum relation is the same in both layers, the drive current will try to induce a drag current in the same direction as drive current, which must be neutralized by an electrical field in the opposite direction, thus we measure a negative drag resistance. Oppositely, if the electrical current and carrier momentum is in the same direction on one layer but in the opposite direction on the other layer, the drive current will create a opposite direction drag current, thus build up a positive drag resistance.

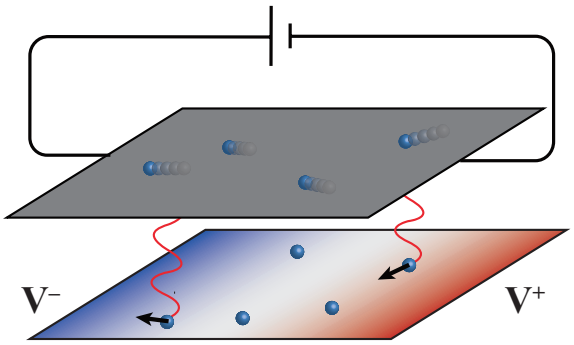

Figure 1.2: Electrons moving on the top layer transfer some of their momentum to the electrons on the bottom layer through interlayer Coulomb scattering. This kicks the electrons on the bottom layer to left side, lowering the electrical potential on the left respect to the right.

In the simple Drude model[26,27], the drag resistivity caused by this frictional drag process is

$$\rho_{drag} = \frac{m_{drag}}{e^2 n_{drive} \tau_D} \tag{1.1}$$

in which, m_{drag} is the effective mass of carriers on the drag layer, $-e$ is the electron charge, n_{drive} is carrier density on the drive layer and τ_D is the momentum transfer time, indicating how long it takes to completely transfer the momentum of electrons in one layer to the other. This is similar to the momentum relaxation time in a diffusive conductor caused by scattering. Calculating τ_D with Born approximation or Fermi-Gorden rule and plug it into eq. 1.1 gives us:

$$\rho_{drag} = \frac{\hbar}{e^2} \frac{\pi^2 \zeta(3)}{16} \frac{T^2}{E_{F1} E_{F2}} \frac{1}{\kappa_1 \kappa_2 k_{F1} k_{F2} d^4} \tag{1.2}$$

, in which $\zeta(3) \sim 1.202$ is a constant, T is the temperature, d is interlayer distance, κ_1 and κ_2

are inverse Thomas-Fermi screening length of each layer, $E_{F1}, E_{F1}, k_{F1}, k_{F2}$ are the Fermi energy and Fermi wavevector of each layers, respectively. In a Fermi liquid, eq. 1.2 applies under following conditions: (1) interlayer separation d is much smaller than mean free path, (2) d is much larger than Thomas Fermi screening length $1/\kappa$ (strong screening limit) and (3) temperature $T \ll E_F/(k_F d)$ [28,26]. This formula indeed agrees with the three conclusions we obtained from the above simple arguments.

This frictional drag effect has been experimentally studied extensively in both semiconductor double quantum wells [29,30,31] and graphene double layers [32,33]. In most cases under zero magnetic fields, the previous picture, where drag is caused by momentum transferring between Fermi liquids successfully captured the experimental observations. However there are cases where the simple theory presented above does not match measured drag signal. Most notably, in the graphene double-layer near charge neutral point, the Fermi liquid behavior does not apply. The measured drag response shows unexpected behaviors that cannot be explained by momentum drag only [32,34,35]. So energy drag picture was proposed to explain the experiments [36,37,34]. In the energy drag picture, flowing current in one layer generates a temperature gradient, which can be transfer to the drag layer to induce a drag voltage via thermoelectric effect. Coulomb drag effect under magnetic field is yet more complicated. Even in the case of drag caused by momentum transfer, the experimental findings were puzzling while little consensus was reached by theorist. The first chapter will be dedicated to the frictional drag effect under strong magnetic fields caused by momentum transferring.

1.2 Exciton condensation

Excitons are pairs of electrons and holes bound together by the Coulomb interaction. At low temperatures, excitons can form a Bose-Einstein condensate (BEC), enabling macroscopic phase coherence and superfluidity[38]. The most commonly known excitons are created by optical excitation in semiconductors. When photons hit a semiconductor, electrons are excited from the valance band to the conduction band. The excited electron can bind with the hole it left behind to form an exciton. In order to achieve condensation, a large density of excitons are needed as the BEC transition temperature is proportional to exciton density. However, optically generated excitons have short lifetimes in nano-seconds.[39] They quickly recombine and release a photon, which leads to the annihilation of excitons. While a strong continuous optical pumping is needed to keep up the exciton density, the optical excitation also heats up the sample. This makes keeping a high density of excitons under low temperatures very difficult.

One way to solve this problem is to place electrons and holes in spatially-separated parallel conducting layers, where excitons can form across the layers but cannot recombine. An electronic double layer (EDL), in which two parallel conducting layers are separated by an insulator, is an ideal platform to realize a exciton BEC without optical excitation (Fig. 1.3). Interlayer excitons formed across layers in EDLs have infinte lifetime and can be generated by electrical doping. This scheme paves a path to achieve exciton condensation in thermal equilibrium.

Beyond the benefit of infinite lifetime, the dipole-dipole repulsion between interlayer excitons can facilitate the establishment of phase coherence and keep the excitons from failing into an electron-

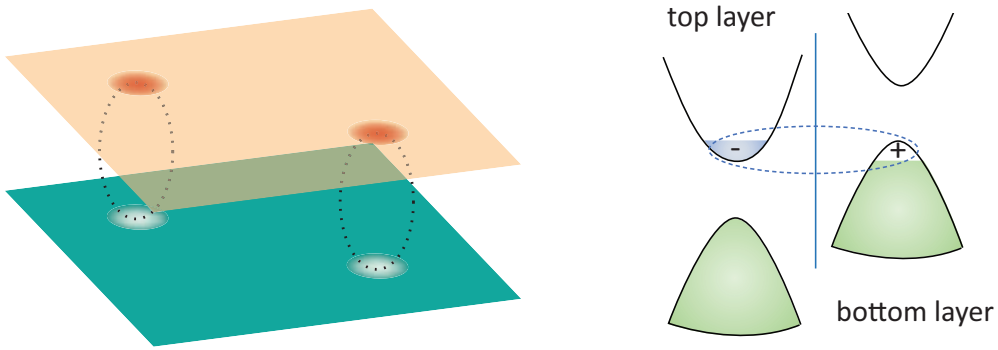

Figure 1.3: Interlayer excitons in a double-layer system. Left, illustration of interlayer exciton in real space. Electrons on the top layer bind with holes on the bottom layer by Coulomb interaction to form excitons. Right, interlayer exciton between conduction band of the top layer and valence band of the bottom layer.

hole plasma. It also provides a way to study exciton transport using electrical methods. As excitons are charge-neutral particles, they normally does not respond to electrical fields and cannot carry electrical currents. However, in a double-layer system, if there are contacts on each individual layer, interlayer excitons can carry counterflow currents, which flow in the opposite directions in the two layers. Using counterflow measurements, transport properties of excitons can be studied. When excitons form a condensate, which is a superfluid state, zero resistance of the counterflow current will be detected. This novel superfluid behavior in 2D offers potential to study many important phenomena, such as Berezinskii–Kosterlitz–Thouless transition and BEC-BCS crossover, which will be covered in Chapter 5.

Interlayer exciton under zero magnetic field was first attempted in GaAs double quantum well. Despite some anomalous drag in low temperatures, no concrete evidence of exciton condensation

have been found[40]. When graphene double-layer system arises, there was initial theory prediction of room temperature exciton condensation in monolayer graphene double-layers[41]. However, no exciton condensation was found down to 1.5K and it was found the initial theory failed to properly consider the screening effect, which reduces the transition temperature down to mK range[42]. It has also been theoretically suggested that multi-layer graphene double-layer, such as bilayer or trilayer graphene double-layers are better candidates due to their high density of states[43,44]. Experimental efforts are still being made in in this direction.

1.3 Exciton condensation between Landau levels

As higher density of states (DOS) makes interaction energy more prominent comparing with kinetic energy, large DOS usually facilitate interaction driven effects like exciton condensation. One way to generate large DOS is by applying a strong magnetic field. Under strong magnetic fields, electrons develop flatband levels called Landau levels (LLs). No surprisingly, the first experimental observation of this superfluid exciton flow was demonstrated in GaAs double quantum wells under high magnetic fields, in which strong correlation is established between electron-like and hole-like quasiparticles in quantizing orbits.

When a two-dimensional (2D) electron gas of density n is subject to a perpendicular magnetic field B, the kinetic energy of electrons is quantized to discrete LLs. Each LL contains $n_0 = eB/h$ degenerate Landau orbits per unit area, where e is electron charge and h is Planck's constant. If all the orbits in a LL are occupied (i.e., the filling factor $\nu = n/n_0$ is an integer), the 2D electron system

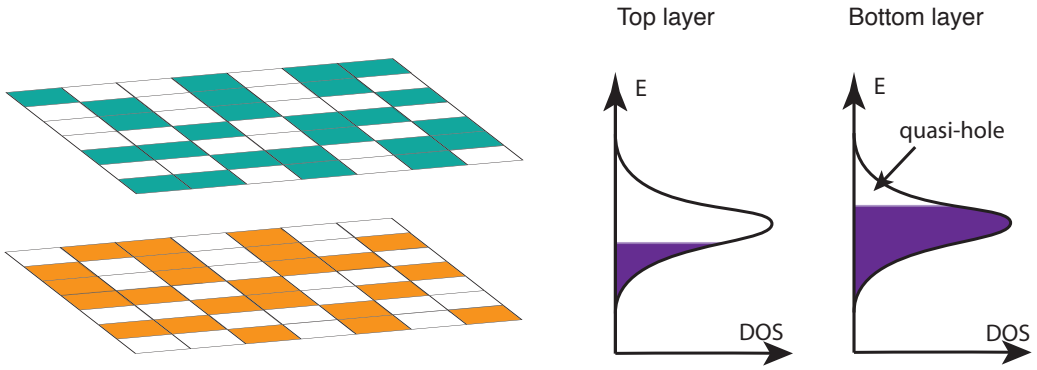

Figure 1.4: Exciton condensation between LLs. Left, the squares in each layer present degenerate Landau orbitals. In partial filled Landau levels, some of the orbitals are filled while others are empty. Because of interlayer Coulomb repulsion, a filled state on the top layer will correspond to an empty state on the bottom layer. This filled-empty state can be seen as an interlayer exciton. Right, Landau levels of double-layer. The number of filled state in one layer matches the number of empty state in the other, establish $\nu_{tot} = 1$ interlayer correlated state.

forms a quantum Hall state. In a double-layer, the filling factor of the individual layer can be specified by $\nu_{top} = n_{top}/n_0$ and $\nu_{bot} = n_{bot}/n_0$, where n_{top} and n_{bot} are the density of top and bottom layer. If LLs in both layers are partially filled, i.e., ν_{top} and ν_{bot} are non-integer numbers, neither layer can form a quantum Hall state on its own. However, Coulomb repulsion forces the electrons in the two layers to occupy different orbitals in the XY plane, leading to spatial anti-correlation between layers. When the total filling fraction, $\nu_{tot} = \nu_{top} + \nu_{bot}$, becomes an integer, the two layers together can form a coherent state in which each filled state (quasi-electron) in one layer correspond to an empty state (quasi-hole) in the other layer (Fig. 1.4). These bound empty-filled states can be described as excitons in the quantum Hall scenario.

One possible arrangement of electrons in the $\nu_{tot} = 1$ state is shown in Fig. 1.4 left. We can write

down the wave function for it.

$$|\Phi_1\rangle = c^\dagger_{T,k_1} c^\dagger_{T,k_2} c^\dagger_{B,k_3} c^\dagger_{T,k_4} ... \, |0\rangle \tag{1.3}$$

in which, $c^\dagger_{T,k_n}$ create an electron on the top layer at the nth Landau orbital. $|0\rangle$ is the vacuum state where no Landau orbital is filled in both layers. This only represent one possible configuration. However, there are many different configurations that satisfy the condition of $\nu_{tot} = 1$ and inter-layer correlation. For example, we can switch the electron on site 2 and site 3 in both layers:

$$|\Phi_2\rangle = c^\dagger_{T,k_1} c^\dagger_{B,k_2} c^\dagger_{T,k_3} c^\dagger_{T,k_4} ... \, |0\rangle \tag{1.4}$$

At equal filling $\nu_{top} = \nu_{bot} = 1/2$, adding all the possible configurations coherently, we arrive at the interlayer coherent state:

$$|\Phi\rangle = \prod_k \frac{1}{\sqrt{2}} (c^\dagger_{T,k} + e^{i\phi} c^\dagger_{B,k}) \, |0\rangle \tag{1.5}$$

In this wavefunction, k is the LL orbital index. $\prod_k$ is the product over all possible k orbital states in the Landau level. ϕ is the superfluid phase at k orbital, and represent the phase change when a electron is moved from the top layer to the bottom layer. At ground state, ϕ for the all Landau orbitals are the same, due to the weak dipole repulsion between different interlayer excitons. Similar to the number of Cooper pairs in a BCS superconductor, number of electrons in each layer does not conserve as can be seen in Eq. 1.5. This is due to electrons can fluctuate from one layer to the other when the phase is constant.

We can perform particle-hole transformation in one of the layers and change the vaccum state from $|0\rangle$ with empty LLs in both layers to $|0'\rangle$ with empty LL in the bottom layer and a full-filled LL in the top layer. The previous wavefunction becomes:

$$|\Phi\rangle = \prod_k \frac{1}{\sqrt{2}}(1 + e^{i\phi} c^\dagger_{B,k} c_{T,k}) \left|0'\right\rangle \tag{1.6}$$

$c_{T,k}$ is annihilation operator for a electron in the top layer, thus create a hole. This wavefunction highly resembles that of BCS superconductors. The only differences is that instead of creating pairs of electrons in the BCS theory, $c^\dagger_{B,k} c_{T,k}$ produces an exciton at k state with an electron on the bottom layer and a hole on the top layer.

The system can also be described equivalently by the pseudo-spin language. In this language, top layer can be treated as pseudo-spin up while bottom layer can be regarded as pseudo-spin down. When electron density of the two layers are the same, the spin up component equals spin down component in magnitude. So $\nu_{top} = \nu_{bot} = 1/2$ state is a pseudo-spin ferromagnet with polarization direction in the XY plane. The wavefunction can be transformed from Eq. 1.5:

$$|\Phi\rangle = \prod_k \frac{1}{\sqrt{2}}(|\uparrow\rangle + e^{i\phi} |\downarrow\rangle) |0\rangle \tag{1.7}$$

When the filling factors of two layers are different, the pseudo-spin will be out of plane.

Then, we consider presentation of the many body wavefunction of $\nu_{tot} = 1$ in the real space.

The many body wavefunction of a single layer quantum Hall system on the lowest Landau level is

$$\langle z_1, z_2 ... z_N | \Phi \rangle = \frac{1}{\sqrt{N!}} \begin{vmatrix} \phi_0(z_1) & \phi_1(z_1) & \cdots & \phi_{N-1}(z_1) \\ \phi_0(z_2) & \phi_1(z_2) & \cdots & \phi_{N-1}(z_2) \\ \vdots & \vdots & \ddots & \vdots \\ \phi_0(z_N) & \phi_1(z_N) & \cdots & \phi_{N-1}(z_N) \end{vmatrix} \tag{1.8}$$

in which $z_j = x_j + iy_j$ is the complex coordinate of the jth electron and $\phi_i(z)$ is the single particle wavefunction of ith Landau orbital. For the lowest Landau level under symmetric gauge (when z is defined with unit of magnetic length l_B),

$$\phi_i(z) \propto z^i e^{-|z|^2/4} \tag{1.9}$$

i is the angular momentum quantum number of the specific Landau orbital. Combining eq. 1.8 and eq. 1.9, we achieve:

$$\langle z_1, z_2 ... z_N | \Phi \rangle \propto \begin{vmatrix} 1 & z_1 & \cdots & z_1^{N-1} \\ 1 & z_2 & \cdots & z_2^{N-1} \\ \vdots & \vdots & \ddots & \vdots \\ 1 & z_N & \cdots & z_N^{N-1} \end{vmatrix} e^{-\Sigma_{i=1}^N |z_i|^2/4} \propto \prod_{i<j} (z_i - z_j) e^{-\Sigma_{i=1}^N |z_i|^2/4} \tag{1.10}$$

z_i and z_j are coordinates for two different electrons. In eq. 1.11, we can see the wavefunction vanishes when two electrons occupy the same orbital state, which is due to Pauli exclusion principle. In

double-layer structure, the electron on top layer also try to avoid the electrons on the bottom layer, not due to Pauli exclusion but due to Coulomb repulsion. So we can guess a wavefunction that vanishes when electrons on the top layer and electrons on the bottom layer coincide: $|\Phi\rangle \propto (z_i - w_j)$, where z and w are coordinates of electrons in the top layer and bottom layer, respectively. We can write down the wavefunction in a similar way as eq. 1.11:

$$\langle z_1, z_2 ... z_N | \Phi \rangle \propto \Pi(z_i - z_j)\Pi(z_i - w_j)\Pi(w_i - w_j)e^{-\frac{1}{4}\Sigma|z_i|^2 + |w_i|^2} \tag{1.11}$$

This is called the Halperin (111) state, where 111 denote the power on the three terms[45]. It vanishes when two electrons in either layer coincide in the same place, due to Pauli exclusion and Coulomb interaction.

There are many experimental methods used to study in the $\nu_{tot} = 1$ state. The most prominent ones are show in Fig. 1.5. The tunneling experiment measures tunnel current between two conducting layers through the barrier. This could be done in a electronic double-layer system with a weak tunneling barrier, such as GaAs double quantum wells. When a condensate is formed, current can flow between layers freely without the application of a bias voltage. This produces a zero-bias peak in the dI/dV measurements[46]. This resonant tunneling behavior is an analogy to Josephson effect of superconductors, manifesting the phase coherence.

Coulomb drag measurements, on the other hand, directly probe the interlayer correlation. Normally, frictional drag effect is very small and vanishes at low temperature. However, when the $\nu_{tot} = 1$ state is present, a very strong drag signal in the direction perpendicular to drive current

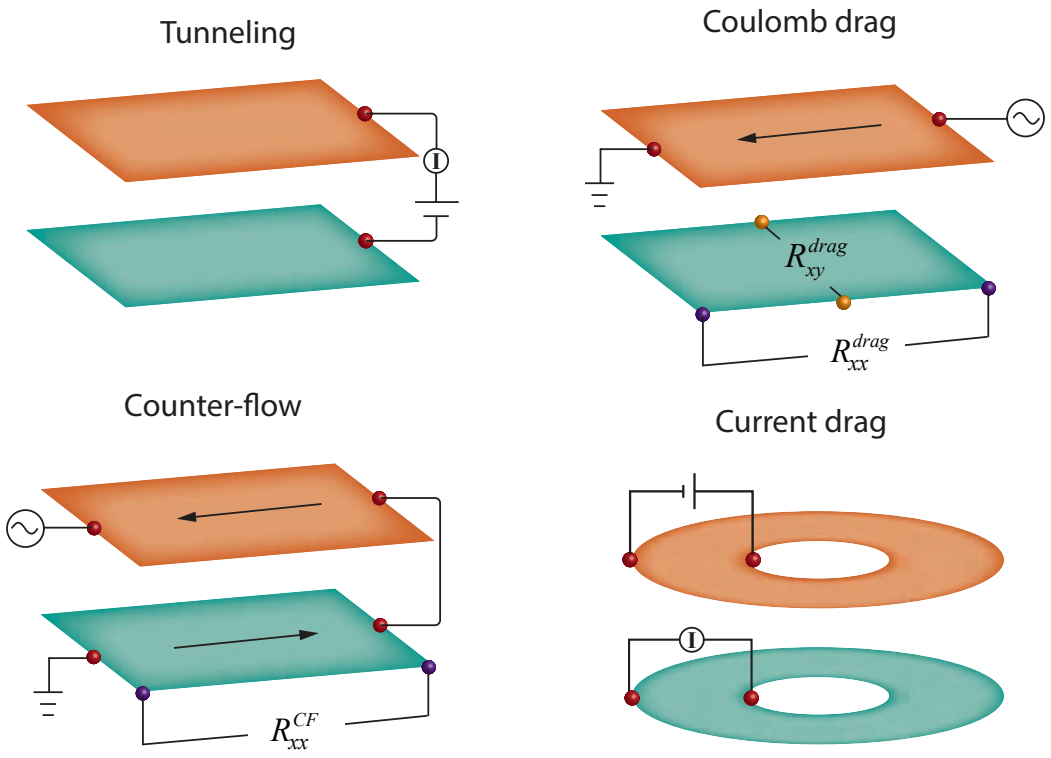

Figure 1.5: Various experimental schemes for probing the exciton condensate phase at $\nu_{tot} = 1$ in electronic double-layer systems.

emerges. As a matter of factor, this so called Hall drag resistance is quantized to h/e^2 and equals to the Hall resistance of the drive layer[47]. Details about this measurement will be discussed in Chapter 3. This quantization of drive and drag layer Hall resistance is partially due to the existence of a edge state. If the edge state is eliminated, conduction through excitons in the bulk is the only conducting channel in the system. As the excitons carry counterflow current, which is current in the two layers in the opposite directions, driving current in one layer induces an identical drag current in the opposite direction. This is called the perfect current drag and it confirms that excitons are indeed responsible for transport in the system[48].

Last but not least, the counter-flow measurement probes the resistance of exciton current[49,50]. By driving current in two layer in the opposite directions and measuring voltage drops in one of the layer, it senses dissipation of exciton flow. When a condensate is established, the counterflow resistance will be zero, which proves excitons form a superfluid.

1.4 Graphene double-layer devices

The devices studied in this thesis are graphene double-layers, where two monolayer or bilayer graphene are separated by a thin hexagonal boron nitride (hBN). In the earlier devices such as the one used in Chapter two and three, the graphene-thin-hBN-graphene structure is encapsulated by two thicker hBN layers to isolate the graphene layers from impurities on the outside. Electrical contacts are fabricated onto each individual layers. Metal gates and silicon backgate are used to tune the carrier densities in the top and bottom graphene. Later we adopted graphite gate scheme, where the double-layer

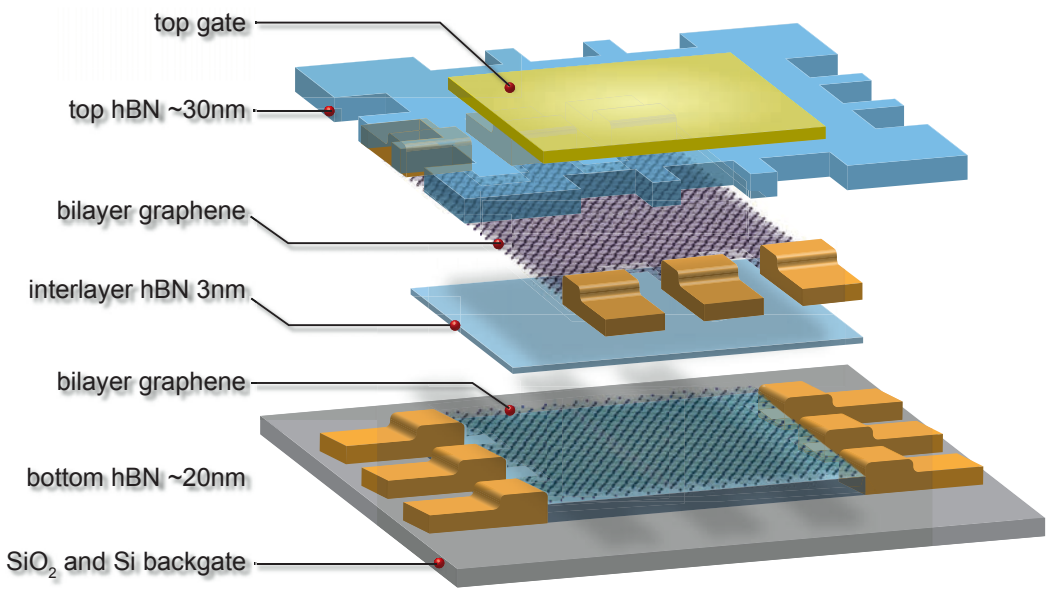

Figure 1.6: Schematic for graphene double-layer devices with metal and silicon gates. Blue represent hBN, while yellow denote metal contacts on individual layers.

structure is encapsulated by hBN-graphite. The graphites, being single crystal and atomic flat with little impurities, act as a Faraday cage for the graphene double-layers. This further reduces charge inhomogeneity and increases mobility of the samples.

1.4.1 Devices with metal and Silicon gate

First, I summarize the fabrication process for graphene double-layer devices with metal and silicon gates. The single-crystal layers of graphene and hBN are prepared by mechanical exfoliation. And the hBN-graphene-hBN-graphene-hBN stack (Fig. 1.7) is made with van der Waals (vdW) transfer technique[19]. For our purposes, we choose two graphene layers that are shaped as strips. We then

align the strips perpendicularly into a cross (can be seen in Fig. 1.7 panel 4) during the stacking process, so we can use the overlapped part as the main channel area while fabricating individual contacts on each layer at the non-overlapped parts (Fig. 1.7). The edge contacts (Cr/Pd/Au) on both graphene layers are deposited after etching the entire stack into the final device geometry. Top gate (Cr/Au) are fabricated on top of the main channel area after 20-30nm of ALD (atomic layer deposition) Al_2O_3 to insulate the top gate from the graphene.

Usually, the part of graphene near metal contacts are slightly doped and may form unwanted PN junctions due to the metal-graphene work function mismatch. These contact-induced local PN junctions cause bad contact to quantum Hall states under high magnetic fields. In order to address this problem, we fabricate local top gates (contact gates) to dope the graphene leads between metal contact and the main channel separately. These contact gates are adjusted to dope the graphene leads to very high densities of the same carrier type of the main channel.

1.4.2 Dual graphite gated devices

The dual graphite gated double-layer devices are made of hBN-graphite-hBN-graphene-thin-hBN-graphene-hBN-graphite (from the top to the bottom) (Fig. 1.8, the topmost hBN not shown). The topmost hBN is not necessary for device purpose, but it makes picking up graphite much easier and nicer. The challenge in making this kind of devices is that there are many conducting layers with shapes that we cannot control, i.e. two graphene, and two graphite gates. If we do not plan carefully, some of the layers might be shorted together by the metal contact after etching through the stack. To fabricate contacts onto each layer without shorting to other layers, initially I tried to partially

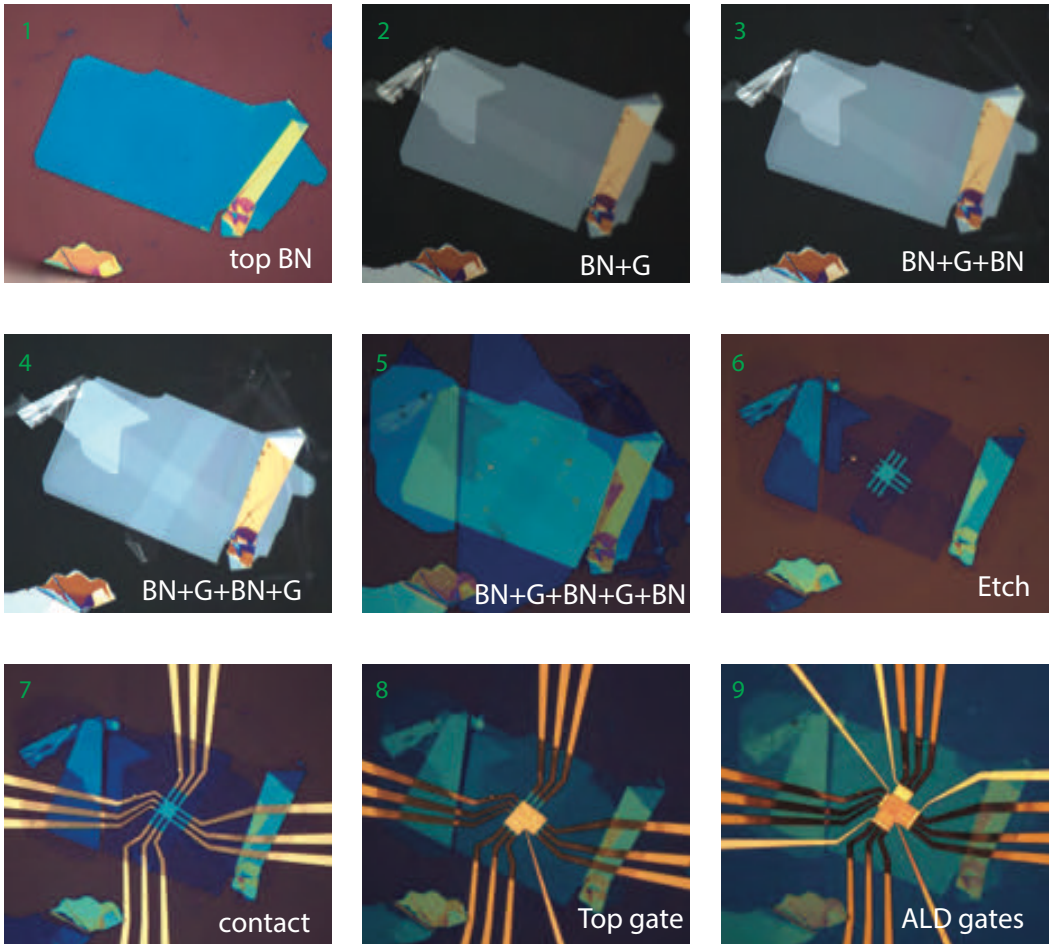

Figure 1.7: Fabrication process for graphene double-layer devices with metal and silicon gate. 1-5 are steps of stacking, while 6-9 are nano-fabrication processes.

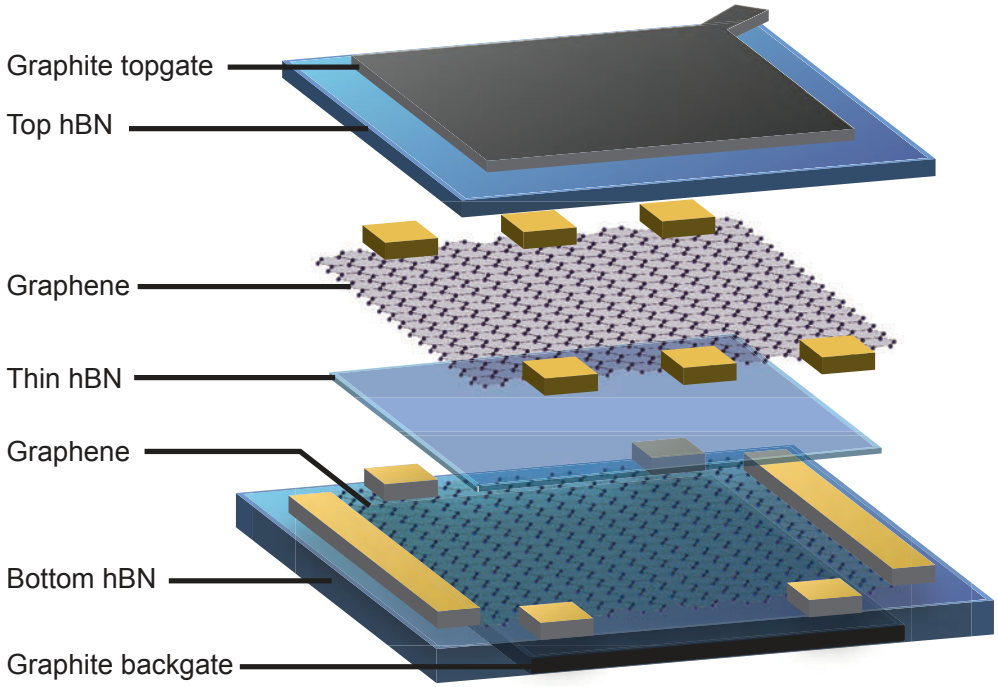

Figure 1.8: Illustration of graphene double-layer devices with dual graphite gates.

etch the stack. The idea was to etch the top graphite first into desired shapes and stop the etching before it reaches graphene. And then a different etch mask is prepared to etch the graphene layers but stops before it reaches the bottom graphite. The partial etch method works for the top graphite because etching graphite requires a different recipe (O_2 plasma) from etching hBN (CHF_3 plasma). The graphite etch can stop at the hBN layer without reaching the graphene layers. However this does not work for the etching of graphene layers, which is very thin and can be penetrated by CHF_3 plasma. So very often I found the graphene contacts are shorted to the graphite backgate, rendering the device useless.

Then I decided to avoided having two different conducting layers (except the top graphite, which can be controllable defined by partial etch) at the place where I would fabricate contacts. The easy way to do this is to pre-pattern the bottom graphite (Fig. 1.9 left). We etch the bottom graphite into a rectangle with a lead extending out before depositing the rest of the stack onto it. After the stack is deposited, the top graphite gate is etched into the same shape of bottom graphite with the exception of a different lead for contacting the gates separately. This way we can use the same cross design of graphene double-layer found in the metal and silicon gated devices without worrying about shorting graphene to graphite gates, as long as the overlapped cross is bigger than the pre-patterned rectangle (Fig. 1.9 left). This schemes is used for Chapter 4 and 5.

However, the pre-patterned graphite is dirtier than natural cleaved ones due to contamination during the fabrication. So for the best quality, we went back to use all natural cleaved flakes. To do this, the shape of graphene and graphite are carefully chosen and arranged so that we can use the overlapped part as the main channel area while fabricating individual contacts on each layer at the

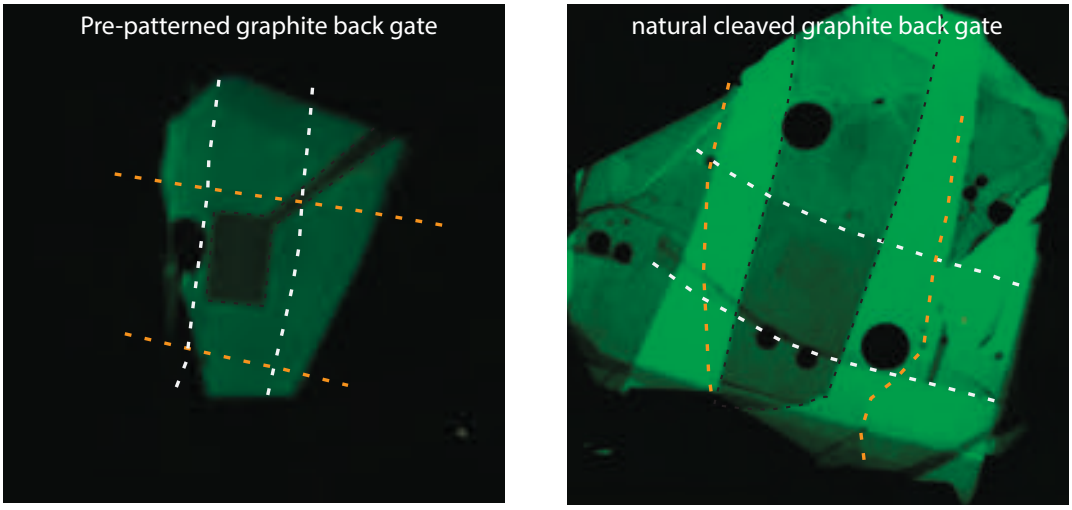

Figure 1.9: Fabrication of dual graphite gated devices. Left, the bottom graphite are pre-patterned before the rest of stack is placed on it. Black dashed line marks the shape of bottom graphite. Orange dahsed lines marks the boundary of top graphene layer. White dashed lines marks the boundary of bottom graphene. Right, bottom graphite (black dashed line) is not pre-patterned but naturally cleaved.

regions with just one conducting layer (Fig. 1.9 right). Square-shaped top graphene layer is chosen (Fig. 1.9 right, orange colored lines), while we choose strip-shaped bottom graphene (white colored lines) and bottom graphite (black color), that are narrower but longer than the top graphene. We align the bottom graphite and bottom graphen into a cross while keeping the overlapped area inside the top graphene square. The top graphite covers everything after stacking but is etched into the same shape as bottom graphite in the first fabrication step. We then etch the stack into final device geometry and fabricate Cr/Pd/Au contacts on top graphite, two graphene layers and bottom graphite all at once. Last, we grow 20-30nm ALD Al_2O_3 before depositing contact gate above top layer graphene lead to increase the contact transparency.

2

Frictional Coulomb drag in strong magnetic fields

As mentioned in the introduction, frictional Coulomb drag effect between Fermi liquids is relatively well established. However, frictional drag effect under a magnetic field is not yet understood. In the presence of magnetic fields, drag voltages can be decomposed into magneto-drag (longitudinal com-

ponent) and Hall-drag (transverse component). At a first glance, the Hall drag should be zero, as carrier moving in the drive layer only kicks carriers of the drag layer in the same direction as drive current. However, as the momentum direction of carriers under magnetic field is not aligned with the direction of charge current, non-zero Hall drag can occur, but yet to be observed. Moreover, under strong magnetic fields, quantized Landau levels (LLs) form in both layers, requiring consideration beyond the semiclassical Fermi liquid description. Early experimental works in GaAs double quantum wells revealed surprising sign changes of magneto-drag, which depends on the LL filling factor difference between the two layers[51,52]. Due to the lack of gate tunablity and small drag response, these studies are often inconsistent and fail to promote a testable explanation.

Graphene double-layer devices provide an excellent material platform to investigate the magneto-drag and Hall-drag effect, owing to a wide range of gate tunability of individual layers, large LL separation, and small inter-layer distance. In this chapter, we present experimental investigation of frictional magneto- and Hall-drag in high mobility graphene double-layer devices. The observed large magneto-drag and Hall-drag signals can be related with Laudau level (LL) filling status of the drive and drag layers. We find that the sign and magnitude of the drag resistivity tensor can be quantitatively correlated to the modulation of resistivity tensors in the drive and drag layers, confirming a theoretical formula for proposed by von Oppen, Simon and Stern (OSS)[53]. Magnetic field and temperature dependence of the drag effect further reveals the nature of the Coulomb scattering between quantized Landau levels.

The devices used in this experiment is monolayer graphene double-layer separated by a thin hBN $\sim$4 nm, encapsulated by two thicker BN layers ($\sim$20 nm). Interlayer tunneling resistance is found

to be larger than GΩ range. The low temperature (1.5 K) mobility of the bottom layer is ∼50 m^2/Vs and the top layer shows a slightly lower mobility of ∼20 m^2/Vs. With this mobility range, quantum Hall effect (QHE) can be observed at magnetic field B as low as 0.2 T in both layers. Voltages applied to the back gate (V_{BG}) and the top gate (V_{TG}) control the carrier density of the top layer n_T and the bottom layer n_B.

2.1 Coulomb drag under B=0

We begin our exploration with Coulomb drag measurements at zero magnetic field. The drag measurements are performed by applying a small drive current $I_{drive} \sim 100nA$ to the (active) drive layer and measuring the drag voltages in the (passive) drag layer. The low frequency Lock-in measurements (17.7Hz) we use essentially probe the DC drag response.

Our drag measurements at 300K is similar to what has been reported by the Manchester group[32]. The position of charge neutral point of each layer not only depend on the corresponding gate (e.g. top gate for top graphene layer) but also depend on the opposite gate voltage (e.g. bottom gate) due to incomplete screening. Due to the small density of state in graphene, some electrical fields from the bottom gate can penetrate through bottom graphene layer to dope the top graphene layer. As a result, the dashed lines in Fig. 2.1 marking neutral point of each layer are not straight lines. This effect can be simulated by a model considering all the geometric and quantum capacitance of the system. The charge neutral lines of the two layers divide Fig. 2.1 into four quadrant. Drag resistance is negative when the carrier types of both layers are the same (top right and bottom left in

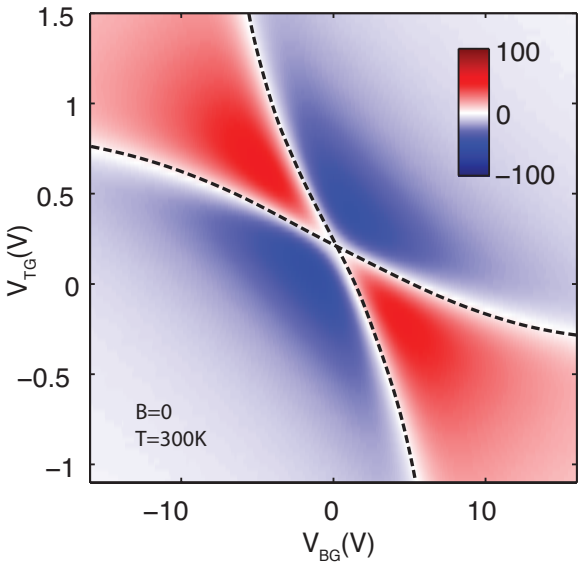

Figure 2.1: Coulomb drag (Ohm) at room temperature and under zero magnetic field as a function of top and bottom gate voltages. The dashed lines marks Dirac point of the top and bottom layer.

Fig. 2.1), and is positive when the carrier types of the two layers are different (top left and bottom right). Along the charge neutral line, Coulomb drag effect is near zero. This is due to Coulomb drag effect requires particle-hole asymmetry respect to the Fermi energy [26]. At charge neutral Dirac point, monolayer graphene is electron-hole symmetric, thus have no drag response.

Drag behavior for most parts of this measurement is well understood. However, the case for double neutrality point (DNP), where both layers are charge neutral, is more intriguing (where two dashed lines in Fig. 2.1 intercept). Previous study have shown a positive drag resistance at DNP, which increases and then decreases as temperature drops from room temperature. In contrast, our measurements (Fig. 2.2) show a negative drag resistance at DNP, the magnitude of which also goes up and down as temperature decrease. This difference in the sign of drag signal suggests the drag

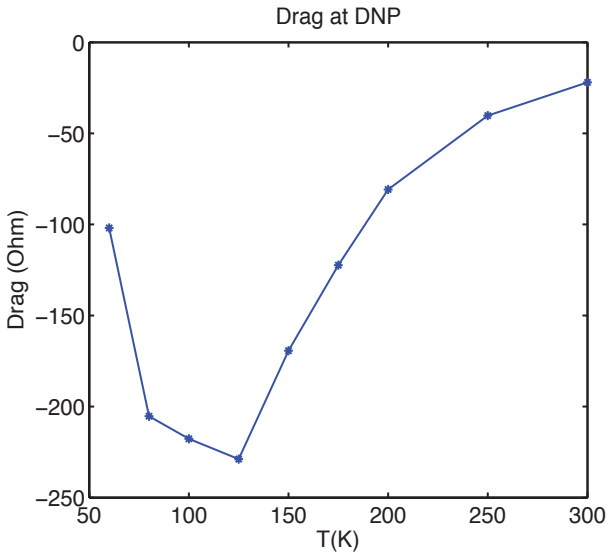

Figure 2.2: Coulomb drag at double neutrality point as a function of temperature at zero magnetic field.

effect at DNP is not universal but may depend on the details of the sample, such as impurity level or sample size.

2.2 Eliminating spurious drag signals

When we try to carry out drag measurements at low temperatures and under magnetic fields, we found some unexpected problems. The measured drag signal in the quantum limit does not depend on the top and bottom gates in the same way (Fig. 2.3). In an other word, Fig. 2.3 does not look symmetric respect to changing x and y axis. In Fig. 2.3, the top layer is the drive layer and bottom layer is the drag layer. The sign of drag signal changes even when the carrier types of both layer stay the same. However, this sign change is only sensitive to drag layer density changes. Changing the drive layer density merely modulate the amplitude of drag resistance, but does not affect the sign.

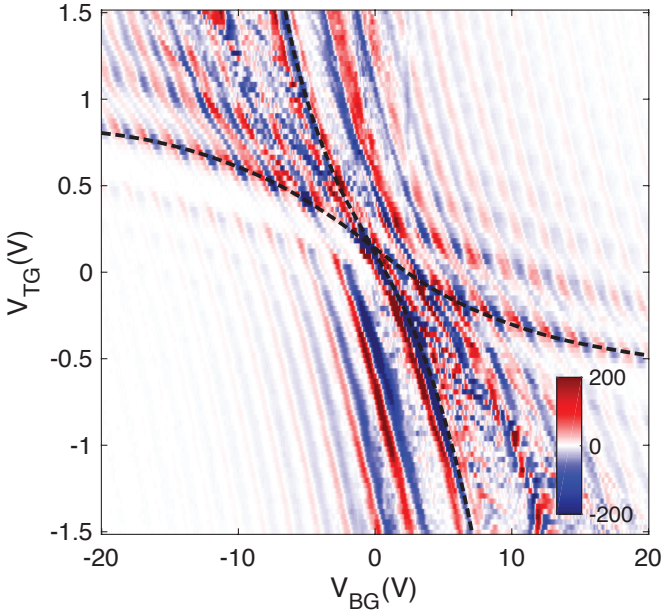

Figure 2.3: Magneto-drag (Ohm) at B=1T and T=1.5K, with the top layer as drive layer and bottom layer as drag layer.

Assuming the two layers are similar, this observation suggests Onsager relation is broken. Onsager reciprocal relation states: if we switch the current and voltage terminals as well as flip the magnetic field direction, the measured multi-terminal resistance should stay the same in a linear response system ($R_{12,34}[B] = R_{34,12}[-B]$). Fig. 2.4 explicitly demonstrate a different drag response when we switch the drive and drag layer. Onsager relation is built on the time reversal symmetry and broken of Onsager suggests something is wrong with our measurements.

When we were trying to resolve this mystery, we come across a paper [54] about spurious drag signals originated from the "interlayer bias" effect. To test this possibility, we need to separately control the source and drain bias on the drive layer, instead of grounding the drain and applying bias to the source. Using the circuit shown in Fig. 2.5, positive bias voltage V_{drive+} is applied on the

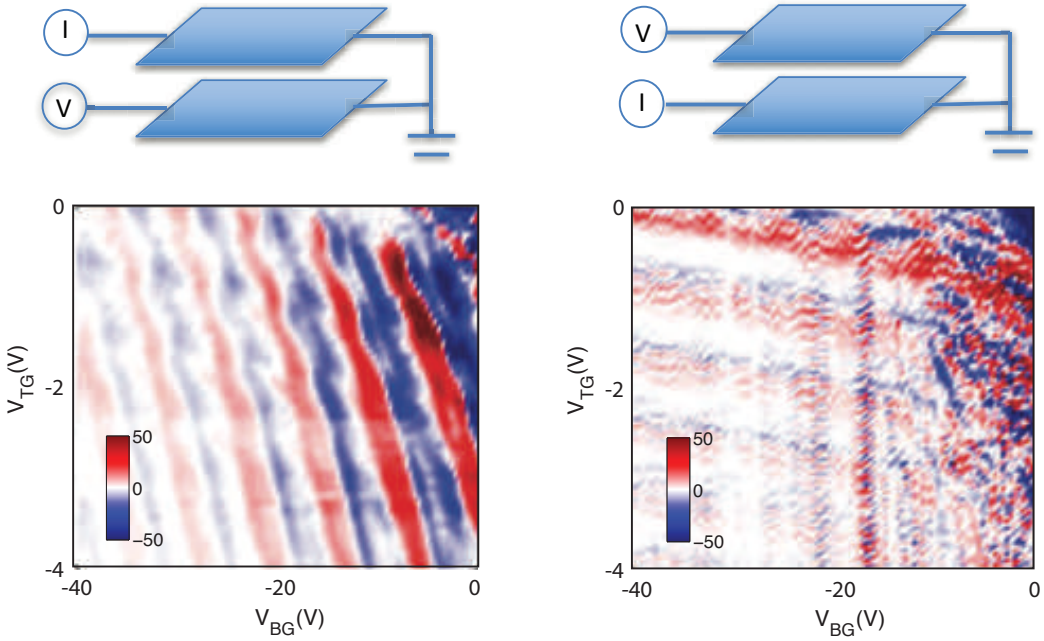

Figure 2.4: Switching the drive and drag layer, and at the same time flipping the magnetic field direction (from 8T to -8T) produces different drag resistance (Ohm). This shows Onsager reciprocal relation is broken.

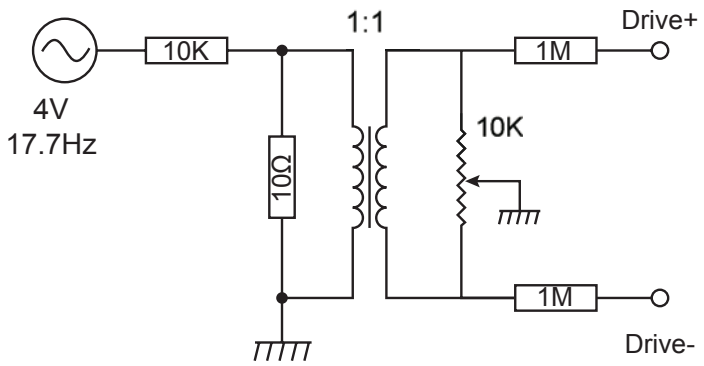

Figure 2.5: Circuit for adjusting the interlayer bias, while keeping bias current the same. The left part is a 1000:1 voltage divider, reducing 4V bias down to 4mV. The middle is a 1:1 transformer to isolate the ground. On the right, we have a variable resistor (potentiometer) to change the common mode. The two 1MOhm resistor is to convert 4mV voltage bias to 2nA current bias.

source of the drive layer, while V_{drive-} is applied on the drain of the same layer[27]. We can independently adjust the common mode ($V_{drive+} + V_{drive-}$) by changing the variable resistor, while keeping the differential bias ($V_{drive+} - V_{drive-}$) the same. If the drag response is real, changing the variable resistor should not affect the result as the current flowing in the drive layer stays the same ($(V_{drive+} - V_{drive-})/R_{drive}$). Surprisingly, we found drag resistance depend critically on the variable resistor setting (Fig. 2.6). By measuring the voltage difference between a non-current-carrying contact on the drive layer and a contact on the drag layer (interlayer bias voltage), we found the sign of drag signal is correlated with the sign of interlayer bias voltage.

We later understand, with the simple bias scheme we were originally using, the drive layer is at a different potential from the drag layer (Fig. 2.7). This is due to the voltage drops across the large contact resistances (can often be $100k\Omega$ in high fields) between graphene and metal. Flowing current across this large contact resistance rise the potential on the drive layer to about half of the bias volt-

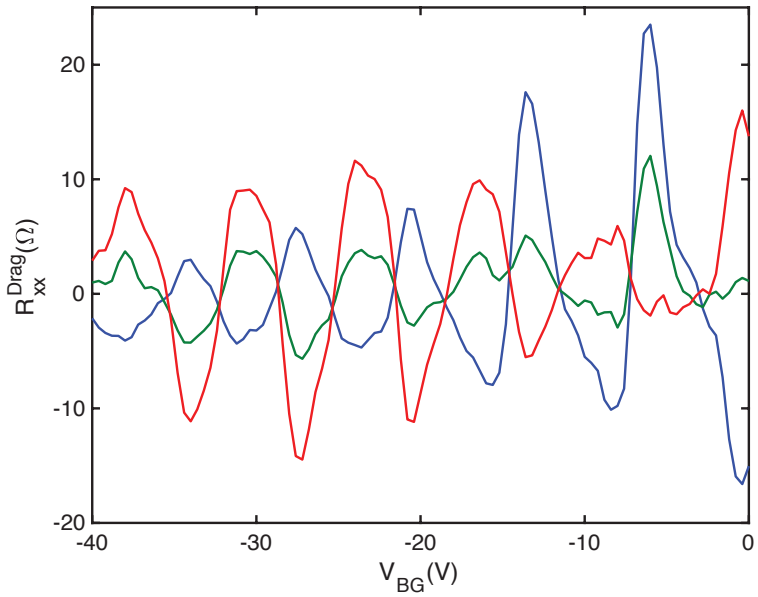

Figure 2.6: Effect of adjusting the interlayer bias on drag resistance. This plot takes a linecut across the oscillating drag signal shown in Fig. 2.4 left. Curves with different color are taken with different variable resistor settings. The sign of drag is flipped when the sign of interlayer bias changes. This demonstrates the measured drag response is spurious signal coming from the interlayer bias, instead of real drag response associated with drive current.

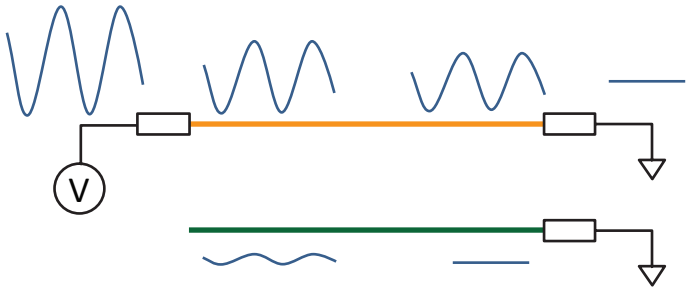

Figure 2.7: The origin of interlayer bias. The sine waves represent the AC voltage at different part of the sample.

age (assuming source and drain have similar contact resistance). This potential have a gating effect on the drag layer, which modulates the drag layer carrier density. Interestingly, if we measure a conductor inside a fridge, it is very common to see a constant DC voltage due to thermoelectric effect. As the interlayer bias modulate the carrier density of the drag layer, it also modulates this DC voltage. This modulation of DC voltage appears as a AC voltage in sync with the drive current, which we interpreted as the drag voltage. We found this spurious signal is most pronounced at low temperatures and high magnetic fields, where the contact resistances are high and thermoelectric effects are strong.

2.3 Magneto-drag and Hall-drag in the quantum Hall regime

To eliminate this spurious signals originating from interlayer bias gating effect, interlayer balancing is implemented in the drive layer. We tune the variable resistor so that the interlayer bias is minimized. Also we stayed in relatively high temperature range, where the real drag effects are strong and spurious effects are weak. Onsager reciprocity and linear response of the drag signal to

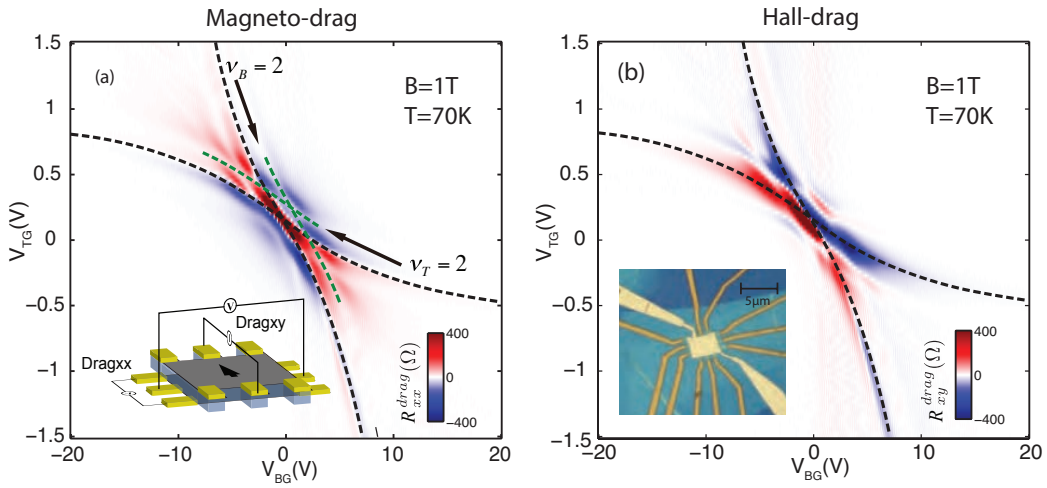

Figure 2.8: (a) Magneto-drag resistance measured under a magnetic field of 1T and at a temperature of 70K. Black and green dashed lines mark charge-neutrality and $\nu = 2$ of the individual layers, respectively. Insert shows the schematic of the measurement. (b) Hall-drag resistance under the same condition as (a). Inset is an optical microscope image of the device used in this experiment.

I_{drive} are confirmed, indicating we are measuring the real drag response. The magneto-drag resistance R_{xx}^{drag} and Hall-drag resistance R_{xy}^{drag} are obtained from the measured voltages across the passive (drag) layer. The drag data presented here is taken under both positive and negative magnetic fields and symmetrized (anti-symmetrized) for $R_{xx}^{drag} = (R_{xx}^{drag}[B] + R_{xx}^{drag}[-B])/2$ and $R_{xy}^{drag} = (R_{xy}^{drag}[B] - R_{xy}^{drag}[-B])/2$ to remove mixing between longitudinal and Hall components.

Fig. 2.8 shows R_{xx}^{drag} and R_{xy}^{drag} as a function of V_{BG} and V_{TG}, measured at T =70 K and relatively low magnetic field B =1 T. The two black dashed lines crossing each other correspond to $\nu_T = 0$ or $\nu_B = 0$, the charge neutrality point (CNP) of each layer. Similar to the zero field case, these CNP lines divide the (V_{TG}-V_{BG}) plane into four regions, e-e (top-right), h-h (bottom-left),

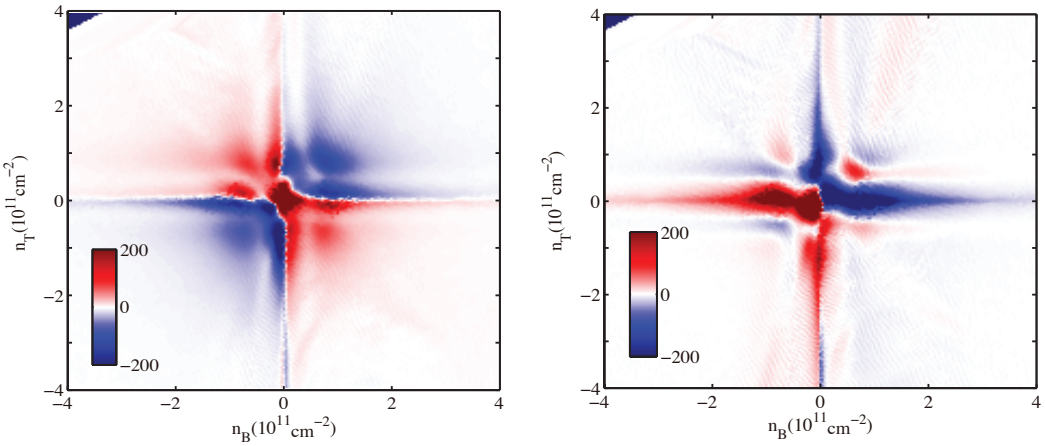

Figure 2.9: Same data as Fig. 2.8, but with gate voltages converted to densities of each graphene layer. Note that the sign of magneto-drag (left) only depend on carrier types. But the Hall drag (right) shows sign changes even in the same carrier types quadrant.

e-h (bottom-right) and h-e (top-left). For magneto drag (Fig. 2.9 a), the sign of R_{xx}^{Drag} follows the sign of drag at $B = 0$, i.e. the e-e and h-h regions show a negative drag signal, while the e-h and h-e regions exhibit a positive drag. Along the CNP lines, $R_{xx}^{Drag} \approx 0$. We also note that there is additional modulation in each regions, where some $R_{xx}^{Drag} \approx 0$ lines running in parallel with CNP lines (examples are marked by green dashed lines in Fig. 2.8). Further inspection in connection with the magneto-resistance measurements of each layer (which will be discussed later in detail) indicates that these lines are corresponding to integer LL filling fraction ν_T or ν_B, where either the active or passive layers are in a quantum Hall (QH) state. The vanishing R_{xx}^{Drag} signal in these QH regions thus suggest the drag become inefficient as the bulk of either layer becomes incompressible. The incompressible bulk results in zero density of state for interlayer Coulomb scattering.

This observation is more pronounced at higher magnetic fields where stronger QHE appears

with a wide range of incompressible regions in the (V_{TG}-V_{BG}) plane. Fig. 2.10 (a) shows $\rho_{xx}^{Drag}(V_{TG}, V_{BG})$ measured at B=13T, where the well-developed zig-zag shaped incompressible stripes of QH states can be identified with zero drag (for example the green dashed lines surround $\nu_{bot} = 2$ incompressible strip, where drag vanishes). The zig-zag shape of the CNP (black dashed lines) and other incompressible stripes originate from variance of screening effect inside and outside of LLs. Inside the LL of the top layer, the high density of state nearly perfect screen top gate electrical field, thus the resistance contour of the bottom layer is straight. Vice versa for the bottom gate. In between LLs of the top layer, there is zero screening effect due to zero density of state in the top layer, thus the contours are diagonal, as both top and bottom gates dope the bottom graphene equally, as if the top layer does not exist.

The corresponding Hall-drag R_{xy}^{drag} measurements shows similar vanishing signals in the incompressible regions in the (V_{TG}-V_{BG}) plane as shown in Fig. 2.10 (b). We note R_{xy}^{drag} exhibits similar magnitude as R_{xx}^{drag}, confirming the prediction made by OSS. However, unlike R_{xx}^{drag} whose sign is determined by the sign of carriers, R_{xy}^{drag} undergoes sign changes within each quadrant. Also contrary to R_{xx}^{drag}, R_{xy}^{drag} does not vanish along the CNP lines. At higher magnetic field $B = 13$ T (Fig. 2.10 (b)), the incompressible QHE regions exhibit well-developed regions of vanishing ρ_{xy}^{drag} similar to ρ_{xx}^{drag}.

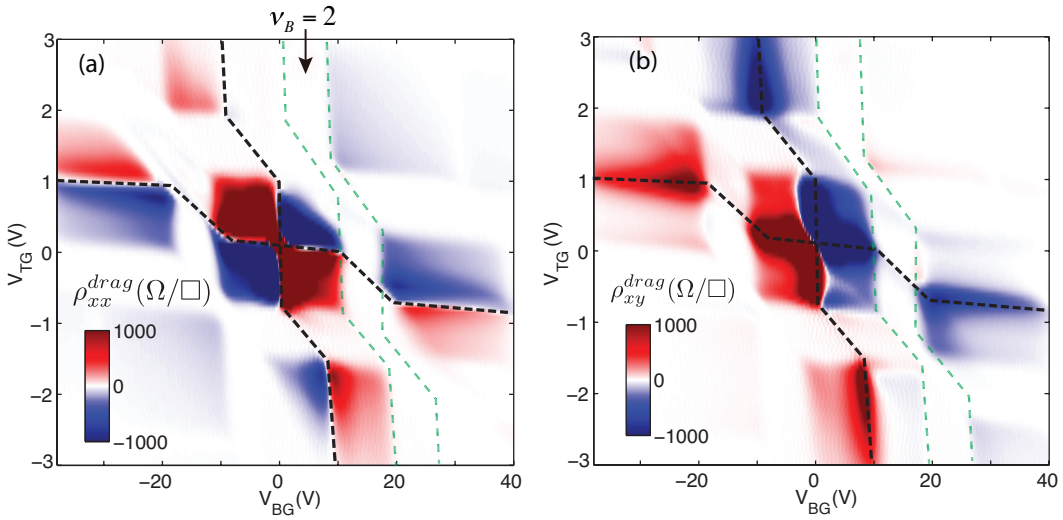

Figure 2.10: Measured magneto- and Hall-drag resistivity at T=70K, B=13T. Black dashed line still mark the charge neutral points of each layer, while the green lines indicate boundary of $\nu = 2$ quantum Hall plateau.

2.4 Simulation from OSS formula

We later found a theory work matches our experimental data. Extending prior theoretical work based on the linear response theory[55,56,57,58], von Oppen, Simon and Stern (OSS) proposed a theoretical approach to frictional drag effect under strong magnetic fields[53]. According to OSS, the drag resistivity tensor $\hat{\rho}^{drag}$ can be related to the density differential of the magneto-conductivity tensors $\hat{\sigma}$ in individual layers:

$$\hat{\rho}^{drag} \sim -\hat{\rho}^{p} \frac{d\hat{\sigma^{p}}}{dn^{p}} \frac{d\hat{\sigma^{a}}}{dn^{a}} \hat{\rho}^{a} \tag{2.1}$$

Here, $\hat{\rho} \equiv \begin{pmatrix} \rho_{xx} & \rho_{xy} \\ \rho_{yx} & \rho_{yy} \end{pmatrix}$ and $\hat{\sigma} = \hat{\rho}^{-1}$ are the magneto resistivity and conductivity tensors, respectively. n is carrier density of each layer, and the superscripts a and p stand for active (drive) and

passive (drag) layers, respectively. The physical interpretation of this theory is that driving DC current on one layer creates asymmetry in the thermal density fluctuations in that layer. These density fluctuations are transferred to the drag layer through Coulomb interaction. Then the induced density fluctuations in the drag layer are rectified to a DC voltage. It predicts that Hall-drag could have the same magnitude as the magneto-drag. This formula links the drag response to the resistivity of each layer, and provide a testable formula that we could examine experimentally.

To compare density-dependent magneto- and Hall-drag with Eq. 2.1, we need obtain magneto-resistance tensor $\hat{\rho}$ and $\hat{\sigma}$ as a function of densities. Experimentally, we measured the longitudinal (R_{xx}) and transverse (R_{xy}) components of magneto-resistance on each layer and then converted them to $\hat{\rho}$ and $\hat{\sigma}$ using simulated geometrical factors. Fig. 2.11 are measured ρ_{xx} and ρ_{xy}, the two independent components of $\hat{\rho}$, of the top and bottom layers as a function of the top and gate voltages V_{TG} and V_{BG}. These data were taken at the same condition as the drag experiment shown in Fig. 2.10 and symmetrized (anti-symmetrized) to remove mixing between R_{xx} and R_{xy}. Under strong magnetic fields, the relation between the density and V_T and V_B can be complicated due to the varying screening effect in LLs. In general, the derivation of conductivity respect to density $\frac{d\hat{\sigma}}{dn}$ thus include derivation to both top and bottom gate:

$$\frac{d\hat{\sigma}}{dn} = \frac{d\hat{\sigma}}{dV_{BG}}\frac{dV_{BG}}{dn_B} + \frac{d\hat{\sigma}}{dV_{TG}}\frac{dV_{TG}}{dn_T}. \tag{2.2}$$

However $\frac{d\hat{\sigma}}{dn}$ is not zero only in the compressible regions of (V_T, V_B), as the imcompressible region have quantum Hall plateaus. When both layers are compressible, the gating effect decouple

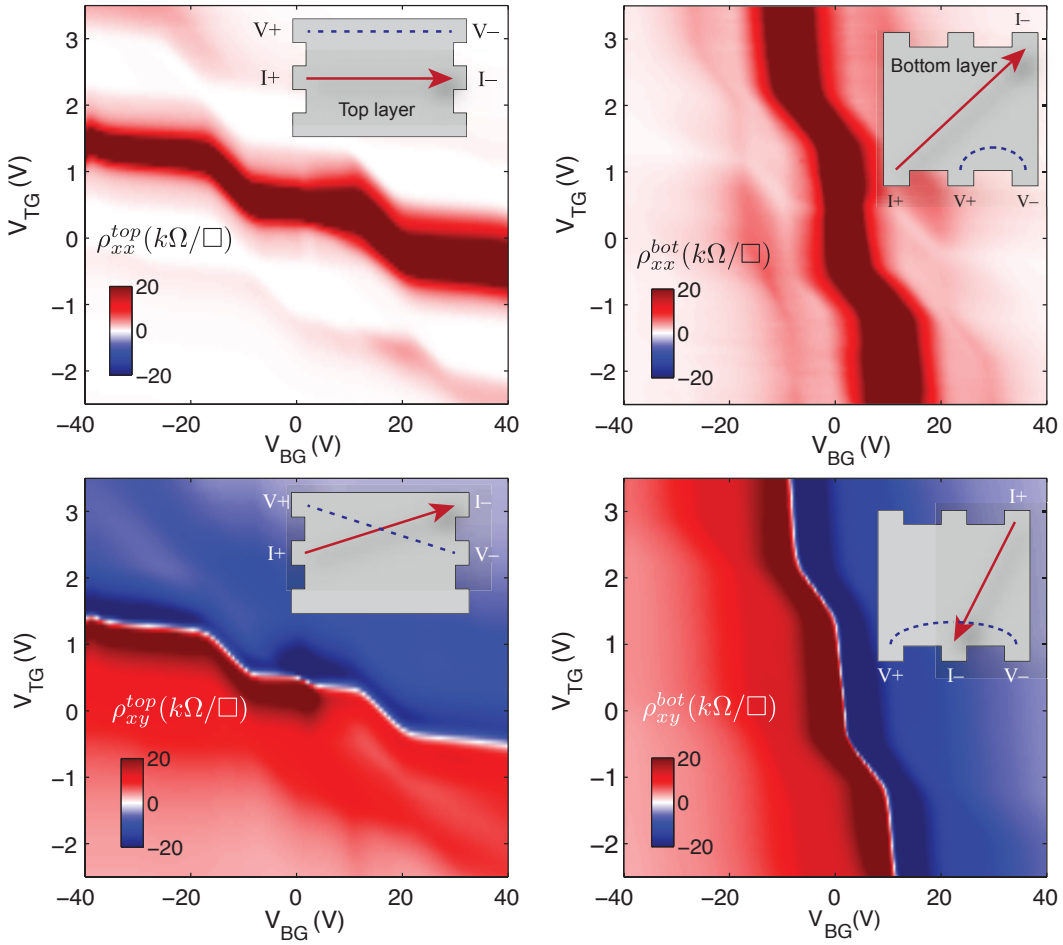

Figure 2.11: Magneto- and Hall-resistivity of each layer. The inset of each panel illustrates the measurement setup for each corresponding quantity. This measurement is taken under the same condition as the drag measurements at B=13T and T=70K.

to each corresponding layer due to nearly perfect screening, resulting $n_T = C_{TG}V_{TG}/e$ and $n_B = C_{BG}V_{BG}/e$. Therefore, taking derivative respect to densities is the same as respect to gate voltages times geometric capacitances.

Fig. 2.12(c-d) shows the computed drag resistivity ρ_{xx}^{drag} and ρ_{xy}^{drag} obtained from $\hat{\rho}^{drag}$ by applying experimental obtained $\hat{\rho}^{a,p}$ to Eq. 2.1. $\hat{\sigma}^{a,p}$ were obtained by numerically inverting $\hat{\rho}^{a,p}$ tensor. Comparing these calculated results with the measured drag resistivity shown in Fig. 2.12(a-b), we find the theory provides reasonable match to the experiment by capturing key features of the sign and magnitude of the observed drag. To be specific, for ρ_{xx}^{drag}, the calculation successfully captured that the sign of drag is governed by carrier types and does not change cross LLs for graphene double-layer specifically. For ρ_{xy}^{drag}, the complicated changes of Hall drag signs are also revealed by the calculation. We note that while the calculated drag exhibits excellent agreement with the data in the compressible regime, the agreement between experiment and calculation is worse in the incompressible strips, especially for ρ_{xy}^{drag}. Specifically, the measured drag signals vanish as expected while the calculated one does not. This is due to the imperfect measurement geometry (Fig. 2.11 insets) for ρ_{xx}^{top} and ρ_{xy}^{bot}, which lead to non-perfect QHE (as can be seen in Fig. 2.11). These geometries are unideal as they are very far from a Hallbar measurement. We were constrained by some of the contact being unavailable. The non-perfect quantization results in finite $\frac{d\hat{\sigma}}{dn}$ which lead to non-zero calculated drag.

While comparing the absolute magnitude of experimental drags to theoretical expectation is not possible due to the undetermined prefactor in Eq. 2.1, we can still make a relative comparison of the magnitude of different components of the drag resistivity tensor. Fig. 2.13 shows an example of such

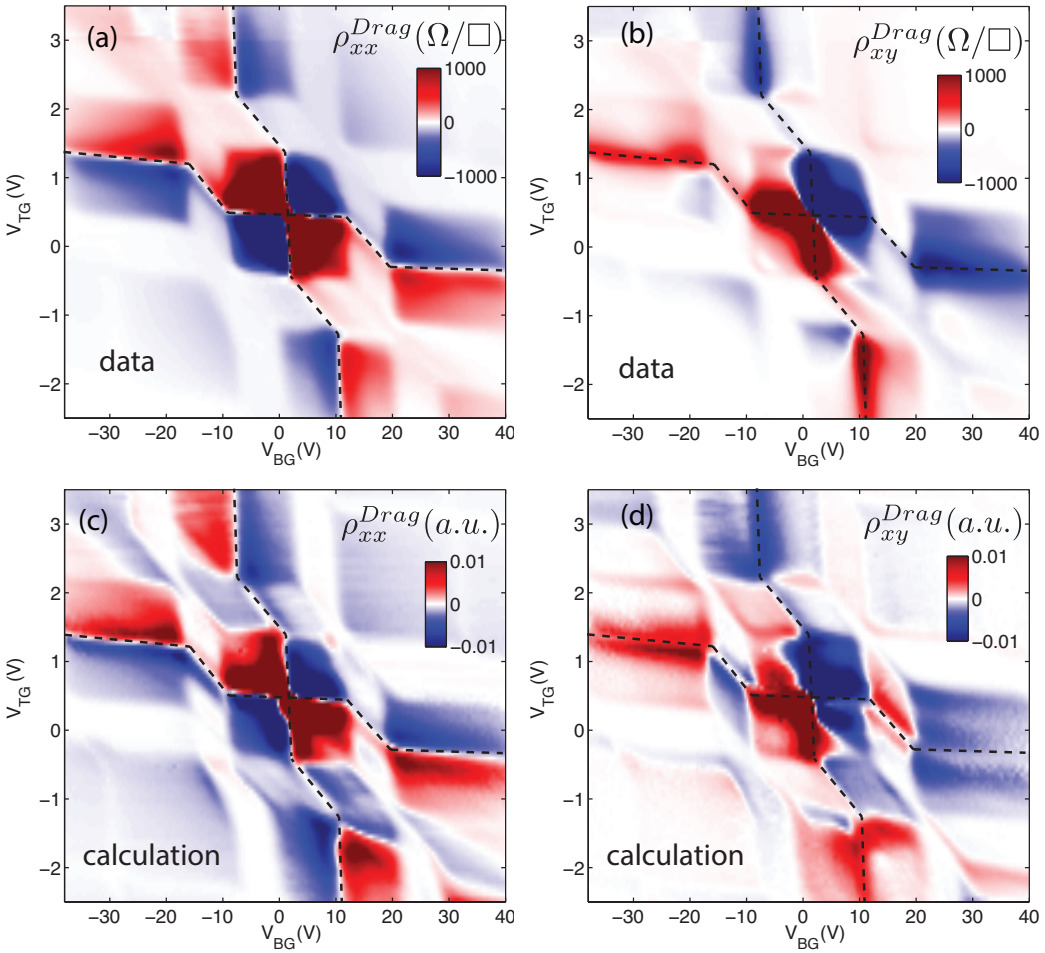

Figure 2.12: a) and (b), measured magneto- and Hall-drag resistivity at T=70K, B=13T. (c) and (d), calculated magneto- and Hall-drag resistivity using Eq. 2.1. The calculation is in arbitrary unit (a.u) due to the undetermined prefactor.

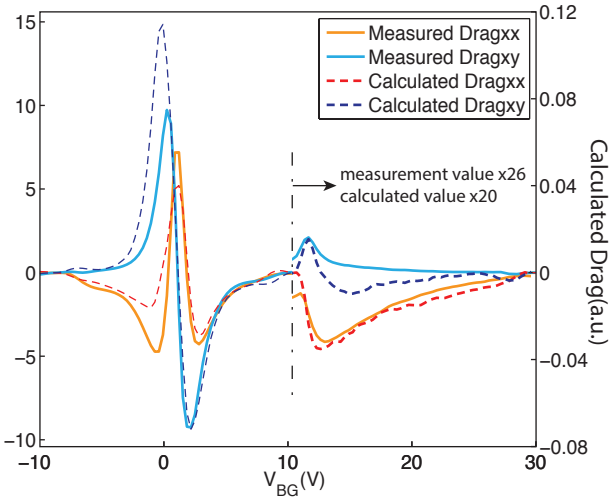

Figure 2.13: line-cut of measured and calculated magneto- and hall-drag along the equal-density line ($n_T = n_B$). The dashed vertical line around $V_{BG} \approx$10 V separates the first LL (N=1) region (right) from the zeroth LL (N=0) region (left). In the first LL region, measured drag is multiplied by a factor 26 for clarity while the calculation is multiplied by a factor 20 in order to make a good comparison to the measured values.

a comparison along the equal-density line ($n_T = n_B$). Note that the prefactor in Eq. 2.1 could be a function of density, temperature and field. We multiplied a common factor to Eq. 2.1 to make the calculated results comparable to experimental $\hat{\rho}^{drag}$. Plotting the magneto-drag and Hall drag in the same scale, we found that the relative magnitude between measured ρ_{xx}^{drag} and ρ_{xy}^{drag} (solid curves) match well with the calculation (dashed curves), proving that Eq. 2.1 holds quantitatively. For best matching, we also note that we multiplied different common factors for different LLs whose ratio is $\sim$1.3 for N=0 to N=1 Landau level (separated around $V_{BG} \approx$10V, indicating that the prefactor in Eq. 2.1 can be LL dependent but has a weak density dependence within a LL.

2.5 Temperature and field dependence

Finally, we discuss the temperature and magnetic field dependence of drag signals. Unlike the zero magnetic field drag, which was found to be proportional to T^2 owing to the increasing scattering phase space in the Fermi liquid[32], ρ_{xx}^{drag} measured in the high magnetic field regime exhibits a relatively weak temperature dependence. Fig. 2.14(a) and (b) show the temperature and density dependent ρ_{xx}^{drag}. We note that even for $N = 0$ LLs (orange shaded region in Fig. 2.14(a)), where we observed the most significant temperature dependence, the drag signals increase only by a factor of $\sim$2 as temperature changes from 40 K to 240 K. In particular, when both layers are on $N = \pm 1$ Landau level (red dashed line in Fig. 2.14(b)), there is almost no temperature dependence above $\sim$40K. The observed temperature insensitive drag effect is presumably due to the fact that the thermal energy is much larger than the individual LL spreads, but much smaller than the LL spacing (the first cyclotron gap $\sim$1500K at B=13T). Under these conditions, only one LL is partially occupied while the LLs above or below are completed empty or full. And as temperature is much larger than LL broadening, the entire partially filled LL is always accessible for Coulomb scattering. In this temperature regime (40K to 240K), temperature no longer controls the scattering phase space, so drag no longer depends on temperature. At even lower temperatures (T$\sim$15K), a set of broken symmetry QHE emerges, and the agreement with the OSS theory persists. Interestingly, ρ_{xx}^{drag} exhibits a strong magnetic field dependence. Fig.2.14(c) shows ρ_{xx}^{drag} as a function of magnetic field at T=240K, where a B^2 dependence is observed across different densities. One possible explanation of the strong field dependence is that the scattering phase space is enlarged by the increase of

the LL degeneracy at higher fields. The scattering phase space in the quantum Hall regime is mostly controlled by the LL degeneracy instead of temperature, thus shift the square law from T^2 to B^2.

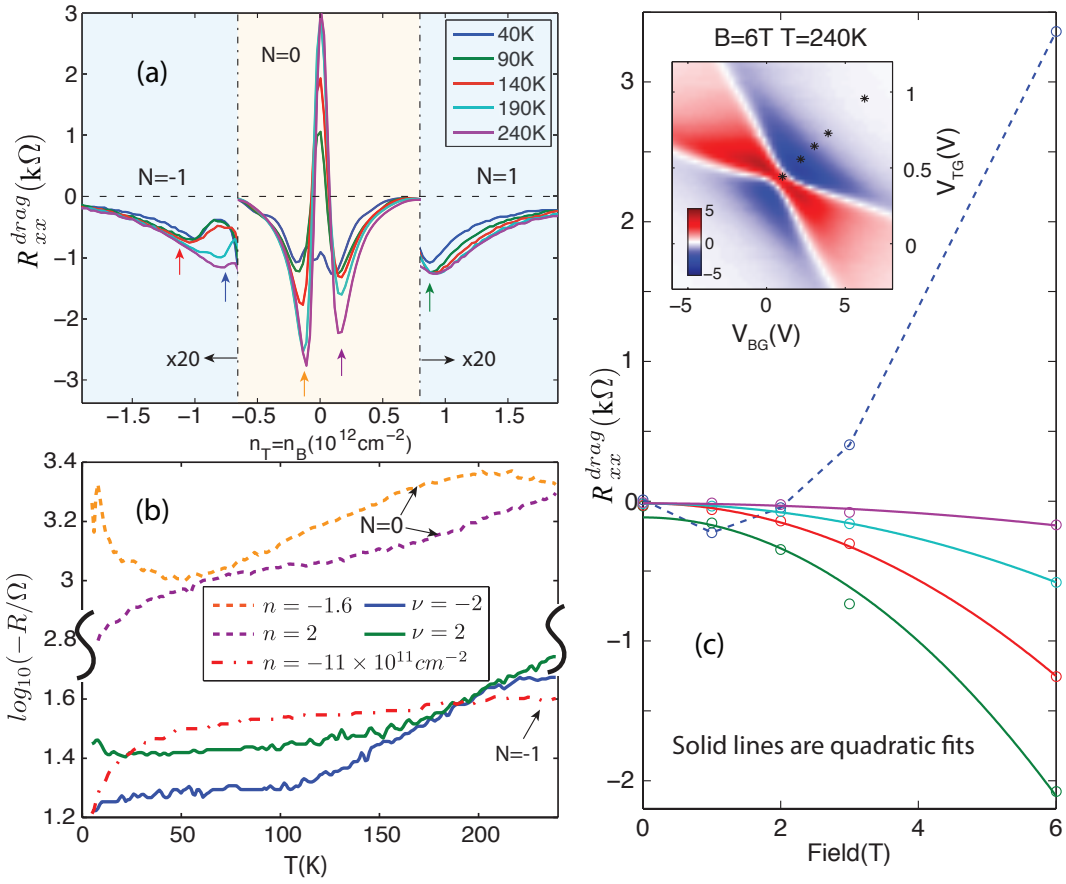

Figure 2.14: (a)Magneto-drag along equal density line ($n_B = n_T$) as a function of densities at B=13 T and different temperatures. The blue (yellow) shaded region marks $N = \pm 1$ ($N = 0$) LL. The drag signals are multiplied by a factor of 20 in the blue shaded regions for clarity. (b) drag as a function of temperature at different density points. Solid lines represent the Landau gaps $\nu = \pm 2$. Dashed line represent partially filled LLs: $n = -1.6, 2 \times 10^{11}\mathrm{cm}^{-2}$ corresponding to $N = 0$ LL; $n = -11 \times 10^{11}\mathrm{cm}^{-2}$ correspond to $N = -1$ LL. The density of each line in (b) is marked out in (a) by arrows with corresponding colors. (c)Magneto-drag as a function of field at temperature of 240 K, at certain density points along equal density line (shown as * in the insert). Circles are experimental data and solid curve are quadratic fit of the data.

3

Exciton condensation in graphene double-layer

In an electronic double layer (EDL) under strong magnetic fields, filled Landau states in one layer can bind with empty states of the other layer to form exciton condensate. In this chapter, I demonstrate exciton condensation in bilayer graphene double-layers. Driving current in one graphene layer

generates a near-quantized Hall voltage in the other layer, signifying interlayer correlation and exciton superfluidity. Owing to the strong Coulomb coupling across the atomically thin dielectric, $\nu_{tot} = 1$ state in graphene appears at a temperature twenty times higher than previously observed in GaAs double quantum wells. We also observed other integer total filling factor states $\nu_{tot} = 3, -3$. Phase transitions of ν_{tot} can be induced by the perpendicular electric field, due to the tunable quantum Hall ferromagnetism of bilayer graphene. By studying these phase transitions, we comprehend why the exciton condensate phase emerge at certain filling factors under certain displacement fields.

3.1 Quantum Hall drag of $\nu_{tot} = 1$

Quantized Hall drag for $\nu_{tot} = 1$ has been observed in the lowest LLs in GaAs double quantum wells. However, the BEC realized in semiconducting double quantum wells turn out to be rather fragile, with the temperature scale in the sub-Kelvin range (reported gap $\Delta \sim 0.8K$)[47]. This fragility is mainly caused by a relatively large interlayer separation. It is noted that the critical temperature T_c is proportional to the characteristic energy scale $\frac{e^2}{\epsilon l_B}$, where ϵ is the dielectric constant and $l_B = (\hbar/eB)^{1/2}$ is the magnetic length specifying the inter-particle distance in a LL. Also, the exciton BEC only appears in the strong coupling regime, where the d/l_B ratio is below a critical value of $d/l_B < 2$. Thus reducing d substantially below the limit of the semiconducting double quantum well will likely enhance $T_c$as well as increase the exciton binding energy.

The previous chapter showed strong Coulomb drag effect in graphene double-layer heterostructures in the frictional regime at high temperatures. However, cooling that sample to lower tem-

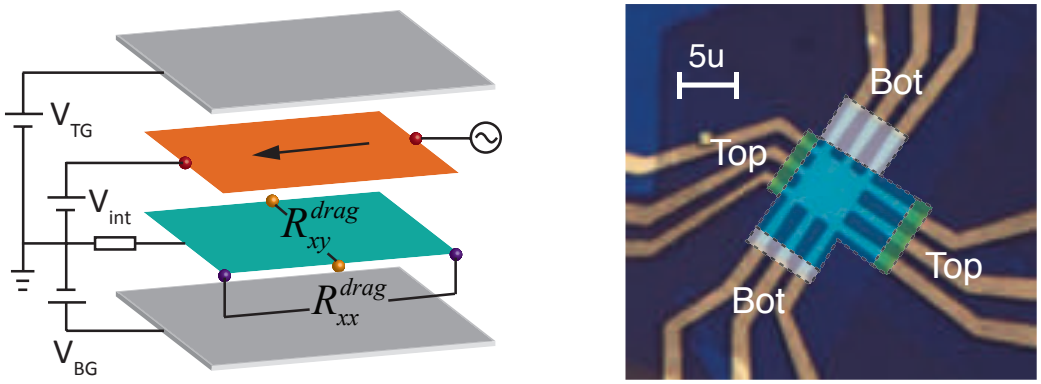

Figure 3.1: Measurement setup (left) and device image (right). In the device image, metal leads on the left and right (three on each side) contact the top layer graphene, while others contact the bottom layer graphene. The blue shaded area of graphene is under the top gate; white and green shaded regions are under the contact gate.

perature, we did not observed signatures of exciton condensation due to sample quality limitation and low contact transparency at low temperatures. In order to overcome these challenges, we improved contact transparency using the contact gates, as described in section 1.4. In Fig. 3.1, white (green) shaded area are later covered with a metal gate (contact gate) controlling lead doping of the bottom (top) layer. These devices are made of two Bernal stacked bilayer graphene (BLG) sheets separated by 3 nm hBN and encapsulated by two thicker hBN layers (between 20nm and 30nm). Both graphene layers have mobility $0.5 - 1 \times 10^6 cm^2/Vs$ and exhibit symmetry breaking quantum Hall states at fields as low as 5T.

The voltages applied to the top gate (V_{TG}), the bottom gate (V_{TG}) and the interlayer bias between graphene layers (V_{int}) tune the carrier densities of the top and bottom graphene layers n_{top}, n_{bot}: $n_{top} = C_{TG}V_{TG} - C_{int}V_{int}$; $n_{bot} = C_{BG}V_{BG} + C_{int}V_{int}$ (assuming V_{int} much smaller than

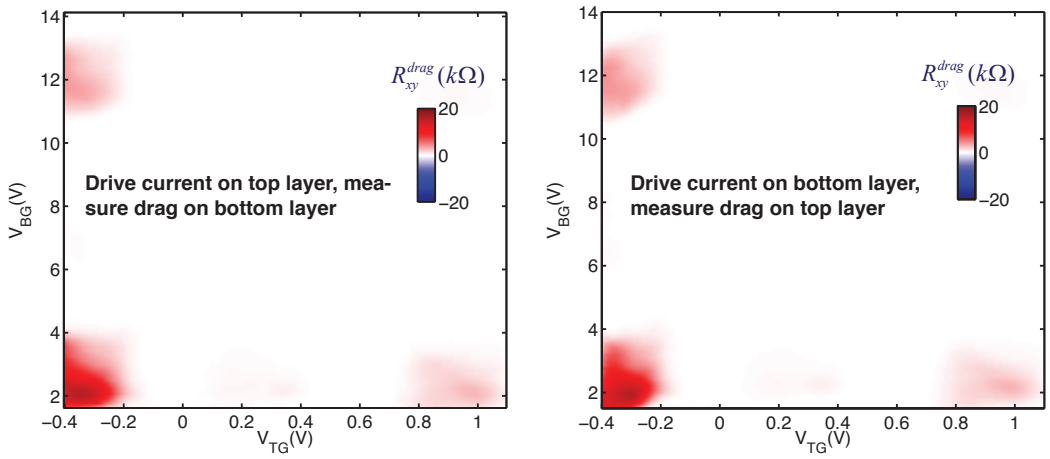

Figure 3.2: Demonstration of Onsager reciprocity. Left panel shows drag measurements performed by driving the top layer and measuring the Hall drag voltage in the bottom layer at B=13T. Right panel shows a reciprocal configuration, i.e., driving the bottom layer and measuring the Hall drag voltage on the top layer (right panel) at B=-13T. Temperature is fixed to 1.5 K. Both experiments yield almost identical results.

V_{TG} and V_{BG}). Here C_{TG}, $C_{BG}$and $C_{int}$are capacitances between the top gate and top layer, the bottom gate and bottom layer, and between the top and bottom graphene layers, respectively. By controlling V_{TG}, V_{BG}, and V_{int}, we can also adjust the average displacement fields on each layer: $D_{top} = (C_{TG}V_{TG} + C_{int}V_{int})/2, D_{bot} = (-C_{BG}V_{BG} + C_{int}V_{int})/2$. We perform Coulomb drag measurements similar to the one in last chapter: R_{xy}^{drive} is the Hall resistance of the drive layer, R_{xx}^{drag} and R_{xy}^{drag} are magneto- and Hall drag resistance. Owning to Onsager relation, it does not matter whether we use the top or bottom layer as the drive layer. Fig. 3.2 shows that exchanging the drive and drag layer measurement configuration yields nearly identical results under opposite magnetic field directions.

Fig. 3.3 shows measurements of R_{xy}^{drive}, $-R_{xx}^{drag}$, R_{xy}^{drag} under B = 25 T, corresponding to the strong coupling limit ($l_B = 5.1$ nm and $d/l_B = 0.58$). In this plot, we adjust V_{TG} and V_{BG} such

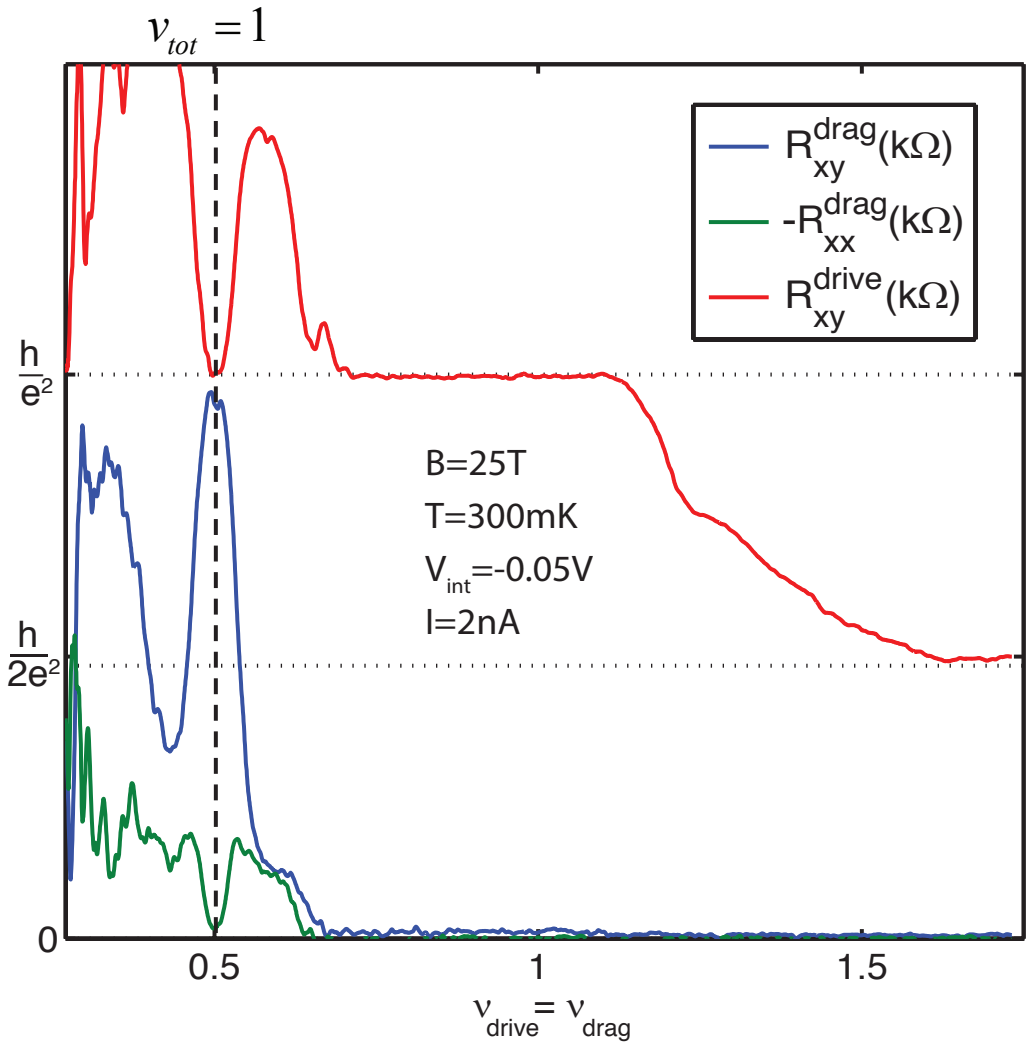

Figure 3.3: $R_{xy}^{drag}, -R_{xx}^{drag}, R_{xy}^{drive}$ as a function of filling factors of both layers at B=25T and T=300mK. The exciton BEC can be recognized by near quantized Hall drag ($R_{xy}^{drag} = \frac{h}{e^2}, R_{xx}^{drag} = 0$) with the simultaneous re-entrant quantum Hall in the drive layer.

that the filling fractions of the two layers are balanced ($\nu_{eq} \equiv \nu_{drive} = \nu_{drag}$). We observe that each layer exhibits its own quantum Hall effect. For $\nu_{eq} \geq 1$, R_{xy}^{drive} exhibit QH plateaus at the values $(R_{xy}^{drive})^{-1} = e^2/h, 4e^2/3h, 2e^2/h$. In these well-developed integer and fractional quantum Hall effect of the individual layers, we find no appreciable drag signal ($R_{xx}^{drag} \approx R_{xy}^{drag} \approx 0$). The vanishing drag signals at low temperatures are expected in the semiclassical picture due to the diminishing scattering phase space. However, the observed drag signals are significantly enhanced when the first LL of both layers are partially filled ($\nu_{eq} < 1$). In particular, for $\nu_{eq} = 1/2$ where both layers are half-filled and thus $\nu_{tot} = \nu_{drive} + \nu_{drag} = 1$, the Hall drag signal reaches close to the quantization value of $h/e^2 = 25.8k\Omega$, while the magneto-drag (R_{xx}^{drag}) dips to nearly zero. Under the same condition, the Hall resistance in the drive (top) layer, which originally rises beyond h/e^2 as ν_{drive} drops below one (i.e., partially filled LL), re-enters h/e^2 again at $\nu_{tot} = 1$. This re-entrant behavior of R_{xy}^{drive} to the same quantized value of R_{xy}^{drag} indicates that the entire double-layer behaves like a single $\nu = 1$ quantum Hall system despite that LLs in each layer are only partially filled.

The quantized Hall drag and re-entrant QHE in the drive layer are considered as strong evidences of interlayer coherence. A simple physical picture for the observed quantized Hall drag can be built upon a two-fluid picture[23] (Fig. 3.4). In this model, currents in each layer are carried by excitons in the bulk ($I_{ex}^{(i)}$) and quasi-particles flowing on the edge ($I_{qp}^{(i)}$), where the superscript i is the layer index. Excitons generate counter flow currents $I_{ex}^{drag} = -I_{ex}^{drive}$; and the zero accelerating electric force requirement on superfluid excitons demands $V_{xy}^{drive} = V_{xy}^{drag} = V_{xy}$. In addition, boundary conditions of the drag and drive layers requires $I_{ex}^{drag} + I_{qp}^{drag} = 0, I = I_{ex}^{drive} + I_{qp}^{drive}$. Furthermore, by considering the two layers as a single coherent quantum Hall system at filling frac-

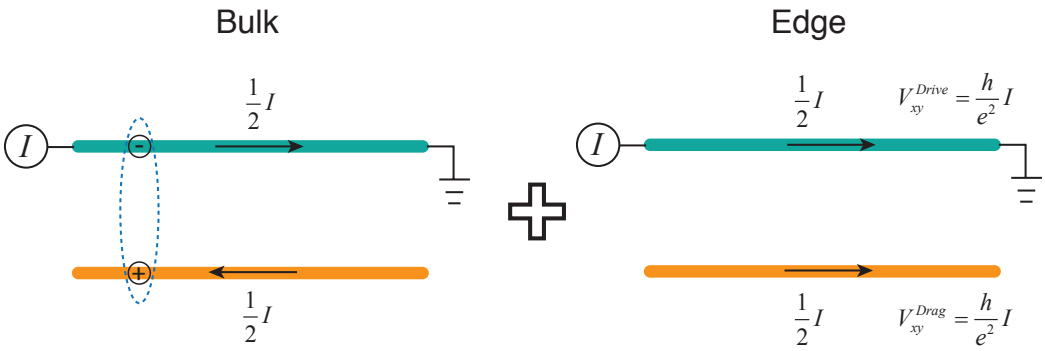

Figure 3.4: Two fluid model for quantized Hall drag. The drag measurement have been disintegrated into two conducting components: edge and bulk. On the drag layer, this two components cancel to get zero current. On the drive layer, they combine to the drive current I.

tion $\nu_{tot} = 1$, we have $I_{qp} = I_{qp}^{drag} + I_{qp}^{drive} = (\nu_{tot}e^2/h)V_{xy}$. Summing up, we obtain the experimental observation $R_{xy}^{drive} = R_{xy}^{drag} = h/\nu_{tot}e^2$ with vanishing $R_{xx}^{drag}$and R_{xx}^{drive}.

Observed $R_{drive} = R_{drag}$ also indicates that the excitons formed a superfluid. Normally, zero counterlflow resistance is needed to demonstrate exciton superfluidity. However, in the linear response regime, counterflow resistance R_{xx}^{CF} and R_{xy}^{CF} can be extracted from the Coulomb drag measurements. According to linear response theory, the voltage drop (either in longitudinal or Hall direction) V^j on each layer (j = 1 or 2 is layer index, 1 represent top layer, 2 represent bottom layer) is proportional to currents on the two layers I^j, as expressed by the following equation:

$$\begin{pmatrix} V^1 \\ V^2 \end{pmatrix} = \begin{pmatrix} R^{11} & R^{12} \\ R^{21} & R^{22} \end{pmatrix} \begin{pmatrix} I^1 \\ I^2 \end{pmatrix} \tag{3.1}$$

By setting the boundary condition in the above equation to $I^1 = I$ and $I^2 = 0$, we note that R^{11}

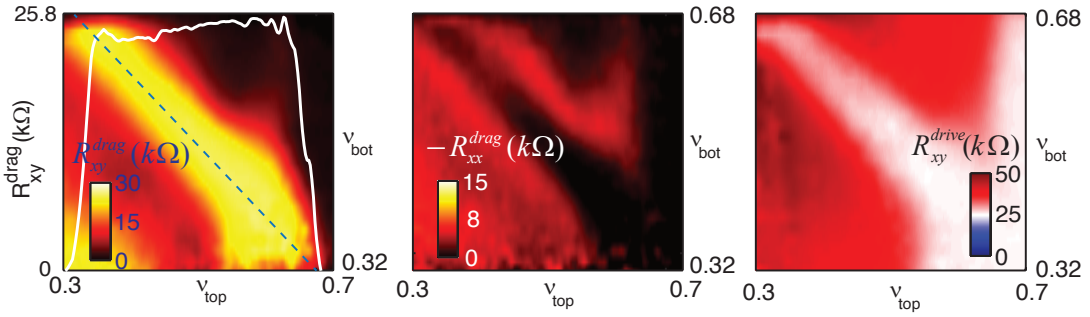

Figure 3.5: R_{xy}^{drag}, $-R_{xx}^{drag}$, R_{xy}^{drive} as a function of filling fractions ν_{top} and ν_{bot}, computed from V_{TG} and V_{BG}. The exciton BEC region appears as a diagonal strip satisfying $]\nu_{top} + \nu_{bot} = 1$. The white trace on the left shows the value of R_{xy}^{drag} (axis on the left) along $\upsilon_{tot} = 1$ line (dashed blue line).

is the resistance of the top layer and R^{21} equals the drag resistance. In the counterflow setup, the current boundary condition is set to $I^1 = -I^2 = I$. Thus, the counterflow resistance on the top layer is $R_{xx}^{CF} = R_{xx}^{top} - R_{xx}^{drag}$ and $R_{xy}^{CF} = R_{xy}^{top} - R_{xy}^{drag}$, which is zero when the drive layer resistance equals drag layer resistance.

The exciton BEC in graphene is can withstand the density imbalance between the two layers, as long as totally filling factor is one. The signatures of the exciton condensation, i.e., $R_{xy}^{drag} \approx R_{xy}^{drive} \approx h/e^2$and $R_{xx}^{drag} \approx R_{xx}^{drive} \approx 0$ withstand a range of gate voltages satisfying $\nu_{drag} + \nu_{drive} = 1$, corresponding to the diagonal line shown in Fig. 3.5 (blue dashed line in the left panel). For a more quantitative analysis, we plot R_{xy}^{drag} cut along this diagonal line as an overlay graph in Fig. 3.5 left (white trace). The level of R_{xy}^{drag} quantization indicates that the BEC persists for the density imbalance $\Delta n/n_{tot} = (n_{drag} - n_{drive})/(n_{drag} + n_{drive})$ up to $\sim \pm 30\%$. Beyond this limit the more stable integer QH states ($\nu_{drag}, \nu_{drive} = 0, 1$) in each layer take over the exciton BEC phase.

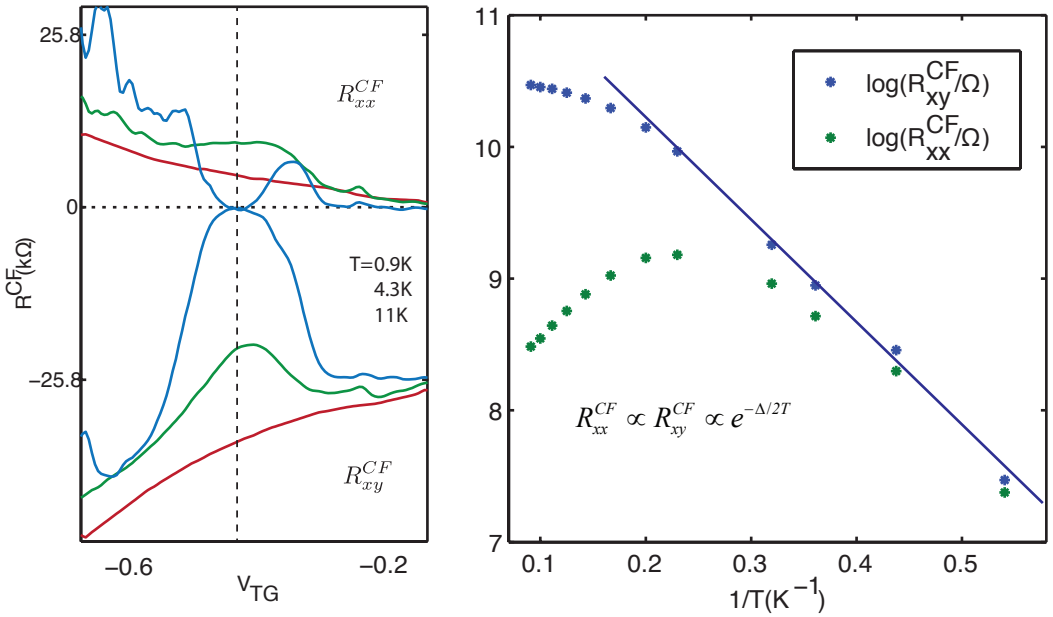

Figure 3.6: Left, calculated counterflow resistance on the top layer as a function of top gate voltage across $\nu_{tot} = 1$ (vertical dashed line) at different temperatures under B=25T. The traces above zero shows R^{CF}_{xx} while the traces below zero shows R^{CF}_{xy}. Right, counterflow resistance as a function of 1/T at $\nu_{tot} = 1$. Blue line marked Arrhenius fit with the gap energy of 16K.

We found that the observed quantized Hall drag in graphene is much more robust than that of the GaAs double quantum wells. The signatures of the exciton condensate, i.e., nearly quantized R_{xy}^{drag} and re-entry behavior of R_{xy}^{drive}, persist up to a few Kelvin for $\nu_{tot} = 1$. For quantitative analysis, we compute the counter-flow resistances R_{xy}^{CF} and R_{xx}^{CF} using Eq. 3.1 and plot them as a function of $1/T$ at $\nu_{tot} = 1$ (Fig. 3.6). While the theoretical expectation for 2D BEC transition is the Kosterlitz-Thouless transition, we find that the vanishing R_{xy}^{CF} and R_{xx}^{CF} exhibit a thermally activating behavior similar to what has been observed in GaAs system. However, the activation gap we obtained $\Delta \approx 16$K is twenty times larger than previous reported.

3.2 Interlayer correlated states at $\nu_{tot} \neq 1$

While the exciton BEC has been discovered only for the half-filled lowest LL in the GaAs double quantum wells, the gate tunability in graphene double-layer devices allows us to explore the phase diagram of possible condensate states other than $\nu_{tot} = 1$. Fig. 3.7 shows experimental survey for R_{xy}^{drag} as a function of ν_{drive} and ν_{drag}, covering the electron-electron ($\nu_{drive}, \nu_{drag} > 0$) and hole-hole ($\nu_{drive}, \nu_{drag} < 0$) regimes. Remarkably, we find at least two additional interlayer correlated states in these regimes: (ν_{drive}, ν_{drag}) centered near ~(0.5, 2.5) and (-1.5, -1.5), corresponding to the drag between $^1/_2$ - $2^1/_2$ filled electron LLs ($\nu_{tot} = 3$) and $1^1/_2$ - $1^1/_2$ filled hole LLs ($\nu_{tot} = -3$), respectively.

Similar to the BEC in $\nu_{tot} = 1$, these states exhibit the near-quantized Hall drag $R_{xy}^{drag} \approx h/\nu_{tot}e^2$and $R_{xx}^{drag} \approx 0$, for a range of (ν_{drive}, ν_{drag}) satisfying $\nu_{drive} + \nu_{drag} = \nu_{tot}$ (Fig. 3.8

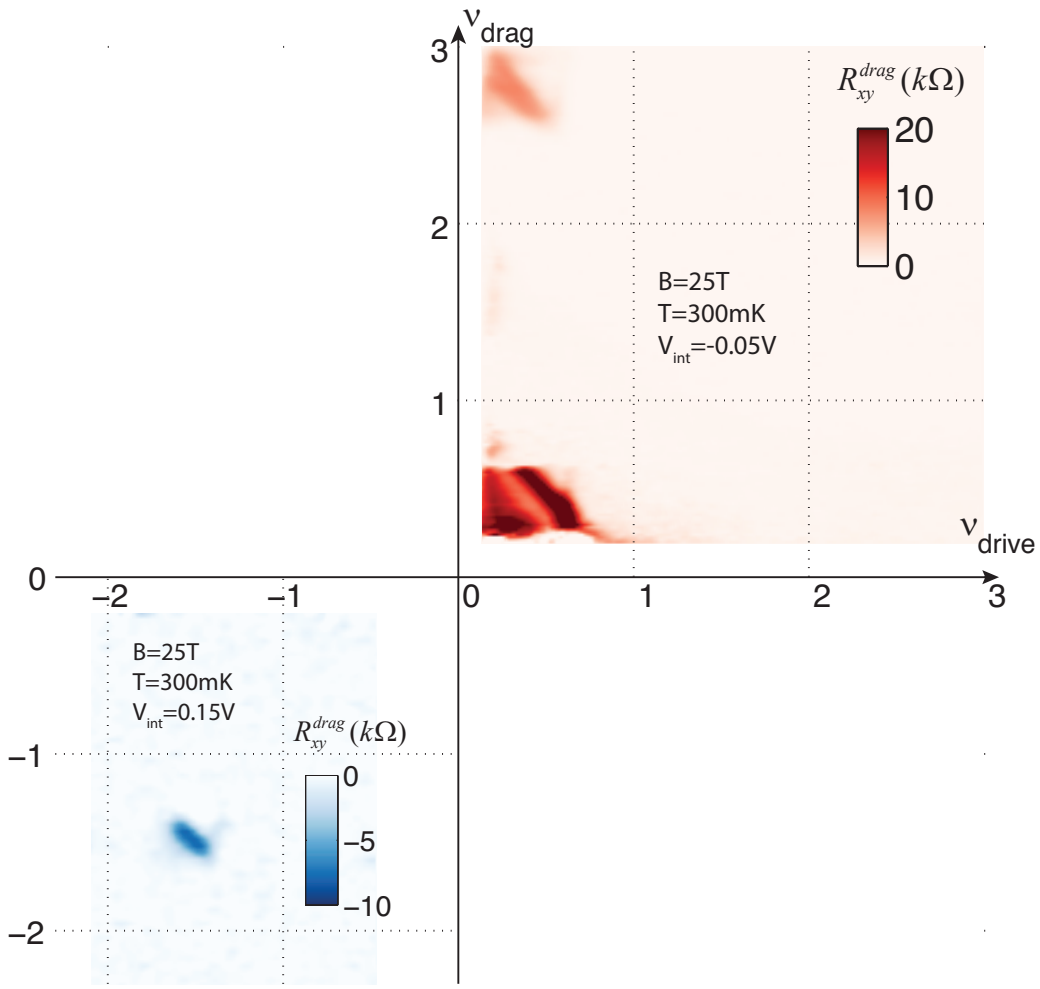

Figure 3.7: R_{xy}^{drag} as a function of the top and bottom layer filling factors at B=25T, T=300mK and $V_{int} = -0.05V$ (electron-electron part) and $V_{int} = 0.15V$ (hole-hole part). Besides $(\nu_{drag}, \nu_{drive}) = (0.5, 0.5)$, additional exciton BEC state is found near $(\nu_{drag}, \nu_{drive}) = (0.5, 2.5)$ and $(-1.5, -1.5)$.

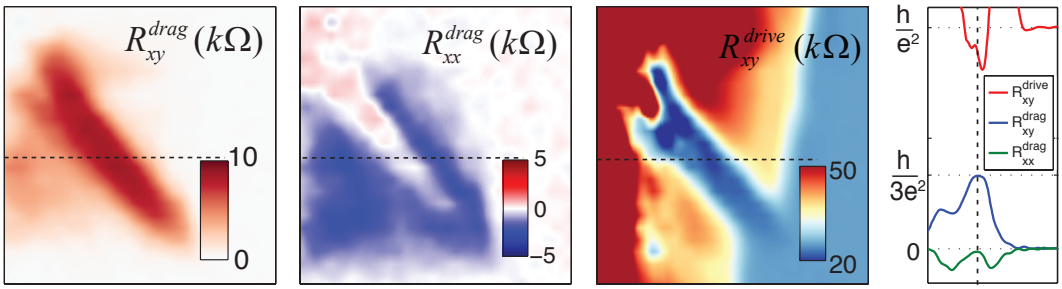

Figure 3.8: Color plots, zoomed-in plot of R_{xy}^{drag}, R_{xx}^{drag}, R_{xy}^{drive} around $\nu_{tot} = 3$ at a higher field of B=31T. Last panel, line-cut of R_{xy}^{drag}, R_{xx}^{drag}, R_{xy}^{drive} along dashed line show in the left color plots.

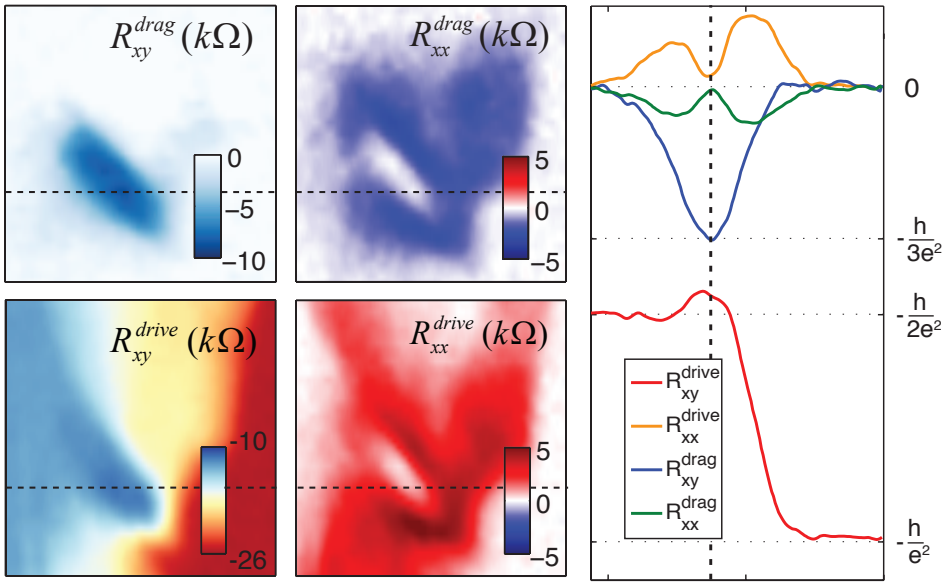

Figure 3.9: Color plots, zoomed-in plot of R_{xy}^{drag}, R_{xx}^{drag}, R_{xy}^{drive}, R_{xx}^{drive} around $\nu_{tot} = -3$ at B=25T. Right panel, line-cut of R_{xy}^{drag}, R_{xx}^{drag}, R_{xy}^{drive}, R_{xx}^{drive} along dashed line show in the left color plots.

and Fig. 3.9). These quantized Hall drag features appear as diagonals in the (ν_{drive}, ν_{drag}) plots and are confined to the sectors corresponding to partially filled first (drive) and third (drag) electron LLs (with all symmetries are lifted) and partially filled second (drive and drag) hole LLs. We interpret these interlayer correlated states as exciton BEC for $\nu_{tot} = \pm 3$. Measurements at lower magnetic fields also reveal a signature of developing exciton BEC for (ν_{drive}, ν_{drag})=(2.5, 0.5), the symmetric pair for (0.5, 2.5) discussed above (Fig. 3.10). The relatively weak presence of this symmetric pair is presumably due to the quality difference between the top and bottom graphene layers. We also note that while $R_{xy}^{drag} \approx h/\nu_{tot}e^2$and $R_{xx}^{drive} \approx R_{xx}^{drag} \approx 0$ are observed in the $\nu_{tot} = \pm 3$ state, we find $|R_{xy}^{drive}| > h/\nu_{tot}e^2$(Fig. 3.8 and Fig. 3.9). Together with less developed quantization of R_{xy}^{drag} in these states, compared to $\nu_{tot} = 1$, we speculate that a dissipative exciton transport of a fragile BEC is responsible for this incomplete re-entrant QHE.

Interestingly, our experimental observations strongly indicate that the electron-hole symmetry of LLs is apparently broken for the exciton BEC. For example, the (0.5, 0.5) BEC exists while (-0.5, -0.5) is absent. Electron-hole asymmetry has been observed in the filling fraction sequences of the fractional quantum Hall effect in bilayer graphene and is related with the structure of symmetry-broken quantum Hall state in bilayer graphene. We will present a explanation of why certain states exist while others do not in the next section.

3.3 Phase transiton induced by displacement fields

We note that the existence of the exciton BEC at fixed $(\nu_{drive}, \nu_{drag})$ sensitively depends on the V_{int}. In Fig. 3.10 and Fig. 3.11, in the same filling factor range, the strong Hall drag only happen in certain interlayer bias windows. To understand what causes the dependence on interlayer bias, we take a closer look at the $\nu_{tot} = 1$ state. In Fig. 3.12, we observe that R_{xy}^{drag} undergoes multiple distinct transitions between high and low values as V_{int} changes, while filling factors stay the same. When the density of each layer is kept close to half-filling by coordinately tuning V_{BG} and V_{TG}, V_{int} changes the displacement field exerted on both layers, $D_{top} = C_{int}V_{int} + n_{top}/2$ and $D_{bot} = C_{int}V_{int} - n_{bot}/2$. Calculating displacement fields using these formula, Fig. 3.14 shows R_{xy}^{drag} as a function of D_{top} (top axis of Fig. 3.14) and D_{bot} (bottom axis of Fig. 3.14). By comparing the displacement fields of these transitions with those of the integer quantum Hall transitions of each layer, we found a close connection between the Hall drag and the LL characters of each layer.

3.4 Selection rules for LLs to establish exciton BEC

For a single bilayer graphene, the lowest Landau level (LLL) have eight-fold degeneracy in the single particle picture (between $\nu = -4$ and $\nu = 4$). This SU(8) symmetry space consists of spin degeneracy $|\uparrow\rangle$ and $|\downarrow\rangle$, valley degeneracy K and K' and orbital degeneracy of $N = 0, 1$. In high quality samples, these symmetries are broken by quantum Hall ferromagnetism (QHFM), and different symmetry-breaking states can be found at different displacement fields for each filling factor. The symmetry-breaking state $\nu = 1$ has three transition points at $D = 0$ and $D = \pm D_1$, and $\nu = 0$

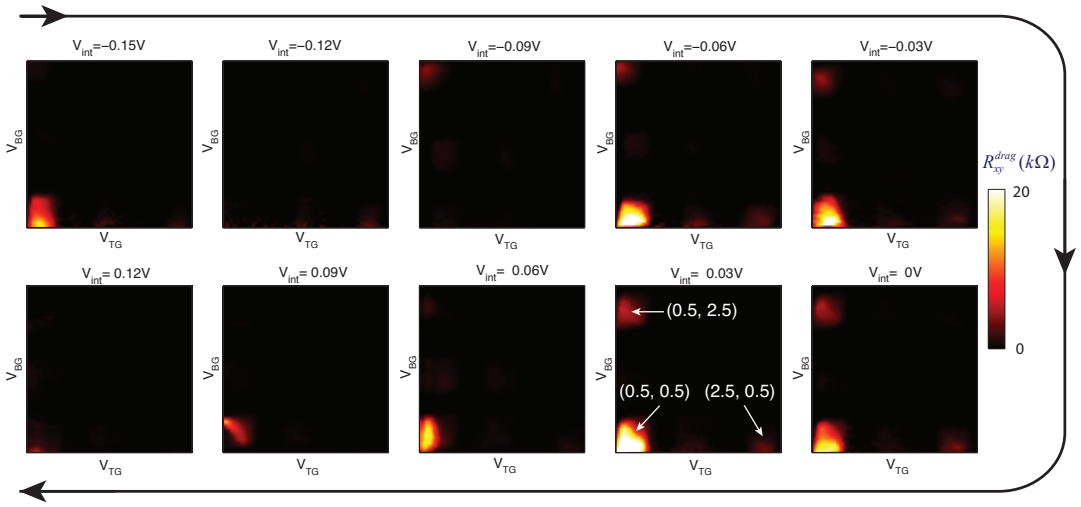

Figure 3.10: Hall drag resistance as function of gate voltages at different interlayer biases at B=13T and T=1.5K in the electron-electron regime (all plots shows same filling factor range $0 < \nu_{top}, \nu_{bot} < 3$). The numbers marked in V_{int} = 0.03V plot indicate (ν_{drive}, ν_{drag}) values.

has four transition points at $D = \pm D_2, \pm D_3$, which can be identified in Fig. 3.14. Across these transitions, the fully filled LLs have different spin, valley or orbital indexes. For partially filled LLs, layer polarization and orbital character were identified by a recent study using capacitance measurements[15]. The partially filled LL $0 < \nu < 1$ is found to hold different layer- and orbital-polarized states at different displacement fields (Fig. 3.13) (+/- denote the layer polarization, which is equivalent to valley polarization K/K' in the lowest LL, and 0/1 denote the orbital index).

Intriguingly, the transitions between these states line up with the transitions of $\nu = 1$ and $\nu = 0$ states regarding to displacement field. In our experiment, the $\nu_{tot} = 1$ state is formed between two partially filled bilayer graphene with $0 < \nu_{top}, \nu_{bot} < 1$. We found that Hall drag is suppressed when the partially filled LLs of one bilayer graphene or both bilayer graphene are in the N=1 orbital state (shaded regions in Fig. 3.14). This also explains the absence of other integer total filling factor

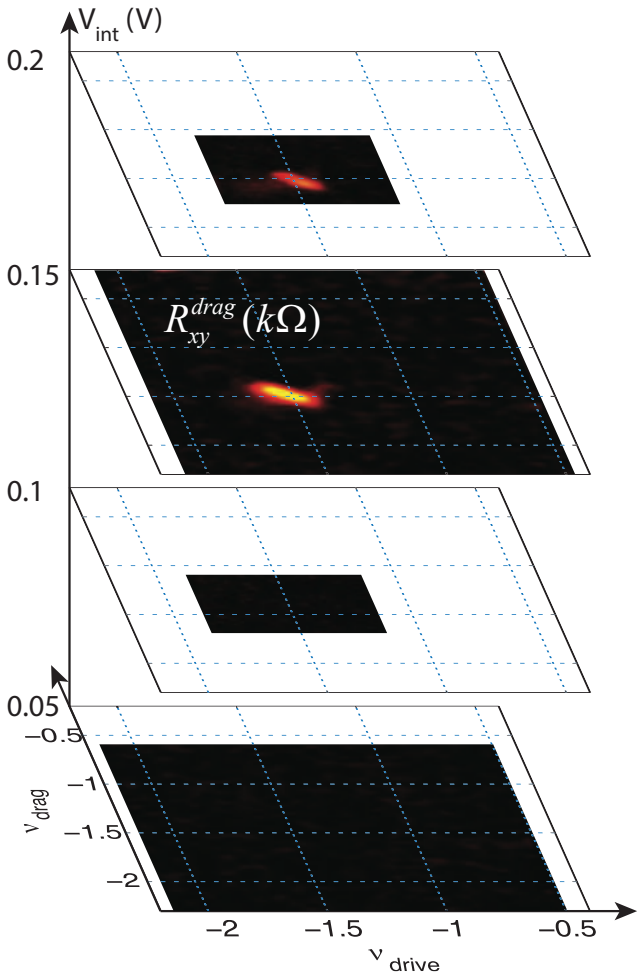

Figure 3.11: Hall drag resistance as function of drive and drag filling factor at different interlayer bias at B=25T and T=0.3 K in the hole-hole drag regime.

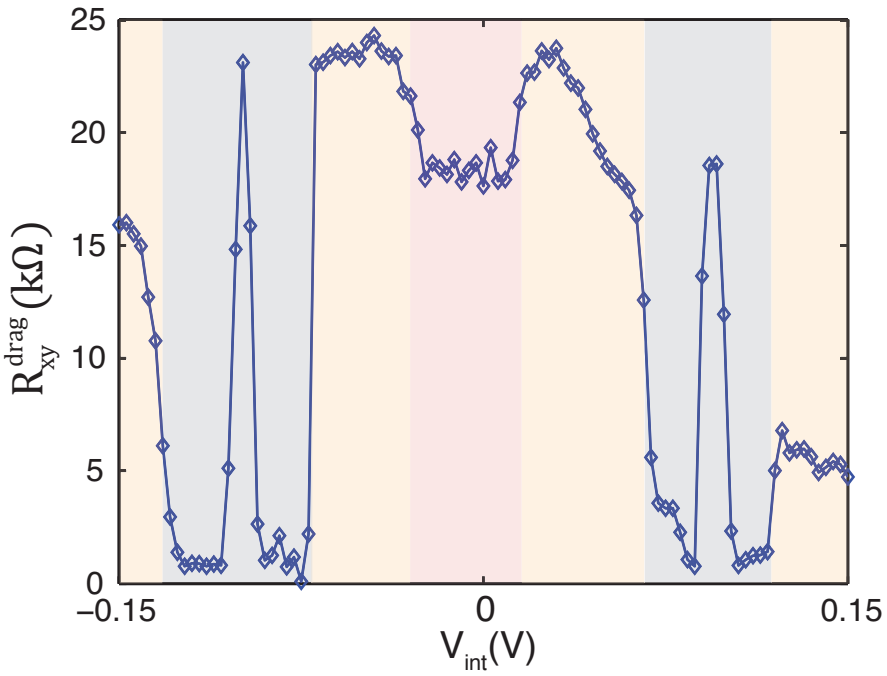

Figure 3.12: Hall drag vs V_{int} at $\nu_{eq} = 1/2$ at B=13T and T=1.5K.

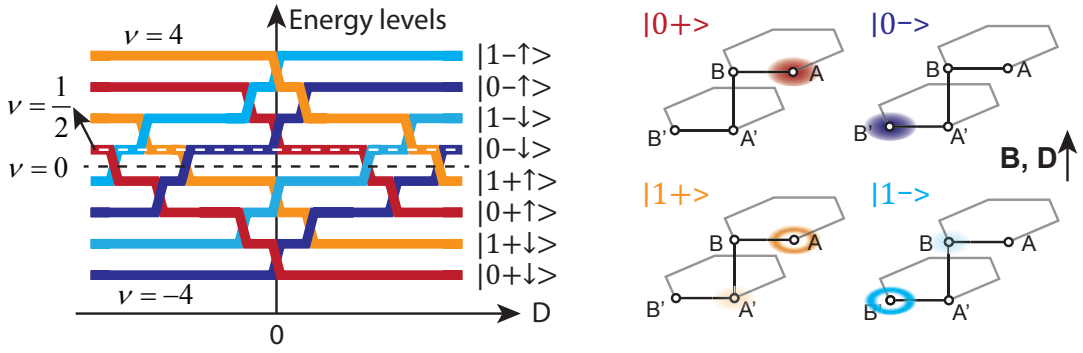

Figure 3.13: Schematic diagram of Landau levels sequence (left) and wave functions (right) of bilayer graphene quantum Hall ferromagnetic (QHFM) states for the lowest LL corresponding to $-4 < \nu < 4$. In the left diagram, x direction represents displacement field *D* and colored lines denote QHFM Landau levels with different orbital (0/1), layer (+/-) and spin ($\uparrow$ / $\downarrow$) quantum numbers, as noted next to the lines. Different colors are used for different orbital and layer quantum numbers. As the displacement field changes, the colored lines cross each other, representing QHFM transitions induced by the displacement field. The horizontal black dashed line marks charge neutrality ($\nu = 0$) and the horizontal white dashed line marks Fermi level of half-filled first LL ($\nu = 1/2$). The diagram on the right depicts wave functions of different bilayer graphene QHFM states, with matching color code as the lines in the left diagram.

states and the broken electron-hole symmetry, as the $-1 < \nu < 0\,(0 < \nu < 1)$ LL is polarized in the $N = 1\,(N = 0)$ orbital state under the same displacement field; the latter is capable of forming an exciton BEC while the former is not. We speculate that the inability of the $N = 1$ orbit to establish an interlayer correlated state is due to its broader spatial wavefunction (Fig. 3.13 right) and thus weaker interaction. Similarly, the weaker Hall drag signal in the region where $D_{top} > 0$ and $D_{bot} < 0$ can be related to the weaker interaction when the wavefunctions of the two layers are further apart due to the opposite layer polarization.

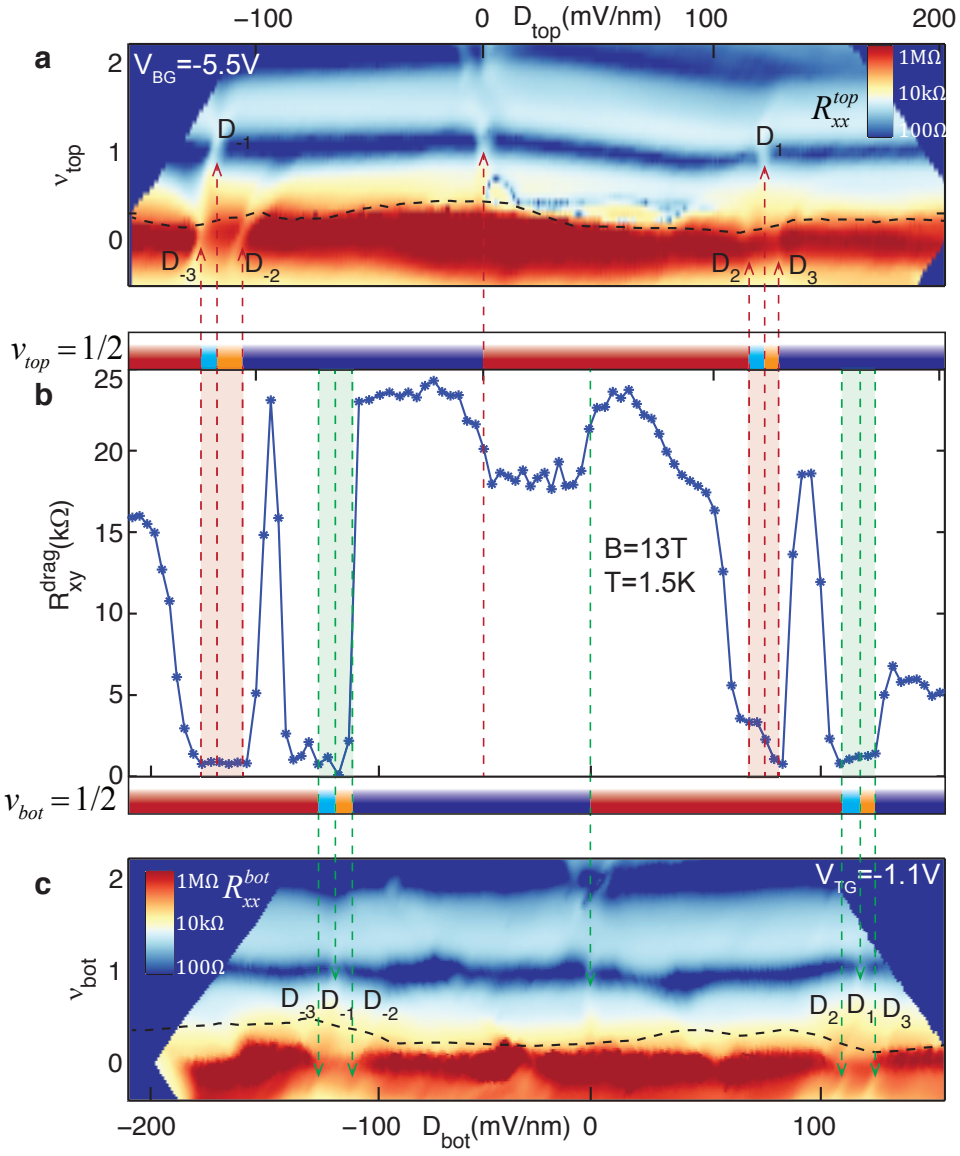

Figure 3.14: Top and bottom panels, longitudinal resistance of top (bottom) bilayer graphene as a function of displacement D_{top} (D_{bot}) and density n_{top} (n_{bot}) at B =13T and T=1.5K. The QHFM transitions are marked with arrows. Middle panel, R_{xy}^{drag} (blue curve) as a function of D_{top} (top axis of the top panel) or D_{bot} (bottom axis of the bottom panel) for $\nu_{tot} = 1$ state at B=13T and T=1.5K. The colored bars on the top and bottom of this plot represent orbital and layer character of the half-filled LL ($\nu = 1/2$) of the top and bottom bilayer graphene with the same color code as Fig. 3.13. The orange and green shaded regions of the main plot which signify N=1 orbital states of the top and bottom layer coincide well with where the Hall drag vanishes, indicating N=1 orbit is incapable of forming exciton BEC phase.

4

$\nu = 0$ Exciton insulator

In the previous chapter, we demonstrated exciton condensates between quasi-electrons and quasi-holes in a graphene double-layer that are electron-electron or hole-hole doped. Although various signatures are used to show that the bulk indeed behave like an exciton condensation, the existence of additional conducting channels on the edge complicates transport behaviors and differentiates it from the exciton condensation formed by real electrons and holes. An exciton condensate formed

by real electrons and holes is an electrical insulator due to the charge neutral nature of excitons, instead of being a correlated quantum Hall state.

In this chapter, I present observation of exciton insulator state between electron-doped and hole-doped graphene layers under strong magnetic fields, when the electron density of one layer matches the hole density of the other. Although magnetic field is still required to stabilize this state, the effect of magnetic field is simply flattening the band for enhancing interaction effect (Fig. 4.1 right). As the excitons are formed by real electrons and holes, instead of quasi-particles, the physics and transport signatures are much closer to that of zero field EC than $\nu_{tot} = 1$ state. At total density $n_{tot} = 0$, one graphene is insulating if the other graphene layer is open-circuit. However, when the circuit of the second layer is closed, the first layer become conducting and a perfect drag current arises in the second layer. Measurement with counterflow current shows vanishing longitudinal and Hall resistance and suggest this $n_{tot} = 0$ state is an exciton condensate.

4.1 The correlated insulator

Device used here is compose of two monolayer graphene layers separated by a 3.7nm hBN. We chose monolayer graphene for this study because of its simpler quantum Hall ferromagnetic Landau level (LL) structure and the electron-hole symmetry. In the previous chapter, we found that only $N = 0$ LLs are capable of forming exciton condensate. As the lowest symmetry-broken LLs ($-2 < \nu < 2$) of monolayer graphene consist solely of $N = 0$ orbital state, it will then be possible to achieve an exciton condensate between the first electron LL of one layer and the first hole LL of the other. We

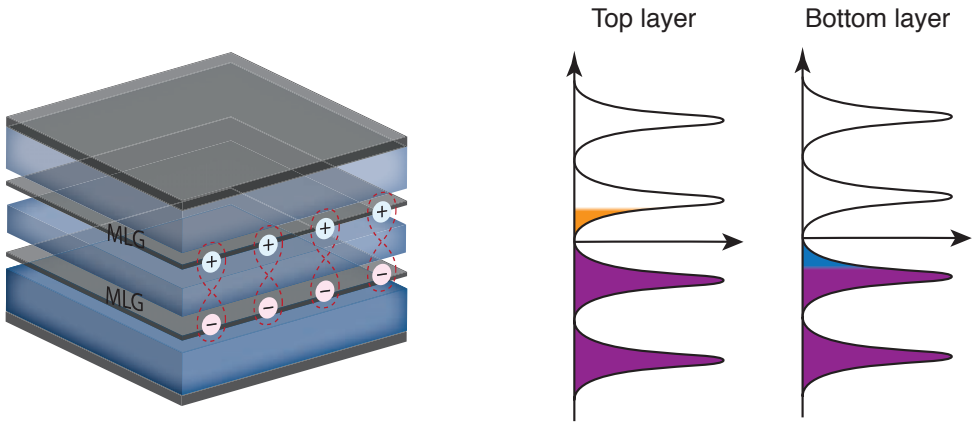

Figure 4.1: Left, schematic for interlayer exciton. MLG stand for monolayer graphene. Top layer is hole-doped, while bottom layer is doped with electrons at the same density. Right, illustration of excitons between electrons and holes under magnetic fields. The magnetic fields flatten the band structure into LLs, enhancing interaction effect. Electrons on the top layer (orange color) bind with holes in the bottom layer (blue color) to form interlayer excitons.

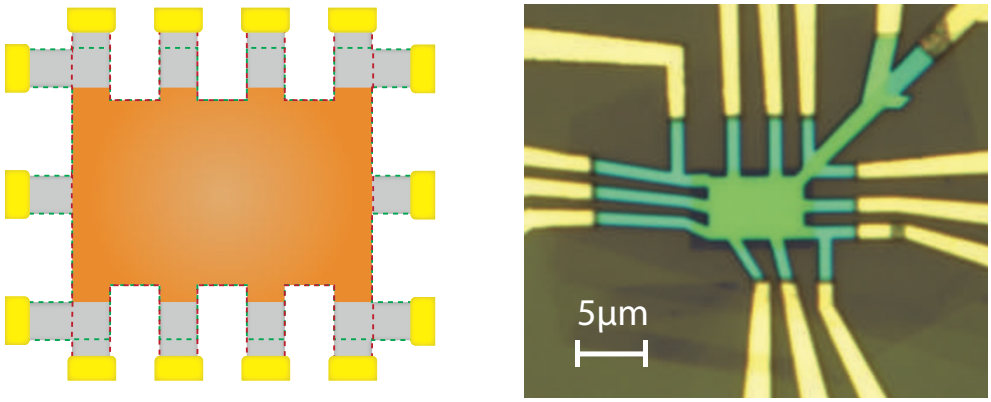

Figure 4.2: Left, illustraction of device scheme. The orange part represent the channel, while grey areas are the graphene leads between channel and metal contact (golden color). Grean (red) dashed lines indicate the boundary of the top (bottom) graphene layer. Yellow depicts gold contacts. Right, optical image.

also advanced our devices architecture to the one with dual-graphite gates (pre-patterned bottom graphite). We fabricate electrical contacts onto each layer but leave a gap between the channel and the metal contacts (grey area in Fig. 4.2 left), so the lead can be gated separately to improve transparency. We use the silicon back gate and contact gates to heavily dope the lead of both layers to high carrier density but matching carrier types with the channel. It is important to note that for the leads at the corners, top and bottom graphene leads share the same path until it reaches the heavily doped part next to the contact. This corner leads are used as current source and drain and are especially important for the perfect current drag and counterflow experiments, as we will discuss later.

First we performed Coulomb drag measurements at B=14T and T=1.8K. Fig. 4.3 shows longitudinal drag resistance (R_{xx}^{drag}), Hall drag resistance (R_{xy}^{drag}) and longitudinal resistance of the drive layer (R_{xx}^{drive}) as a function of top and bottom layer filling factors. In the Hall drag diagram, a checker board pattern emerges. From chapter two, we know that these strong Hall drag regions are separated by integer quantum Hall states of each layer. The quantum Hall states of each layer cut the Hall drag diagram into sixteen regions with strong interlayer correlation, which is present between any pair of partially filled LLs with integer total filling factors $\nu_{tot} = 0, \pm1, \pm2, \pm3$. All these sixteen states are allow to present because they all occur between two N=0 LLs. For the interlayer correlated state $\nu_{tot} = \pm1, \pm2, \pm3$, we found the Hall drag is close to the expected quantization value of $R_{xy}^{drag} = h/\nu_{tot}e^2$.

$\nu_{tot} = 0$, however, is a special case. Following $R_{xy}^{drag} = R_{xy}^{drive} = h/\nu_{tot}e^2$, we should expect a diverging Hall resistance. This is because for $\nu_{tot} = 0$, there is no edge state, thus the system should be behave as an insulator in the Coulomb drag setup. Indeed, out of the sixteen interlayer correlated

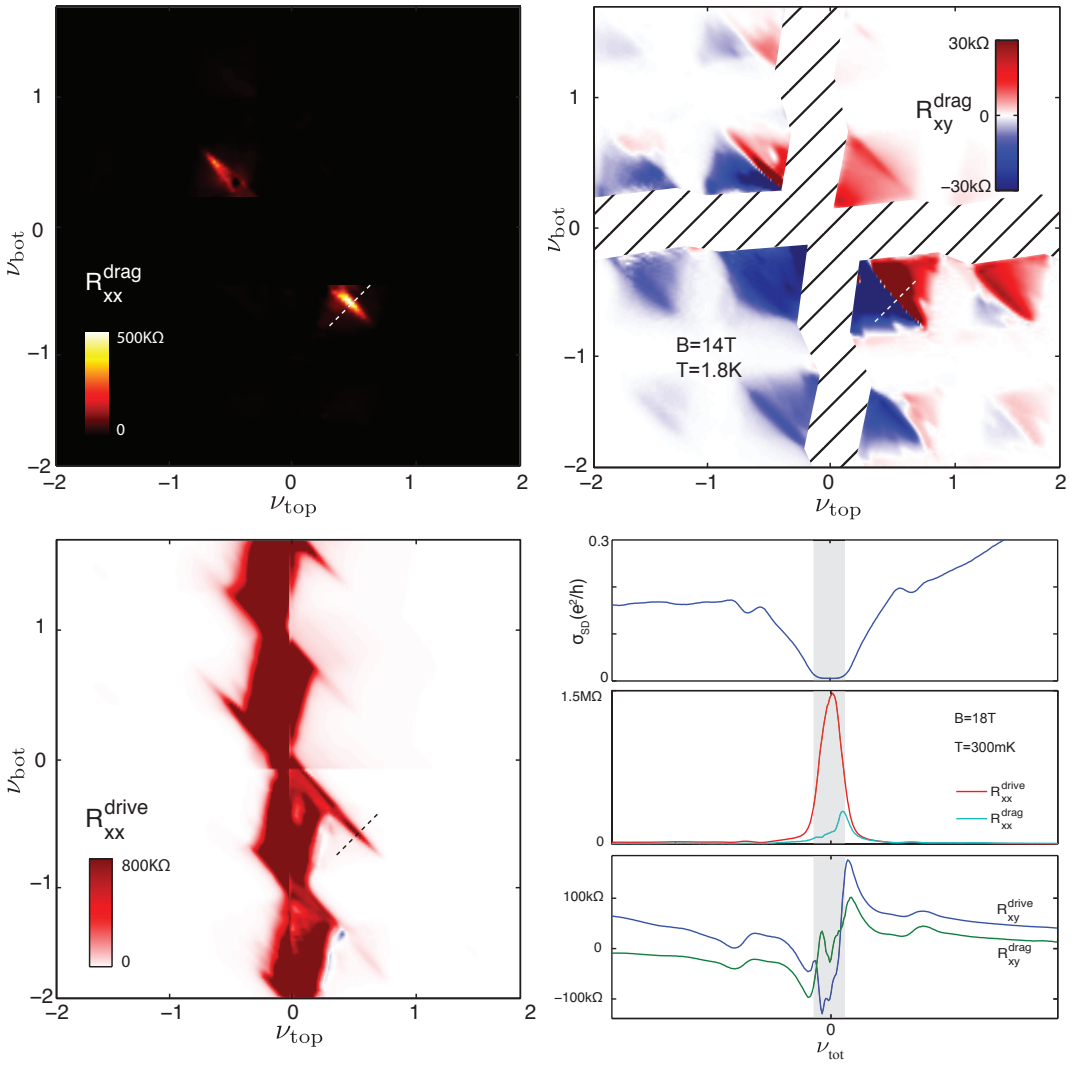

Figure 4.3: R_{xx}^{drag}, R_{xy}^{drag}, and R_{xx}^{drive} as a function of top and bottom layer filling factor. When each layer form its own $\nu = 0$ quantum Hall plateau around charge neutral point, the measurement become unreliable. So $\nu = 0$ regions of each layer are crossed out in R_{xy}^{drag} plot to avoid confusion. The dashed line marks the linecut position of the last panel. Bottom right panel, linecut of two-terminal source-drain conductance σ_{SD}, $R_{xx}^{drag,drive}$ and $R_{xy}^{drag,drive}$ along the dashed line shown in the color plots.

states, two particular states in Fig. 4.3, stand out with exceptional large R_{xx}^{drag}. They correspond to $\nu_{tot} = \nu_{top} + \nu_{bot} = 0$ between first electron LL of one layer and first hole LL of the other layer. This strong R_{xx}^{drag} response ($> 500k\Omega$) is are absent for any other part of the diagram. Taking a linecut across a $\nu_{tot} = 0$ state, we plot the two terminal conductance σ_{SD}, longitudinal resistance of both layers and Hall resistance of both layers. The diverging R_{xx}^{drag} is accompanied by a insulating behavior in the drive layer ($R_{xx}^{drive} > 1M\Omega$, Fig. 4.3) as well. This point is further illustrated by the two-terminal source-drain conductance σ_{SD}, which vanishes near $\nu_{tot} = 0$. Across $\nu_{tot} = 0$, Hall resistances of both layers R_{xy}^{drag} and R_{xy}^{drive} change sign. This is similar to sign change of Hall resistance in a single graphene layer across the charge neutral point. However, when it behaves like an insulator at $\nu_{tot} = 0$, there are large number of carriers ($\approx 1.5 \times 10^{11} cm^{-2}$) in both layers. Because all the carriers are paired up between two layers, carriers in one layer cannot move without being accompanied by the same movement of coupled carriers in the other layer. In the Coulomb drag measurement, the drag layer is open-circuit, and thus the carriers in the drag layer are fixed. The combination of exciton formation and carrier immobilization in the drag layer causes the insulating behavior in this particular measurement.

When we close the circuit on the drag layer, transport property of the entire system changes. Owning to the interlayer correlation, the boundary condition imposed on one layer affects transport behavior of the other layer as well. In Fig. 4.4, two-terminal resistance of the drive layer is measured across $\nu_{tot} = 0$ with two different boundary conditions of the drag layer. The green trace is similar to the setup in Fig. 4.3, and shows a resistance peak at $\nu_{tot} = 0$ when the drag layer is open-circuit. However, this peak vanishes when current is allowed to flow freely on the drag layer by closing the

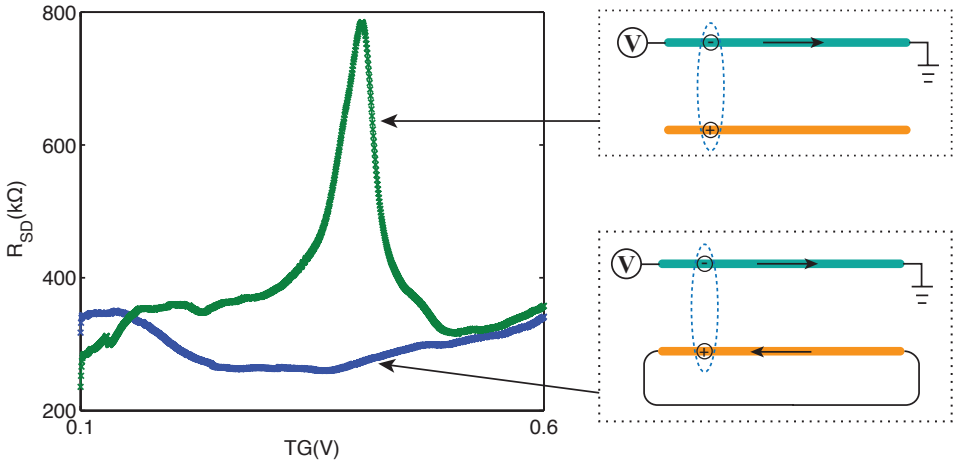

Figure 4.4: Two termional source-drain resistance of the drive layer R_{SD} across $\nu_{tot} = 0$. The schematic inset illustrate the measuremental configuration. The green trace is voltage drag setup with drag layer in open-circuit setup, while the blue trace shows R_{SD} when drag layer circuit is closed.

circuit(blue trace). This current is carried by the excitons, which support currents in the opposite directions in the two layers. The insulator to metal transiton of the drive layer, caused by change of the drag layer boundary condition, really demonstrates the interlayer correlated nature of the $\nu_{tot} = 0$ insulating state.

4.2 Perfect current drag

We can also measure the induced current on the drag layer in this closed-circuit setup. Applying bias voltages on the drive layer, currents measured on both layers are shown in Fig. 4.5. The drive and drag layer currents are almost identical until reaching the high bias regime. The perfect current drag (i.e. $I_{drag} = I_{drive}$) has been shown before in Corbino double quantum well samples at $\nu_{tot} = 1$ [48]. In the previous $\nu_{tot} = 1$ experiments, because it is a correlated quantum Hall state, Corbino

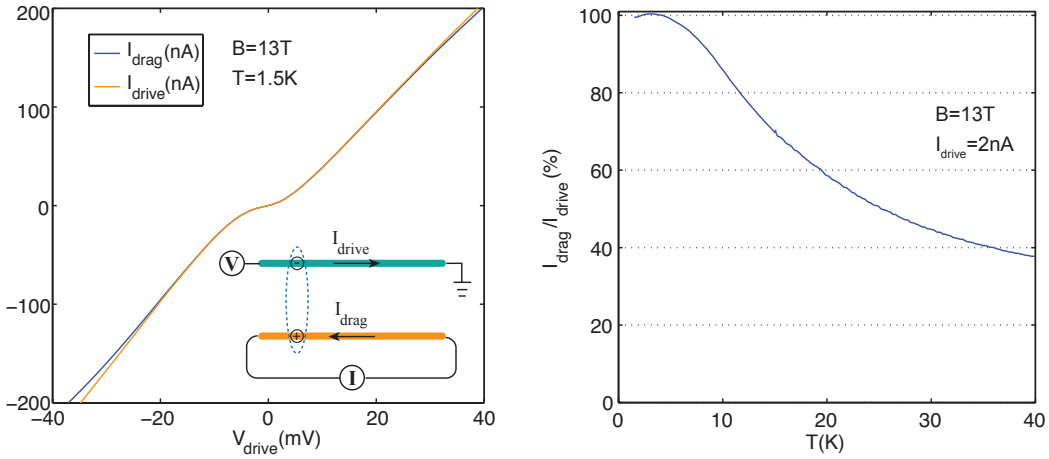

Figure 4.5: Left, current in the drive and drag layer as a function of source-drain voltage applied on the drive layer. The current in drive and drag layers (orange and blue curve) are almost identical in the low bias regime. Right, ratio between drag layer current and drive layer current as a function of temperature.

geometry is needed for eliminating edge transport. And the drag current starts to deviate from the drive current at very small bias current around 0.5nA. In contrast, for $\nu_{tot} = 0$, the drag current we measure maintains above 95% of the drive current with bias currents as high as 200nA. The perfect current drag is also robust against thermal excitation. Ratio between the drag and the drive current I_{drag}/I_{drive} remains $\approx$ 90% at 10K. This robustness against temperature and bias current can facilitate specific device applications, such as 1:1 ground-isolating transformers. Usually transformers require large coils and ferromagnetic materials, thus hard to miniaturize. Our devices, on the other hand, can be microns in size and functions under B=3T and T=4K. It also suggests similar state can be formed between two flatband materials, such as twisted bilayer graphene, without the application of a magnetic field.

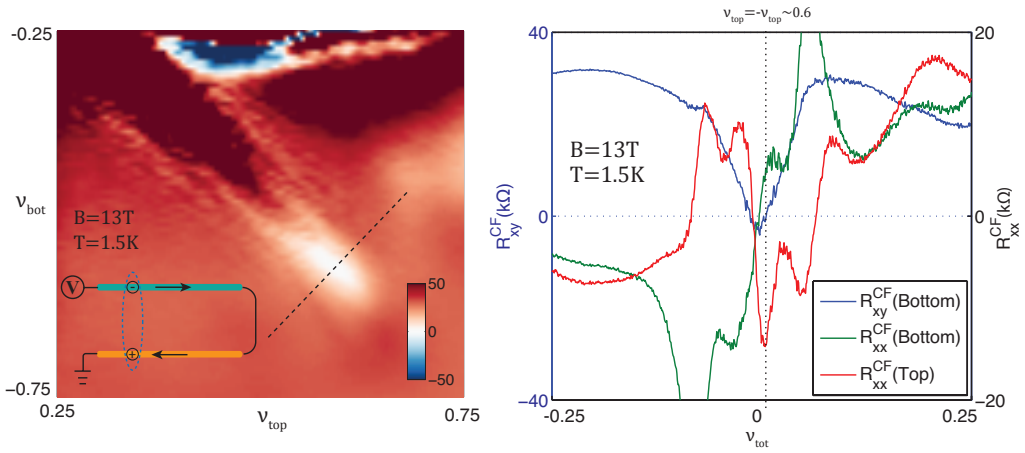

Figure 4.6: Left, counterflow Hall resistance measured on the bottom layer. It vanishes around the $\nu_{tot} = 0$ state (white color). Dashed line marks where the linecut of right panel is taken. Inset, illustration of current flow in counterflow measurement. Right, linecut of counterflow resistance in the Hall direction on the bottom layer and in the longitudinal direction on both layers.

4.3 Counterflow

Counterflow measurements have been utilized in the study of $\nu_{tot} = 1$ state to show the superfluid nature of the exciton flow. In counterflow measurements of $\nu_{tot} = 0$(Fig. 4.6), current is driven on both of the layers. The direction of electrical current is opposite in the two layers, so that they can be carrier by excitons with opposite charges $\pm e$. Voltage drops in both longitudinal and transverse direction in a either top or bottom layer are measured. The counterflow measurement is more difficult in $\nu_{tot} = 0$ than $\nu_{tot} = 1$ state, due to the absent of edge states. In $\nu_{tot} = 1$, if the current injection points on the two layers are at different positions, current in between injection points can still propagate on the edge. As voltage is only probed in the channel, current path difference outside the channel will not affect the counterflow measurement. However, for $\nu_{tot} = 0$, we need to

make sure the current path of both layers completely overlap. Otherwise, where two current paths do not overlop, current is only flowing in one of the layers and will be stopped by the exciton insulator phase. To avoid this problem, the leads used for current injection on both graphene layers completely overlap until they reach the heavily doped parts of the leads, where the exciton insulator phase no longer exists (corner leads in Fig. 4.2). Similar consideration was also taken for the perfect current drag measurements.

The measured counterflow Hall resistance on the bottom layer is shown in Fig. 4.6. In most part of the plot, the counterflow Hall resistance R_{xy}^{CF} mainly depend on the bottom layer filling factor and $R_{xy}^{CF} > 25.8k\Omega$. However, at the $\nu_{tot} = 0$, the counterflow Hall resistance vanishes (white colored area in Fig. 4.6 left). The zero Hall voltage is due to that current is only carried by excitons, which is charge neutral and experience no Lorentz force. A linecut across $\nu_{tot} = 0$ state (dashed line in Fig. 4.6 left) also reveals vanishing Hall resistance at $\nu_{tot} = 0$. However, the behavior of longitudinal counterflow resistance is intriguing, as it appears to change sign across $\nu_{tot} = 0$. At $\nu_{tot} = 0$, the longitudinal counterflow resistance is close to zero. The reason of the sign change is still unclear.

4.4 Phase diagram

It is interesting to see how the insulating behavior goes away as temperature and bias voltage increase. It is unclear whether it should be a sharp transiton from exciton insulator to an uncorrelated metal, or it will display an activation behavior as seen in other insulators. In Fig. 4.7, it appears that

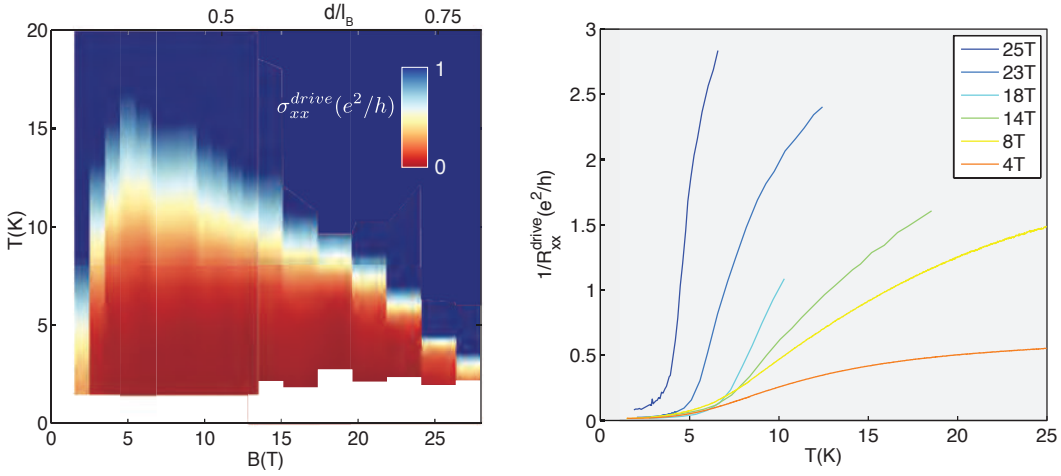

Figure 4.7: Left, conductance of the drive layer as a function of magnetic field and temperature in the small bias limit with Coulomb drag setup. Right, same information as left panel, but plotting the conductance as a function of temperature at a few magnetic field values.

in the low magnetic fields, the transition is rather smooth and resembles that of thermal activations, while in the high field regime, the transiton is sharp. At the same time, the overall temperature scale first increases with magnetic field and then decreases in the high field limit. This behavior might be linked to a phenomenon called BEC-BCS crossover. In the next chapter we are going to take a closer look at the superfluid phase transiton of $\nu_{tot} = 1$ state to decipher the effect of magnetic field on the exciton condensate phase transiton. In Fig. 4.8, we can see that the exciton insulating state persists to rather high bias voltages.

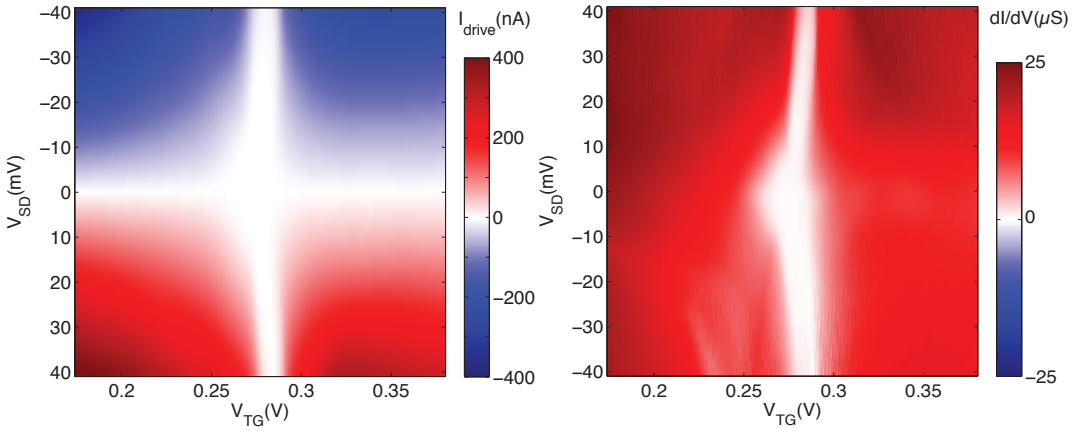

Figure 4.8: Left, drive layer current as a function of source-drain bias and gate voltages across $\nu_{tot} = 0$ state at B=13T and T=1.5K in the Coulomb drag setup. Right, dI/dV plot of the data on the left panel.

5

BEC-BCS crossover

Due to Pauli exclusion principle, fermions by themselves can not form a condensate. In fermionic systems, superconductivity and superfluidity are enabled through pairing of fermionic particles into bosons, and the condensation of these fermion pairs. When the attractive interaction is strong, tightly bound fermion pairs behave like diatomic molecules, forming Bose-Einstein condensate (BEC) at low temperatures. Oppositely, at zero coupling, both layers stay as uncorrelated Fermi liq-

uids. When a arbitrarily weak coupling is introduced, it establishes BCS condensate of cooper pairs, which are dynamically coupled in the momentum space. In this chapter, we discuss the crossover between a BEC-like condensation and a BCS-like condensation of interlayer excitons[23,38], through continuously tuning the coupling strength by changing the effective interlayer separation d/l_B. When the coupling is strong ($d/l_B \ll 1$), the BEC nature of the condensate is evident from the activated phase above condensation temperature, where electrons and holes are paired but not condensed. This phase is manifested by gradually increasing resistance with increasing temperature, which is governed by thermal activation. As effective layer separation d/l_B increase, the interlayer coupling weakens, and the gradual resistance increase turns into a sharp superfluid transition. This sharp transition indicates excitons form and condensate simultaneously as predicted by BCS theory. Berezinskii-Kosterlitz-Thouless (BKT) transition is identified in the BCS regime and we found the critical temperature decreases as the interlayer coupling weakens.

5.1 Introduction to BEC-BCS crossover and BKT transition

There are two prominent types of fermionic condensates: BEC and BCS. The nature of a fermionic condensate is governed by the competition between coupling strength and particle density[59,60]. When the coupling is strong and density is low, the size of the bound states is much smaller than inter-particle separation. Thus the fermion pairs are dilute and can be treated as composite boson particles, which forms a BEC type of condensate under suitable conditions. As the density increases, fermion pairs start to overlap with each other once the inter-pair distance is comparable with the

size of the bound state itself. Real space fermion pairs break apart when the overlap between different pairs are significant. In this high density regime, the coupling strength is small comparing with Fermi energy, due to the screening effect. Therefore Fermi liquid behavior is restored. However, at low enough temperatures, the weak attraction between Fermi surfaces induce Fermi surface instablity. This Fermi surface instability causes a small fraction of fermions near Fermi surface to form cooper pairs and establish a BCS condensate. The cooper pair in a exciton system compose of an electron and a hole, instead of two electrons in a superconductor. A prominent signature of BCS condensates is that cooper pairs form and condensate simultaneously at the same temperature. Above this critical temperature, not only there is no superfluidity, the cooper pairs themselves also do not exist. In this high temperature regime of the BCS limit, the system recovers Fermi liquid behaviors. The crossover between BEC and BCS is an idea highly relevant to many branches of physics, including cold atom physics[61,62,63,64,65], nuclear physics[66], particle physics[67] and especially condensed matter physics[68,69,70,71,72,73]. Yet it has only been convincingly shown in cold fermion gases at $\sim$nK temperatures[61,62,63,64,65]. Despite many types of superfluidity being the core of condensed matter physics, direct manifest of BEC-BCS crossover in a condensed matter system have not been observed. Conventional superconductors are in the BCS limit with extremely weak coupling. In contrast, the coupling in high Tc superconductors is much stronger. Thus it should be situated towards the BEC limit and pairs may form before condensation. This BEC-like condensation is a proposed scenario for the pseudo-gap phase above superconducting transition temperatures in under-doped high-Tc samples[71,72,73]. In the pseudo-gap phase, although the materials do not superconductor, it shows a soft gap around the Fermi energy, which could be due to the pre-formation of cooper pairs.

However, this interpretation is still under debate. Mapping out the phase diagram continuously across BEC and BCS limits may help us achieve better understanding of other superfluid systems as well.

In order to realize BEC-BCS crossover, we need to be able to tune the coupling strength by changing the interaction strength or particle density. This is very difficult in traditional 3D superconductors or superfluids, but is relatively easy in a 2D system. One candidate of realizing the BEC-BCS crossover is the interlayer exciton condensation[38,23]. The uniqueness of interlayer exciton condensation is that it is a highly tunable system. In a double-layer system, both particle density and interlayer interaction strength can be controlled by gates and interlayer seperation, respectively. By tuning the exciton density, both BEC and BCS regime can be accessed[38,74,75,76]. When the interlayer exciton distance ($\sim\ n^{-1/2}$, where n is the exciton density) is much larger than Bohr radius of an individual exciton, excitons are spatially paired (Fig. 5.1) and institute an exciton gas phase above the condensation temperature. Here, the interlayer correlation persists above the superfluid transition temperature and only slowly declines as thermal activation breaks up excitons. In the opposite high density limit, pairing between a small fraction of electrons and holes occurs in the momentum space (Fig. 5.1) below a critical temperature, and vanishes above. As particle density increases, the condensation temperature goes up in the BEC limit due to higher degeneracy ($T_C\ \propto\ n$), and drops down in the BCS limit due to diminishing interlayer coupling. Therefore the highest superfluid transition temperature is usually expected in the crossover regime[38,60].

For the case of exciton condensation under magnetic field, the detailed description is different, while the spirit of BEC-BCS crossover carries over. Under magnetic fields, it is hard to define the ex-

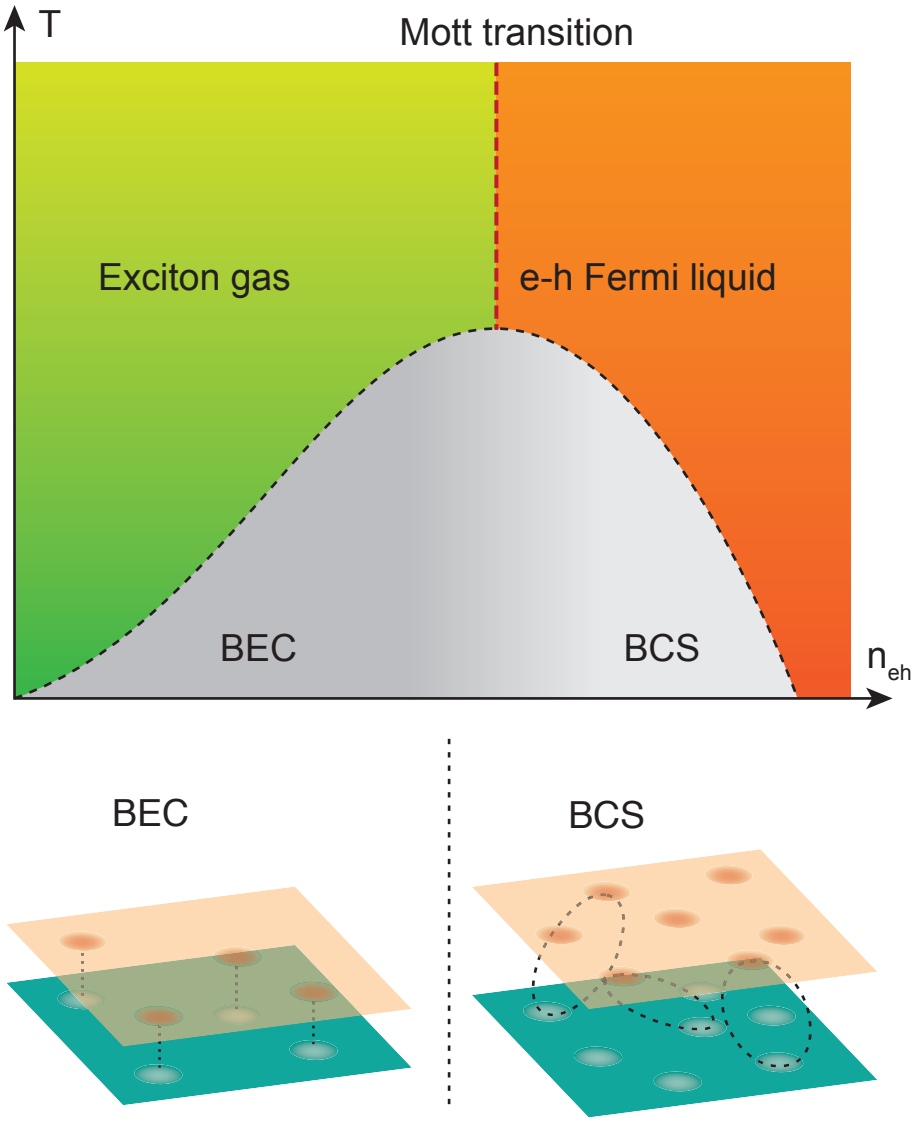

Figure 5.1: Top, illustration of interlayer exciton phase diagram. n_{eh} is the density of electron-hole pairs. Bottom, electron-hole pairing in the BEC and te BCS regime. In BEC, all electrons and holes form real space pairs, while in the BCS regime, a small fraction of electrons and holes pair up in momentum space.

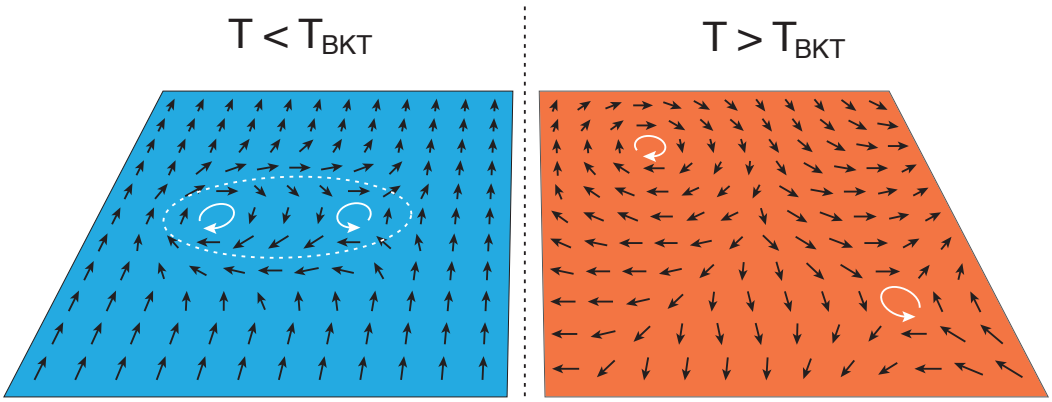

Figure 5.2: Illustration of BKT transiton. The arrows represent order parameter of XY model, which can be spin direction or superfluid phase. When $T > T_{BKT}$, vortex and anti-vortex (white circles with arrow) are free to move, while they are bound into pairs (white dashed line) below BKT temperature.

citon Bohr radius. So the parameter controlling coupling strength is d/l_B, which sets ratio between interlayer Coulomb interaction and innerlayer Coulomb interaction[23]. When d/l_B is small, the two layers are strongly coupled to form a BEC. As d/l_B increases, the interlayer interaction weakens by screening and the condensate crossover to a BCS type. Although $\nu_{tot} = 1$ superfluid state has been observed, it has only be stabilized in very small d/l_B window,[23,77,78,50,79,80,16]. In this chapter, using graphene double-layer devices with dual graphite gates[20], we are able to realize exciton condensation over a large range of magnetic fields (from 4T to 36T) and corresponding d/l_B ratios (from 0.3 to 0.77).

Another relevant phenomena associated with exciton condensate phase transition is the BKT transition. In 3D, phase transitions occur when the order parameter drops to zero at the mean field transition temperature. However, in a 2D XY model, below the mean field transition temperature when the order parameter is still finite, the system can have topological excitations where the the

order parameter, such as pseudo-spin directions or supefluid phases wind around a point to form a vortex (Fig. 5.2). The phase winding can be multiples of 2π (vortex) or -2π (anti-vortex). Because the energy of creating a vortex is $\pi\rho_S ln(R/a)$ (ρ_S is phase stiffness, characterizing energy cost of phase gradients, a is the size of the vortex core, R is the size of the sample), stand alone vortexes can not be find at zero temperature in a very large sample, as the energy cost diverges with the sample size. However, as the temperature increase, the system gains free energy from entropy which is $-2k_B T ln(R/a)$. This entropy comes from the large number of possible locations for the vortexes. So we can define a new phase transition temperature called BKT transition temperature $T_{BKT} = \pi\rho_S/2k_B$, where the total free energy for a vortex is zero. Below BKT temperature in a infinite large sample, stand alone vortex can not exist due to the diverging energy cost. Yet, vortex and anti-vortex pairs can emerge, which cost finite energy to create and cause the long range correlation function to decay with a power law. On the other hand, above the BKT transition temperature, vortexes and anti-vortexes will proliferate, totally destroying any long-range correlation and bring the system back to normal phases.

5.2 BEC-BCS crossover of $\nu_{tot} = -1$

As mentioned in Chapter 3, $\nu_{tot} = 1$ is a counterflow superfluid. By measuring how this counterflow resistace change with temperature, we can understand the superfluid phase transition. Here we focus our study on the $\nu_{tot} = -1$ state in monolayer graphene double-layers. In monolayer graphene double-layers, $\nu_{tot} = 1$ and $\nu_{tot} = -1$ are practically the same due to electron-hole

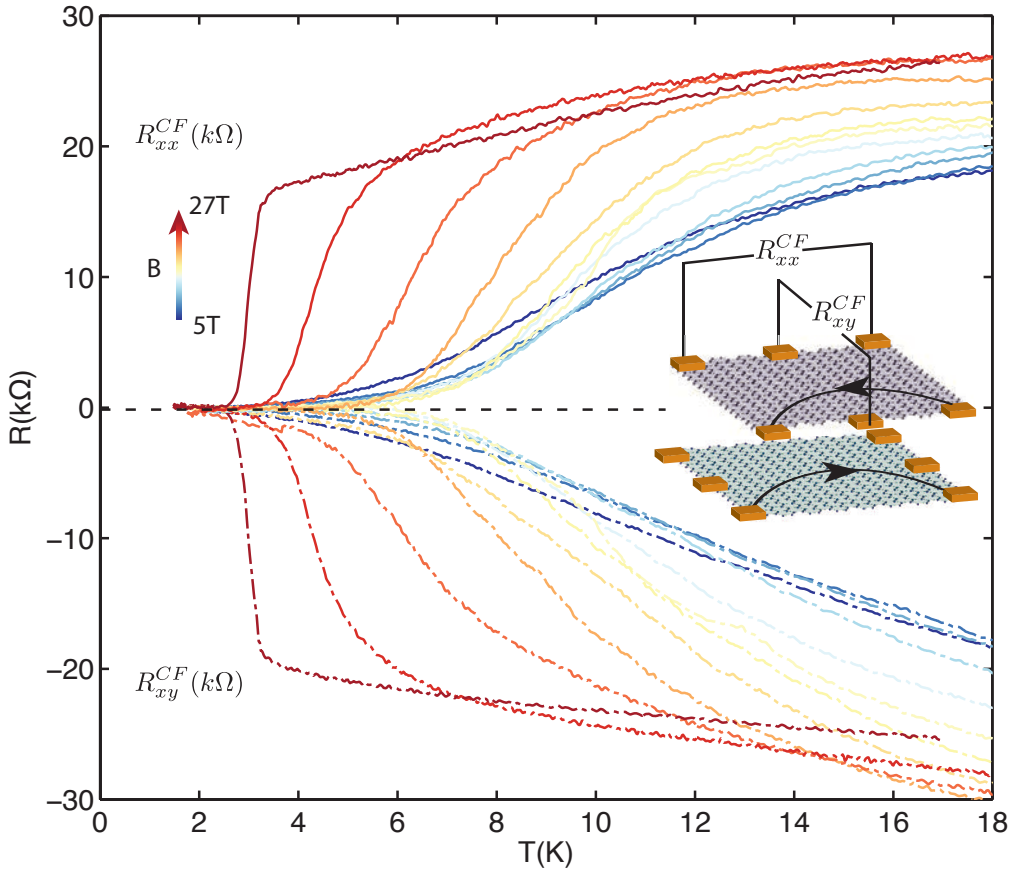

Figure 5.3: Counterflow resistance of $\nu_{tot} = -1$ under different magnetic fields in both longitudinal and transverse directions. Inset, schematic for the counterflow measurement setup. The golden blocks denote electrical contacts and the arrows indicate current flow in each layer.

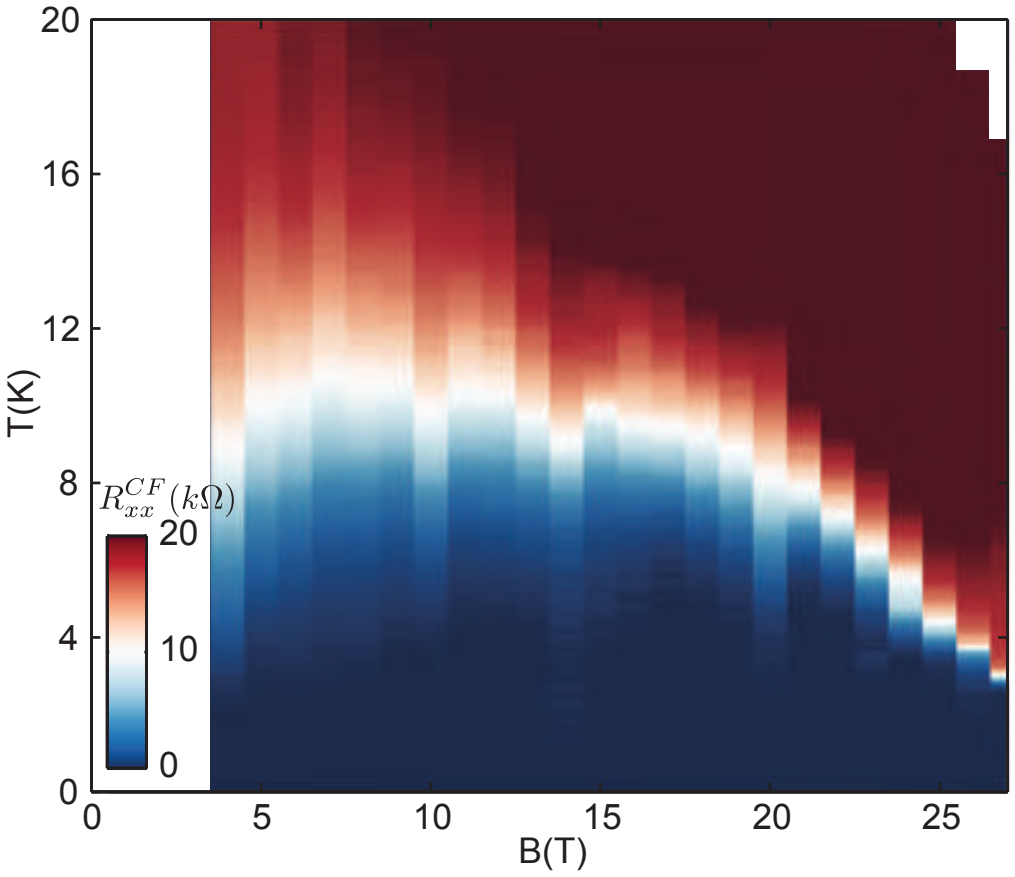

Figure 5.4: Map of longitudinal counterflow resistance as a function of magnetic field and temperature. The low resistance region forms a dome shape which peaks around 15T.

symmetry, the choice of $\nu_{tot} = -1$ is simply due to a better contact perfermance on the hole side. We utilize counterflow measurement to direct probe dissipation of exciton transport(with co-propagating electrons and holes generating opposite currents in the two layers). Current is driven on the two layers in the opposite directions and voltage drops in one of the layers are measured (Fig. 5.3 inset). The base temperature resistance vanishes for all magnetic fields between 4-27T, indicating exciton condensation at the lowest experimental temperatures[23,50,78]. However, the finite temperature behaviors are drastically different for different magnetic field regimes. Under low magnetic fields, as temperature increase, resistance rises gradually (Fig. 5.3). In contrast, under high magnetic fields, there is a sharp jump in resistance, similar to a superconducting transition. This can also be seen in the 2D map of counterflow resistance (Fig. 5.4), where the transition with temperature becomes increasingly sharper at higher magnetic fields. We also note that the low resistance area (blue color area in Fig. 5.4) shapes like a dome, indicating the transition temperature first increase and then decrease with magnetic field. This behavior appears very similar to the illustration of Fig. 5.1. Another interesting observation is that the longitudinal counterflow resistance behaves very similar to the counterflow Hall resistacne (Fig. 5.3).

We found these observations agree well with the generic BEC-BCS crossover description of excitons. At low magnetic fields, the gradual resistance increase can be attributed to the persistence of exciton pairing above the superfluid transition temperature[38,60]. Even not condensated, excitons as charge neutral particles, do not experience Lorentz force and are less prone to be scattered by charged impurities. The absence of Lorentz force naturally lead to zero Hall resistance without requiring condensation of excitons. The longitudinal resistance of excitons can also be signifi-

cantly lower than that of free electrons. Most of the longitudinal resistance in strong magnetic fields is caused by cyclotron motion (resistance under zero magnetic field at the same density is much smaller). As charge neutral excitons move straight across the sample without cyclotron motion, it thus encounter much less scattering. This lead to little resistance in both directions just above the condensation temperature. As temperature rises, the thermal activation creates charged excitations that are subjected to cyclotron motions, generating notable resistance. On possibility of the such charged excitations are free electrons and holes created by unbinding excitons. Then the resistance is proportional to number of free electrons and holes, which can be fitted with the activation behavior (Fig. 5.5). Only at very high temperatures, all the excitons broke apart and recovers the composite fermion Fermi liquid behavior. The same argument can be used for any types of charged excitation in an exciton system, not necessarily limited to exciton unbinding. On the contrary, in the BCS regime (high magnetic fields), the pairing only exists when the excitons are condensed. The system transit directly from a superfluid to a composite fermion Fermi liquid without going through a intermediate exciton gas phase, causing the resistance jump. If we assume the crossover correspond to the highest transition temperature, it rough occurs around $B = 12 - 17\mathrm{T}$ at the top of the dome in Fig. 5.4, coincide with where the transition become sharper as well. We also emphasize that these two behaviors smoothly connect together, which is in accordance with a crossover, rather than a quantum phase transition.

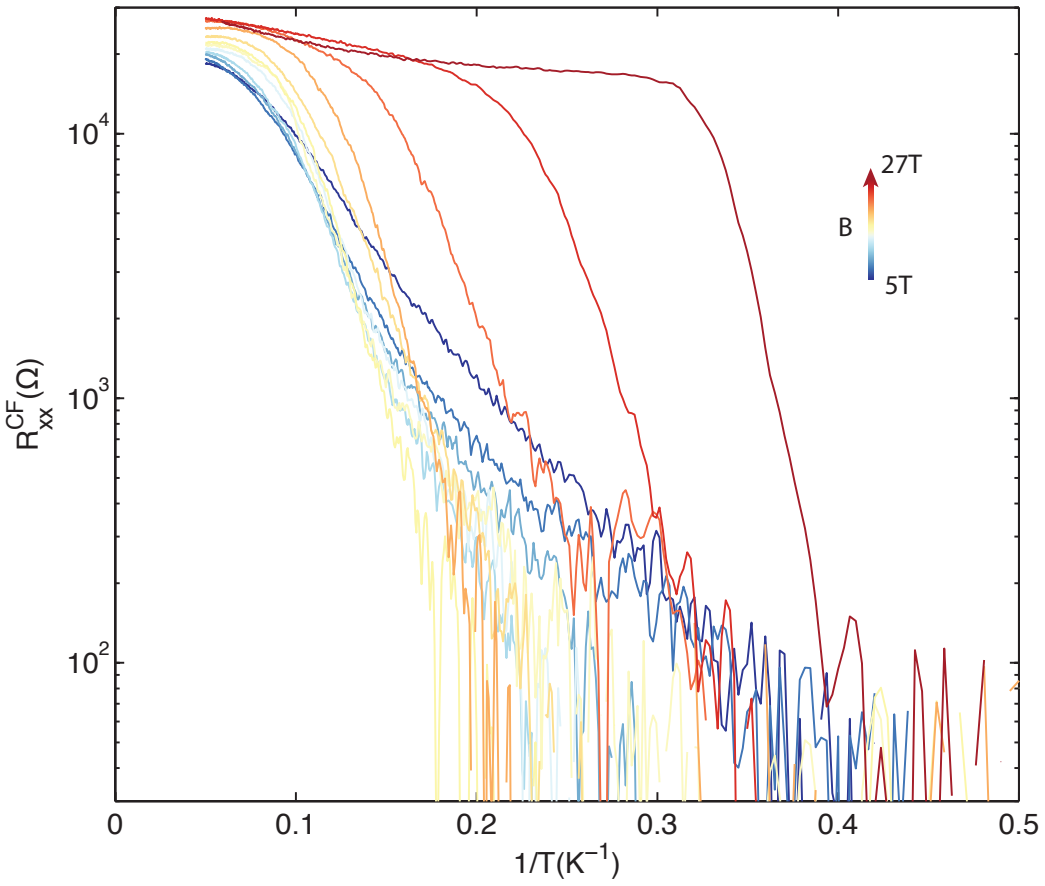

Figure 5.5: Longitudinal counterflow resistance in log scale as a function of 1/T between 5T (blue trace) and 27T (red trace). This Arrhenius plot show well defined activation behaviors under low magnetic fields (straight line) but large deviation from activation behavior at high magnetic fields.

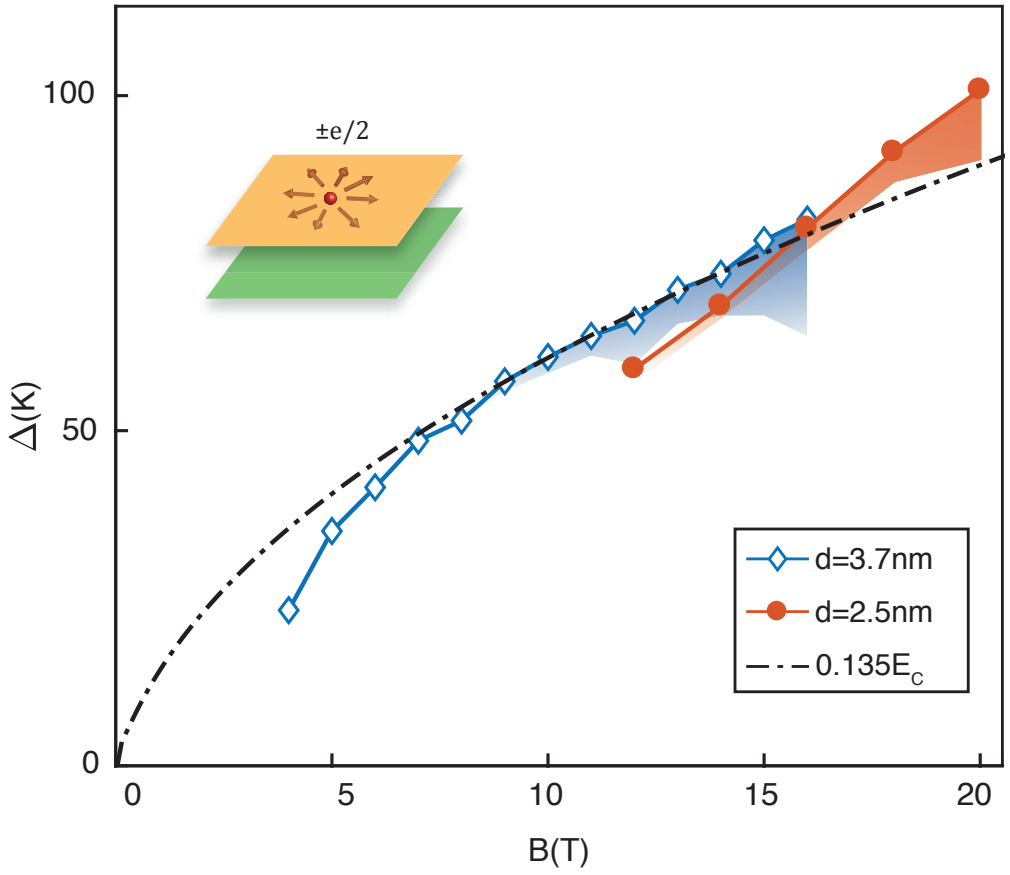

Figure 5.6: Activation gap as a function of magnetic fields for two devices with different interlayer separation d = 3.7nm and d = 2.5nm. The shaded areas marks uncertainty of the gap due to deviation from the activation behavior. At high fields, distinct different slopes can be identified in Arrhenius plot in different temperature ranges, making activation gap ill-defined. The dashed black line denote the scaling of Coulomb energy according to l_B. This line fits the activation gap well when the gaps are well-defined in both samples with different interlayer separation. Inset represents a isolated meron with $\pm$e/2 electron charge and half vortecity.

5.3 Quantitative analysis of activation gap in BEC regime

Although the general behavior is explained above, quantitative analysis of these behaviors require further consideration tailored for two-dimensional exciton condensation under magnetic fields. For the $\nu_{tot} = -1$ state, instead of exciton unbinding, creating full charge $\pm e$ excitations, the lowest energy excitations are merons and anti-merons[81]. The merons are very similar to the vortexes in BKT transition introduced earlier. It also carries a phase winding of $\pm 2\pi$. However, unlike vortexes, meron is a charged excitation, which is half of an electron charge combined with a 2π vortex of the superfluid phase (Fig. 5.6 inset)[23,81].

The merons and anti-merons are binded into pairs below BKT transition temperature T_{BKT}, where zero resistance is preserved. Above T_{BKT}, merons and anti-merons unbind. Despite being a different type of excitation from exciton unbinding, merons are charged excitations just like free electrons and holes. Thus when merons and antimerons are generated, the system is not longer a pure bosonic exciton system. When counterflow current is introduced, the current exerts Magnus force on the merons and anti-merons, causing them to move. Then, the movement of merons and anti-merons will create dissipation and resistance. This resistance is thus proportional to the number of free merons, which is thermally activated.

The activation energy of resistance thus correspond to energy cost of merons. In Fig. 5.6, we plotted activation energy obtained from Fig. 5.5. In the low field regime, we found the activation gap scales with the Coulomb energy E_C regardless of the interlayer separation. This is expected in the $d/l_B \ll 1$ limit. When $d/l_B = 0$, the density of thermal activated merons will be $\sim$

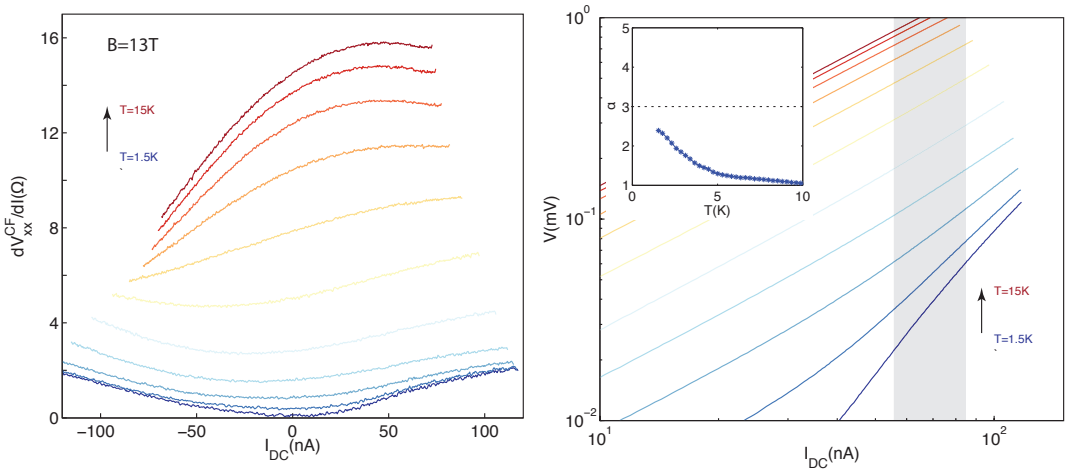

Figure 5.7: Left, differential counterflow resistance as a function of bias current. Right, IV curve in log-log plot. The inset shows the power law α extracted from IV curve in the shaded area.

$l_B^{-2} exp^{-4\pi\rho_S/T}$, in which $\rho_S \propto E_C$ is the phase stiffness. From this equation, we can see the activation gap $\Delta \propto E_C \propto l_B^{-1}$ only depend on magnetic field in the $d/l_B \ll 1$ limit.

As magnetic field increases, activation gap become ill-defined, as the Arrhenius plot exhibits different slopes in different temperature ranges. At high magnetic field, a sharp phase transition better describes the temperature dependence. On the contrary, we note that in the low field BEC limit, superfluid transition temperature is hard to identify, as the resistance smoothly increase in an activating behavior. When we perform the IV curve measurements (Fig. 5.7), the differential counterflow resistance depends on the counterflow current in a near quadratic manner. We can not clearly see a critical current. And the power law extracted from IV curve ($V \propto I^{\alpha}$) never exceed three, even at the lowest temperature of our experiment (300mK).

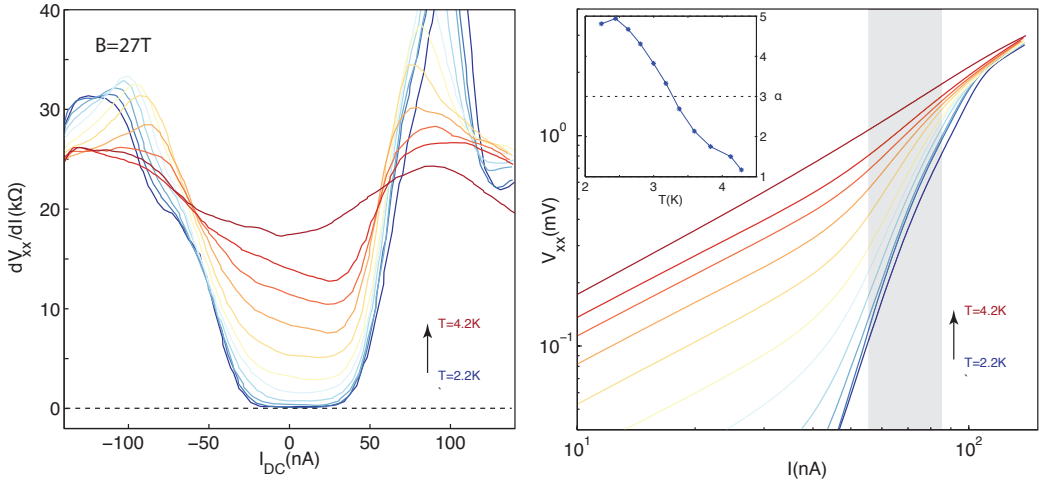

Figure 5.8: Similar to Fig. 5.7, but taken at B=27T. Critical current can be identified when the counterflow resistance start to rise. The power α crosses three.

5.4 BKT transition in the BCS regime

As prior mentioned, superfluid transition in two dimensions is described by the BKT transition[82]. However, different from the BEC case where the BKT temperature is set by superfluid phase stiffness[82], in the BCS limit the meanfield transition temperature T_{BCS} can be much lower than T_{BKT} found by the phase stiffness. The phase stiffness describes the hardness of changing the phase of condensated excitons over space. It originates from inter-exciton interaction, which can be very strong in the high density regime. On the contrary, exciton binding can be very weak. Even below T_{BKT} determined by phase stiffness, excitons might already disintegrate due to their low pairing energy. So BKT transition temperature of a BCS condensate is bound by the BCS mean field transition temperature $T_{BKT} \approx T_{BCS}$ above which the phase stiffness vanishes[83]. In this regime, vortexes and anti-vortexes with superfluid phase winding of 2π or 4π (2π and 4π vortex) are the excitations of

the system[74].

Above T_{BKT}, the system is full of free vortexes and anti-vortexes. When a current is driven through the system, vortexes move under the Magnus force and create dissipations if not pinned. As a result, Ohmic behavior will manifest. Below T_{BKT}, vortexes and anti-vortexes are paired and produce no resistance under small bias (Fig. 5.8). This is due to the fact that the vortex and the anti-vortex experience Magnus force in the opposte directions, which cancels out. Thus the vortex-anti-vortex pairs are not prompt to move and do not generate dissipation. However, under finite bias currents, the vortex-anti-vortex pairs can be ripped apart by the opposite direction Magnus force. This creates free roaming vortexes and lead to dissipation that depend on the current amplitude. This effect translates to a non-linear current-voltage (I-V) relationship $V \propto I^{\alpha}$ (exponent $\alpha = 2T/T_{BKT} + 1$) in the small current limit below BKT temperature. Across the BKT transition temperature, α jumps from three to one. Although theoretically, the power should suddenly change from three to one, most experiments reports a continuous changing α with temperature due to disorders in the sample. In Fig. 5.8, we show the IV curves of counterflow transports, from which power law α is extracted (Fig. 5.9). By common convention, we used $\alpha = 3$ to define the critical temperature T_{BKT}. T_{BKT} obtained this way is shown in Fig. 5.10, which decreases with increasing d/l_B as interlayer interaction weakens. Eventually, at magnetic fields above 30T for d=3.7nm, the $\nu_{tot} = -1$ state is completely gone, and two layers resume independent quantum Hall behaviors. After scaling with the Coulomb energy, we found that T_{BKT} of two samples with different interlayer separations fall onto a universal curve (Fig. 5.11). The origin of this universal behavior is not yet understood.

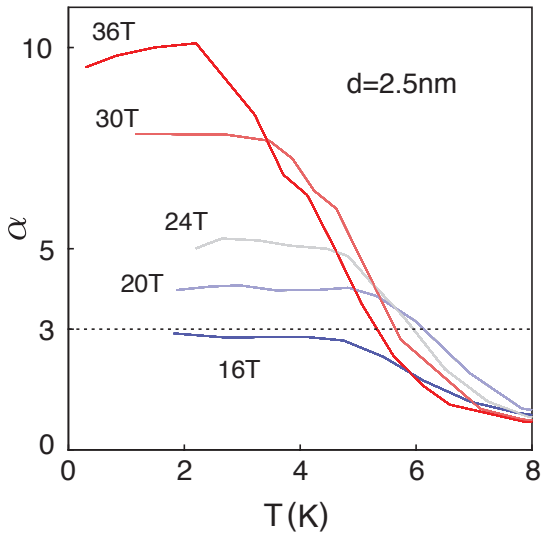

Figure 5.9: α extracted from the IV curve as a function of temperature. Under high magnetic fields, α rise above three at low temperatures as expected from BKT transtion. However, as magnetic field drops, α saturates at lower values and eventually T_{BKT} can not be define when α saturates below three (for example: B = 16T).

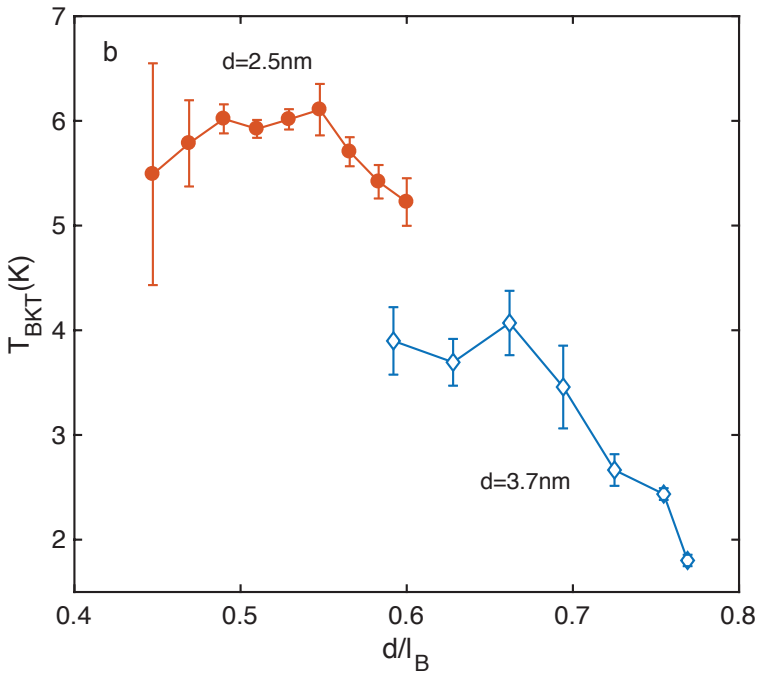

Figure 5.10: BKT transition temperatures defined at power $\alpha = 3$ as a function of d/l_B in two samples with different interlayer separations.

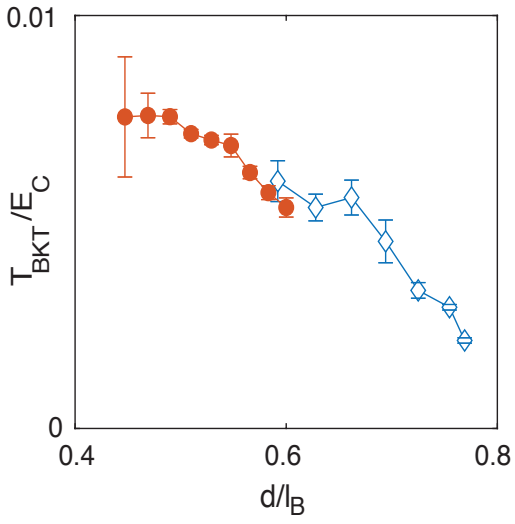

Figure 5.11: BKT transition temperatures after scaling to Coulomb energy E_C. Data from samples with different interlayer separation fall onto a universal line.

6

Fractional interlayer quantum Hall states

In two-dimensional (2D) electron systems under strong magnetic fields, interactions can cause a variety of peculiar effects, known collectively as the fractional quantum Hall (FQH) effects[84,85]. Bringing two 2D conductors to proximity, a new set of correlated states can emerge due to interactions between electrons in the same and opposite layers[45,86,23,87]. Previously we have talked about the exciton condensation, which can also be seen as an integer interlayer quantum Hall effect. Here

I demonstrate interlayer correlated FQH states in a monolayer graphene double-layer. Current flow in one layer generates different quantized Hall signals in the two layers. This result is interpreted by composite fermion (CF) theory with one interlayer magnetic flux quantum and two intralayer flux quanta attachments. We observe FQH states corresponding to integer values of CF Landau level (LL) filling in both layers, as well as "semi-quantized" states, where a full CF LL couples to a continuously varying partially filled CF LL. Remarkably, we also recognize a quantized state between two coupled half-filled CF LLs, attributable to pairing between layers to form a CF exciton condensate.

6.1 Fractional quantum Hall effect and composite fermions

The energy levels of a non-interacting 2D electron system in a magnetic field are quantized into a discrete set of LLs with degeneracy proportional to the area of the system[87]. A key parameter in these systems is the LL filling factor ν. Integer quantized Hall (IQH) effects occur when ν is an integer, where the Fermi level is in an energy gap between two LLs, and Coulomb interactions between electrons can often be ignored. However, for fractional ν, Coulomb interactions, which lift the LL degeneracy, have a dominant effect, and new collective states of matter can appear at fractional values of ν, leading to the fractional quantized Hall (FQH) effect[84].

In single-layer systems, the most commonly observed FQH states can be understood in terms of the composite fermion (CF) picture[88]. Here, the electrons are each bound to even number ($2m$) of magnetic flux quanta to form CFs, leaving only relatively weak residual interactions between them (Fig. 6.1). The rational behind this flux attachment is that the wave function $\Phi \propto (z_i - z_j)^{2m+1}$

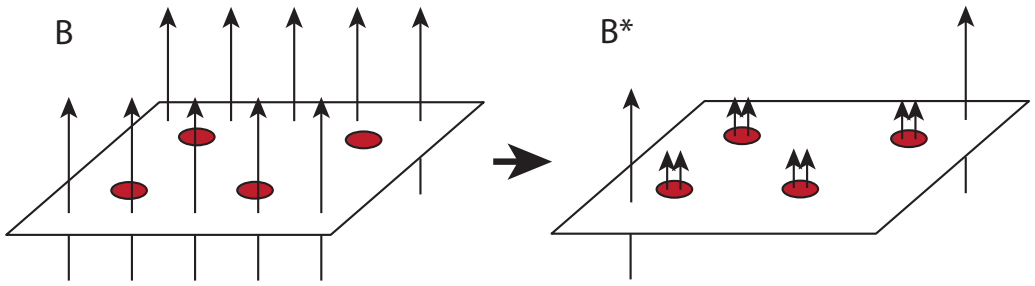

Figure 6.1: Illustration of composite fermions. The arrow represent magnetic field flux. Red circles denotes electrons.

vanish faster when two electrons are close to each other, thus reducing their repulsion energy. Since applied magnetic field is reduced by the binding of magnetic flux, the CFs experience an effective magnetic field $B^* = B - 2mn\phi_0$, which is weaker than the original field B. From this effective magnetic field, we can relate ν to the CF LL filling factor p: $\nu = p/(2mp+1)$. If p is an integer, positive or negative, then the CF system is predicted to have an energy gap, and the electrons will be in a corresponding FQH state, with ν equal to a fraction with odd denominator. Because of this energy gap, the FQH state has vanishing longitudinal electric resistance R_{xx} and quantized Hall resistance[84] $R_{xy} = h/\nu e^2$. FQH states also have quasiparticles with fractional charge and fractional quantum statistics (anyons), different from the statistics of bosons or fermions[85,89].

6.2 Fractional ν_{tot} interlayer correlated states

The scope of quantum Hall physics further expands when we bring two layers close to each other, allowing strong Coulomb coupling between them, while suppressing a direct interlayer tunneling. The exciton condensate state discussed before, can be seen as a interlayer correlated integer quantum

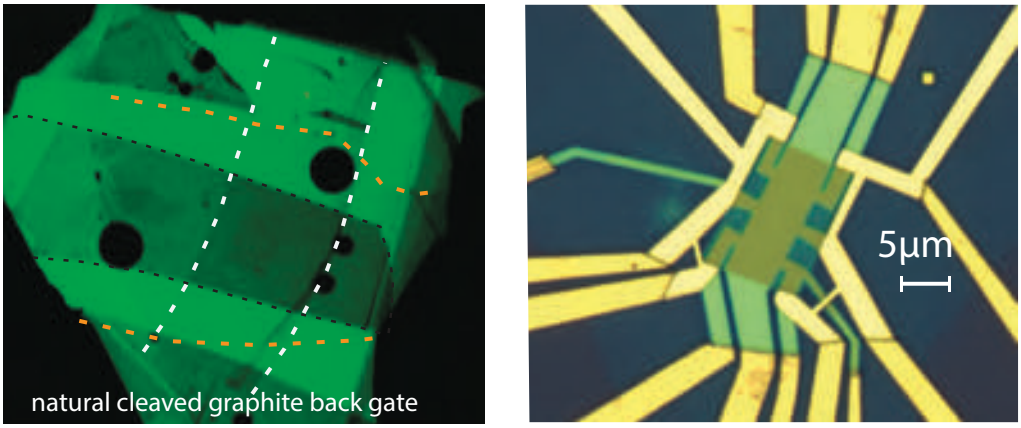

Figure 6.2: Left, image of stack before nano-fabrication. Black dashed line marks the shape of bottom graphite. Orange dahsed lines marks the boundary of top graphene layer. White dashed lines marks the boundary of bottom graphene. Right, final device image.

Hall effect, as the total filling factor is an integer. In the Halperin (111) wave function (Eq. 1.1), we can see electron wave function $\Phi \propto (z_i - w_j)^1$ vanishes when electrons from two layers coincide at the same x, y postion. This can also be seen as electrons in one layer bind with a flux on the opposite layer, causing electron wavefunction on the second layer to vanish on the flux(Fig. 6.4). In GaAs double quantum wells, $\nu_{tot} = 1$ is the only observed interlayer correlated state, while exciton condensation at several other integer ν_{tot} have also been shown in this thesis. Despite theoretical expectations[88,90,91,87,92,93], no direct experimental observation of interlayer correlation at fractional total filling factor has been made thus far. The observed incompressible state at $\nu_{tot} = 1/2$ in double-layer or wide single-layer GaAs has been proposed to be the correlated Halperin (331) state[45], but without direct experimental verification[86,94,95,96]. The delicacy of these expected interlayer FQH states demands extremely high sample quality.

In the present study, we have fabricated monolayer graphene double-layer devices with top and bottom graphite gates. And to ensure best sample quality, we used nature cleaved graphite backgate as oppose to pre-patterned graphite gates utilized in the last two chapters (Fig. 6.2). The thickness of interlayer hBN of this specific device is ≈2.5 nm.

Coulomb drag measurements were first performed with both layers at the same carrier density ($\nu_{top} = \nu_{bot} \equiv \nu_{eq}$) (Fig. 6.3). The previously observed $\nu_{tot} = 1$ exciton condensate state[80,16] can be clearly identified at $\nu_{eq} = 1/2$, with quantized $R_{xy}^{drive} = R_{xy}^{drag} = h/e^2$ and vanishing R_{xx}^{drag}. In this high quality sample, however, additional features with large drag responses are also observed away from $\nu_{tot} = 1$, indicating that strong interlayer coupling persists, thereby enabling additional interlayer correlated states (Fig. 6.3). In particular, we observe vanishing R_{xx}^{drag} at $\nu_{eq} = 1/4, 1/3, 2/5, 3/7, 2/3$, which suggests that incompressible states are developed at these filling factors. Among them, $\nu_{eq} = 1/3$ and $2/3$ appear as trivial single layer quantum Hall states, evident from vanishing R_{xy}^{drag}. We focus our attention first on $\nu_{eq} = 2/5$ and $3/7$ particularly, which are two most prominent states that produce quantized Hall responses in the drive and drag layer. Interestingly, for these states, the two Hall resistance, R_{xy}^{drag} and R_{xy}^{drive}, are quantized to different fractional values. For $\nu_{eq} = 2/5$, we observe $R_{xy}^{drag} = 1$ and $R_{xy}^{drive} = 3/2$ while for $\nu_{eq} = 3/7$, $R_{xy}^{drag} = 2/3$ and $R_{xy}^{drive} = 5/3$, respectively (from now on we use the unit of resistance quantum h/e^2 for the quantized resistance values). From these numbers, we note that the sum of Hall resistance in the drive and drag layer $R_{xy}^{drive} + R_{xy}^{drag} = 1/\nu_{eq}$, as if a portion of Hall voltage is shifted from the drive layer to the drag layer.

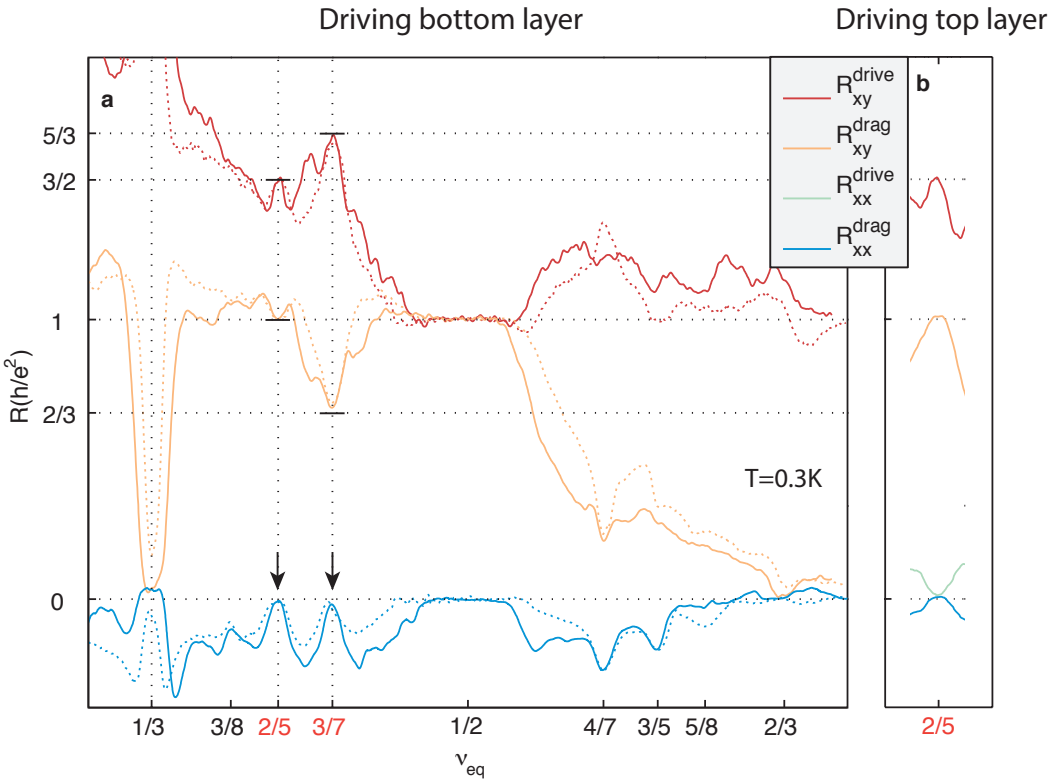

Figure 6.3: Interlayer correlated states at fractional filling factors in graphene double-layer with equal densities. a, vanishing longitudinal resistance (R_{xx}^{drive}, R_{xx}^{drag}) and quantized Hall resistance (R_{xy}^{drive}, R_{xy}^{drag}) in the drive and drag layer appear at $\nu_{eq} = \nu_{top} = \nu_{bot} = 2/5$ and $3/7$. The solid curves are taken under $B = 31$ T and dotted curves are from $B = 25$ T. Short horizontal lines mark the Hall resistance quantization values. b, same measurement as a at 25 T, but with drive and drag layer switched.

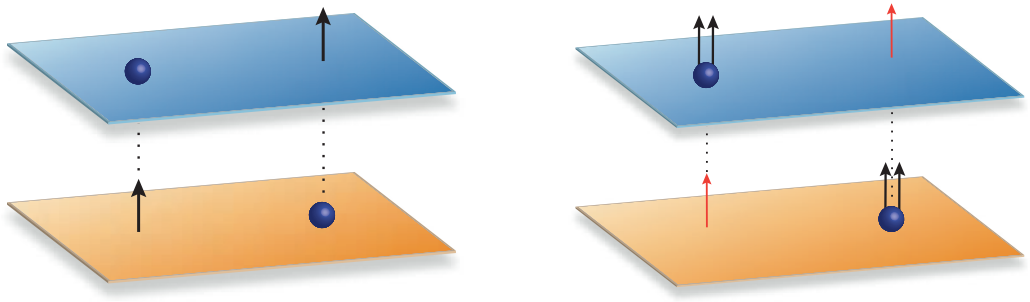

Figure 6.4: Left, composite fermion picture of $\nu_{tot} = 1$ exciton condensate state. Each electron bind with one flux quantum in the opposite layer. Right, compostie fermion picture for observed fractional interlayer states. Each electron (deep blue spheres) in the system is bound with two intralayer magnetic flux quanta (black arrows) and one interlayer flux quantum (red arrows).

6.3 Composite fermion transformation: integer and half-integer composite fermion filling factors

We demonstrate that $\nu_{eq} = 2/5$ state can be understood with a generalized composite fermion (CF) picture. For the double-layer, we introduce multiple species of gauge field (flux quantum), coupling fermions in different layers as well as in the same layer. For our purposes, we choose the coupling constants so that a CF in a given layer sees two flux quanta attached to every other electron in the same layer, but only one flux quantum attached to electrons in the other layer. (Fig. 6.4 right). We only work in $|\nu_{top}|, |\nu_{bot}| < 1$ region, and we assume that electrons are spin and valley polarized. By generalizing the single layer CF picture, it is natural to define CF filling factors p_A and p_B for the top and bottom layers respectively. These are defined as the ratio between the fermion density in a given

layer to the effective magnetic field felt by CFs in that layer (see Appendix B):

$$p_A = \frac{\nu_{top} B}{B - 2n_{top}\phi_0 - n_{bot}\phi_0} = \frac{\nu_{top}}{1 - 2\nu_{top} - \nu_{bot}}, \quad p_B = \frac{\nu_{bot}}{1 - 2\nu_{bot} - \nu_{top}}. \tag{6.1}$$

Inverting Eq. 6.1, the LL filling factors for electrons in the two layers will then be given by

$$\nu_{top} = \frac{p_A(1 + p_B)}{1 + 2p_A + 2p_B + 3p_A p_B}, \quad \nu_{bot} = \frac{p_B(1 + p_A)}{1 + 2p_A + 2p_B + 3p_A p_B}. \tag{6.2}$$

In the case where the layers have equal density, this formula simplifies to $\nu_{eq} = p/(3p + 1)$, where $p = p_A = p_B$.

The experimentally observed interlayer correlated state $\nu_{eq} = 2/5$ corresponds to the composite fermion filling factors $p_A = p_B = -2$. Since the CFs in both layers are correlated, the Hall signal in both layers must be correlated as well. Using the Chern-Simons (CS) field calculation, we obtain the double layer Hall resistivity tensor obeys (see Appendix B for derivation):

$$\hat{\rho}_{xy} \equiv \begin{pmatrix} \rho_{xy}^{top} & \rho_{xy}^{drag} \\ \rho_{xy}^{drag} & \rho_{xy}^{bot} \end{pmatrix} = \hat{\rho}_{CS} + \hat{\rho}_{cf} = \begin{pmatrix} 2 & 1 \\ 1 & 2 \end{pmatrix} + \begin{pmatrix} 1/p_A & 0 \\ 0 & 1/p_B \end{pmatrix}. \tag{6.3}$$

In this equation, $\hat{\rho}_{xy}$ is Hall resistivity matrix in the unit of resistance quantum, which contains two contributing terms: $\hat{\rho}_{CS}$ originates from the motion of the CS flux considering the two intralayer flux quanta and one interlayer flux quantum, while $\hat{\rho}_{cf}$ is caused by Hall effect of CFs. At $\nu_{eq} = 2/5$, Eq. (6.3) produces $R_{xy}^{drag} = 1$ and $R_{xy}^{drive} = 3/2$, matching the experimental observations in

Fig. 6.3.

Applying similar CF formalism discussed above (Eq.6.1) to $\nu_{eq} = 3/7$, however, we obtain $p_A = p_B = -3/2$, indicating that two half-filled CF LLs are involved in this state. A half-filled CF LL by itself should not develop an incompressible state. Moreover, if we were to enforce Eq. (6.3) for these values of p_A and p_B, we would predict $\rho_{xy}^{drag} = 1$ and $\rho_{xy}^{drive} = 4/3$, which is in strong disagreement with the experimentally observed values, $2/3$ and $5/3$, respectively.

In order to correct the weakly interacting CF model presented above for half-filled CF LLs, we can draw an analogy between the half-filled CF double-layer system to the half-filled electron double-layer system, in which an exciton condensate can be formed. If we assume pairing between CFs in one layer and CF holes in the second layer, the CF Hall resistivity tensor becomes

$$\hat{\rho}_{cf} = \frac{1}{p_A + p_B} \begin{pmatrix} 1 & 1 \\ 1 & 1 \end{pmatrix}. \tag{6.4}$$

Inserting Eq. (6.4) into Eq. (6.3), we obtain $R_{xy}^{drag} = 2/3$ and $R_{xy}^{drag} = 5/3$, which agrees with our experimental observations, thus suggesting the CF exciton condensation phase is indeed responsible for $\nu_{eq} = 3/7$ (Further discussion of CF paring in half-filled CF LLs can be found in Appendix B).

6.4 Semi-quantized fractional quantum Hall states

Away from equal filling status, Fig. 6.5 shows that the vanishing R_{xx}^{drag} persists along segments of two symmetric lines (labeled by L1 and L2) that intersect at $\nu_{eq} = 2/5$. The line L2 has a slope of

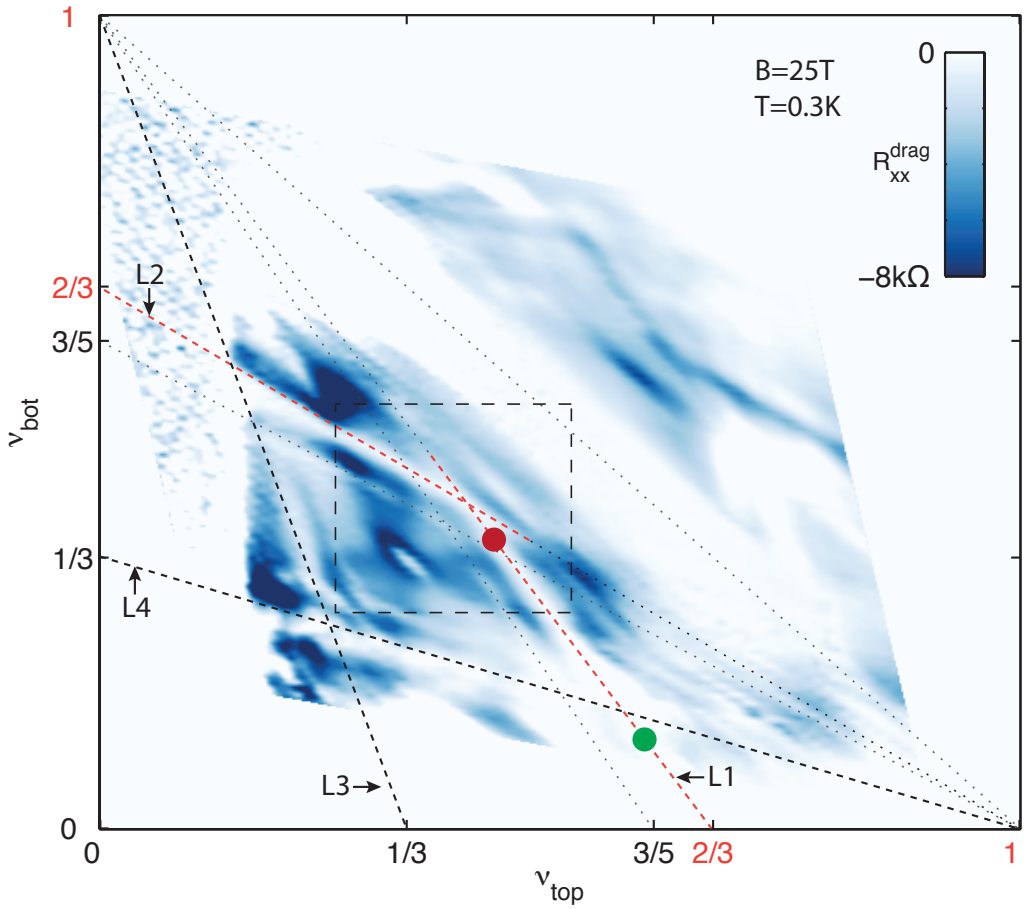

Figure 6.5: Longitudinal drag resistance as a function of filing factors in the top and bottom layer. Dotted lines show locations of semi-quantized states where longitudinal drag resistance vanishes. All these lines connect filling factor $\nu = 1$ in one layer with various filling factors $\nu = 1/3, 3/5, 2/3, 1$ of the other layer. Among them, the intersection of red dotted lines marked by L1 and L2 corresponds to the $\nu_{eq} = 2/5$ state discussed above, and the intersection of L3 and L4 is $\nu_{eq} = 3/7$. The dashed rectangle denotes the scope of zoomed-in measurements of Fig. 6.6.

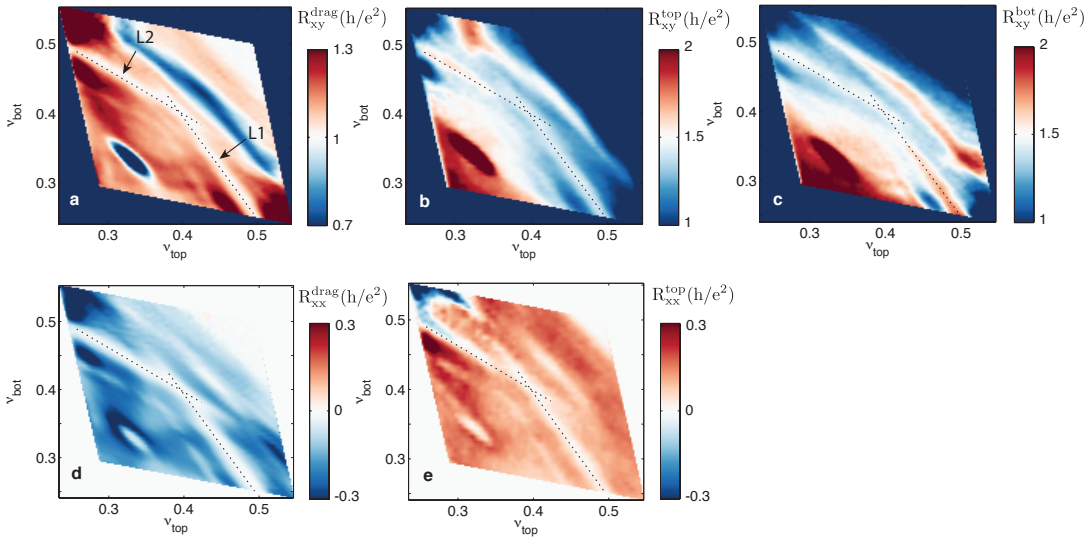

Figure 6.6: Various resistance measurements in the zoomed-in area indicated by dashed rectangle in Fig. 6.5. $R^{top}_{xx,xy}$ ($R^{bot}_{xx,xy}$) is drive layer resistance when current is driven on the top (bottom) layer. The dotted lines mark L1 and L2 (same as red lines in Fig. 6.5). Along L1, quantum Hall signatures ($R^{top}_{xx} = 0, R^{top}_{xy} = 3h/2e^2$) persist on the top layer but not on the bottom layer ($R^{bot}_{xx} \neq 0, R^{top}_{xy} \neq 3h/2e^2$) while the opposite is true for L2. Meanwhile, drag signals are quantized along both L1 and L2.

-2/3 and traces from $(\nu_{top}, \nu_{bot}) = (0, 2/3)$ to $(1, 0)$, while L1 is the inverse. We find that the longitudinal drag vanishes and Hall drag remain quantized along these lines, as shown in Fig. 6.6 and Fig. 6.7, indicating the strong interlayer interaction persists. Unlike the quantized interlayer drag resistance, which is layer-independent, we find that the drive Hall resistance depends on which layer we measure. For example, along L2, we find driving the bottom layer exhibits QHE with $R^{bot}_{xy} = 3/2$ and $R^{bot}_{xx} = 0$. However, when we drive the top layer along L2, $R^{top}_{xx} > 0$ and R^{top}_{xy} is not quantized. Along the L1, the role of the top and bottom layers is reversed. The experimental observed behaviors of all the resistance components along L1 and L2 are summarized in Fig. 6.8.

We note that along L1 or L2, the composite fermion filling factor of one of the layers (p_A or p_B)

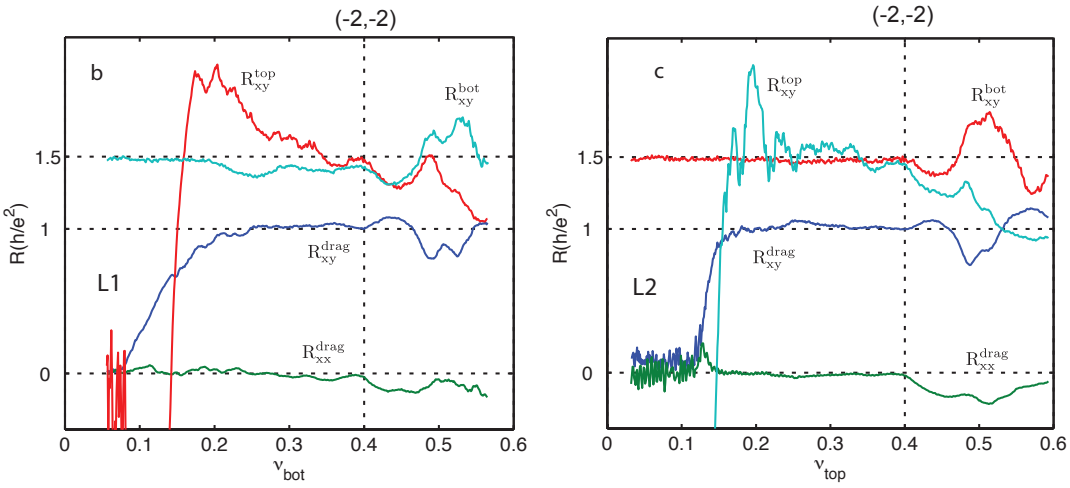

Figure 6.7: Linecut along L1 and L2 shown in Fig. 6.5. For L2, it is notable that R_{xy}^{bot} remained constant all the way until $\nu_{eq} = 2/5$ (vertical dotted line), across the phase transition between single layer $\nu_{bot} = 2/3$ fractional quantum Hall state ($R_{xy}^{drag} \approx 0$) and interlayer fractional quantum Hall state ($R_{xy}^{drag} = h/e^2$), while the opposite is true for L1.

	R_{xx}^{drag}	R_{xy}^{drag}	R_{xx}^{top}	R_{xy}^{top}	R_{xx}^{bot}	R_{xy}^{bot}
L1	0	h/e^2	0	$1.5h/e^2$	≠0	N.Q.
L2	0	h/e^2	≠0	N.Q.	0	$1.5h/e^2$

Figure 6.8: Summary of resistance behavior along L1 and L2 shown in Fig. 6.5. N.Q. stands for non-quantized.

remains at -2 while the other can change continuously. For example, for $p_B = -2$, the filling factors (ν_{top}, ν_{bot}) given by Eq. (6.2) satisfy the expression of L2: $(\nu_{top} + \frac{3}{2}\nu_{bot} = 1)$. In principle, a series of discrete incompressible FQH states can be formed along this line, corresponding to various positive and negative integer values p_A in Eq. (6.2). These should all exhibit vanishing longitudinal resistance, quantized $R_{xy}^{drag} = 1$ and $R_{xy}^{bot} = 3/2$, which do not depend on p_A, while the quantized values of R_{xy}^{top} would depend on the value of p_A. What originally surprised us, however, is that the experimentally observed quantization of $R_{xy}^{drag} = 1$ and $R_{xy}^{bot} = 3/2$, together with vanishing R_{xx}^{drag} and R_{xx}^{bot}, exists continuously along an entire segment of L2, even when p_A is not an integer.

We now understand the above results as follows. For a general point on the line segment L2, there is an energy gap for adding or removing a CF of type B (changes δp_B), but not of type A (change of δp_A). Thus, while the state should not be as stable as at a point where CF filling factors p_A and p_B are both integers, so that both species of CF are gapped, it should nevertheless be more stable than at a nearby points where both CF filling factors are fractions. Therefore, it is plausible that CF states along a line where one of (p_A, p_B) is an integer should be good candidates for the true ground state at the corresponding filing fractions. We call such states *semi-quantized*, as one CF filling factor is fixed but the other can vary continuously.

To understand transport properties in a semi-quantized state, we first note that in the absence of CF scattering or of pinning by impurities, there would be no longitudinal resistance and the Hall resistances would be given by Eq. (6.3), even in the absence of an energy gap. As shown in the Appendix B, if an electric current is applied to the bottom layer (drive), while no current can flow in the top layer (drag), then the current can be carried entirely by CFs of type B (bottom drive),

with no driving force on CFs of type A (top drag), and no motion of those CFs. Since type B CFs are contained in a filled CF-LL, the current is carried without dissipation. Furthermore, as there is no tendency for flow of the type A CFs, a small density of impurities will have no effect. Thus, we should find $\rho_{xy}^{bot} = 3/2$ and $\rho_{xy}^{drag} = 1$ for the semi-quantized states along L2. On the other hand, if current is applied to the top layer, CFs of type A will be forced to move. If CFs in the partially filled CF LL are not pinned by impurities, they will participate in the motion, and the they can be scattered by impurities. This will lead to a longitudinal resistance, and deviations from the result $R_{xy}^{top} = (2 + 1/p_A)$ predicted by Eq. (6.3). On the other hand, in a case where p_A is sufficiently close to an integer value so that the small density of CFs or holes in the partially filled LL can be pinned by impurities, there will again be no dissipation, and the value of R_{xy}^{top} will be pinned at the value corresponding to the nearby integer value of p_A.

Finally, we turn to the state at $\nu_{eq} = 1/4$ and the lines through it (Fig. 6.9). The state $\nu_{eq} = 1/4$ may be described in our CF language by $p_A = p_B = 1$. The state is also equivalent to the Halperin (331) state which has been proposed as a possible explanation for the FQH state at $\nu_{tot} = 1/2$ in wide GaAs quantum wells (detail in Appendix B). The line L3 in Fig. S2, which passes through this point, corresponds to $p_A = 1$ with continuously varying p_B. Although there appears to be a well-developed FQH state at $p_B = 2$ with $p_A = 1$ along this line, corresponding to the values $\nu_{top} = 3/13,\ \nu_{bot} = 4/13$, there does not appear to be a line of semi-quantized states between these two points. The absence of the continuous semi-quantization along these lines suggests that the stabilization of interlayer correlated CF state requires microscopic consideration of the energetics of the quasiparticle addition to the system (see Appendix B).

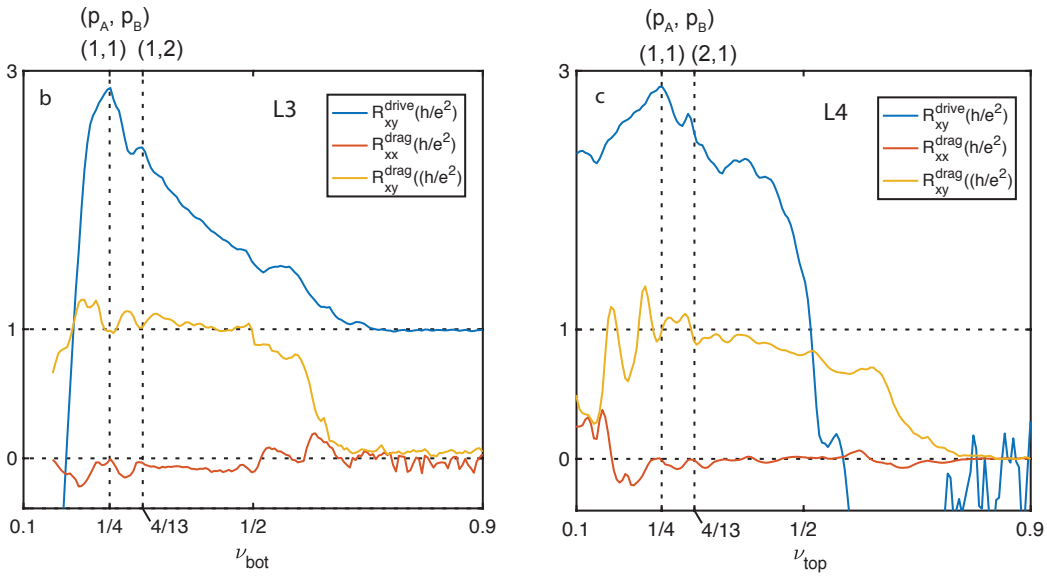

Figure 6.9: Left, linecut L3 through $(\nu_{top}, \nu_{bot}) = (1/4, 1/4)$. At $\nu_{top} = \nu_{bot} = 1/4$ (left vertical dashed line), the longitudinal drag vanish and Hall drag quantize to h/e^2. At the same time, the Hall resistance of the drive layer is close to the expected quantization value of $3h/e^2$. After composite fermion tranformation, $\nu_{top} = \nu_{bot} = 1/4$ becomes $(p_A, p_B) = (1, 1)$, corresponding to a quantized interlayer state. Going away from $\nu_{top} = \nu_{bot} = 1/4$ along this linecut, the quantization is lost. However Hall drag and magneto-drag quantization recovers near $(\nu_{top}, \nu_{bot}) = (3/13, 4/13)$ (right vertical dashed line). This filling factor correspond to composite fermion filling $(p_A, p_B) = (1, 2)$, another quantized interlayer state. Right, linecut L4 through $(\nu_{top}, \nu_{bot}) = (1/4, 1/4)$ in a different direction.

6.5 Anyon (quasi-particle) pairing

A more intuitive alternative approach to understanding properties of the states along L1 and L2 is to begin with the balanced quantized state at $\nu_{eq} = 2/5$, and add quasi-holes to this state (Fig. 6.10 right). Elementary quasi-holes in this state have total charge $-e/5$, with $-3e/5$ in one layer and $+2e/5$ in the other. This addition of one or another type of quasi-hole will move the system along the line L1 or L2, in a direction decreasing the total filling factor. The relative stability of states on the two line segments can be understood considering the energy cost for quasi-holes versus quasiparticles (See the Appendix B for more discussion). Similarly, near the end of L1 or L2, we can consider quasi-holes with charge of $-e/3$. Near filling factor (2/3, 0), the quasi-particles on the top layer are $2/3e$ charged while the quasi-particles on the bottom layer are simply electrons. The bound state of these two quasi-particles will move the system along L1 (Fig. 6.10 left).

The quasi-particle pairing picture also provides an intuitive way to understand the Hall resistance quantization along L1 and L2. For example, let us model states along L2 by starting from the endpoint (0, 2/3), considering filling factors $(\nu_{top}, \nu_{bot}) = [\delta, 2/3(1-\delta)]$, with δ small. (Fig. 6.11). The state (0, 2/3) consists of a completely empty top layer and a bottom layer in a conventional quantized Hall state with $\nu = 2/3$. We may suppose that for a suitable strength of interaction between the layers, an electron added to the top layer would bind strongly to a pair of $e/3$ quasi-holes in the top layer, giving rise to a combined quasiparticle whose total charge is one-third of an electron charge, $-e/3$. Further, we may suppose that the state with $\delta \neq 0$ is formed by addition of a finite density of these compound quasiparticles to the (0,2/3) ground state. .

If a current I is driven on the bottom layer, it will be carried solely by electrons in the $\nu = 2/3$ ground state, with no motion of the quasiparticles. Schematically, we can say that the current is carried by the FQH edge state of the $\nu = 2/3$ layer. (Fig. 6.11 a). The quasiparticles cannot contribute a net current, because that would require a current of electrons in the top layer, in violation of the boundary condition in the drag geometry. The absence of quasiparticle motion requires, in turn, that the net force on a quasiparticle is zero, which will occur if and only if the electric field in the lower layer is 3/2 times the field in the bottom layer. Furthermore, in order to get a net current I from the edge states in the lower layer, the Hall voltage in that layer must be equal to $3Ih/2e^2$. Thus we find $R_{xy}^{drive} = 3/2,\ R_{xy}^{drag} = 1$, in units of h/e^2.

In the case where we drive current I on the top layer, the current must be carried by quasiparticles, since there are no edge states in the upper layer. (Fig. 6.11 b). This current drags a quasiparticle current of $-2I/3$, in the opposite direction, on the bottom layer. This current must be canceled by a $2I/3$ edge current on the bottom layer, which requires that there be a Hall voltage $V_{xy}^{drag} = \frac{3h}{2e^2} \times \frac{2}{3}I = \frac{h}{e^2}I$. By contrast, the voltage V_{xx} and V_{xy} in the top layer will be non-quantized, and will depend on details such as the amount of impurity scattering, as well as the value of δ. Thus we have a quantized Hall drag effect in this configuration, despite having no quantized Hall effect in the top layer.

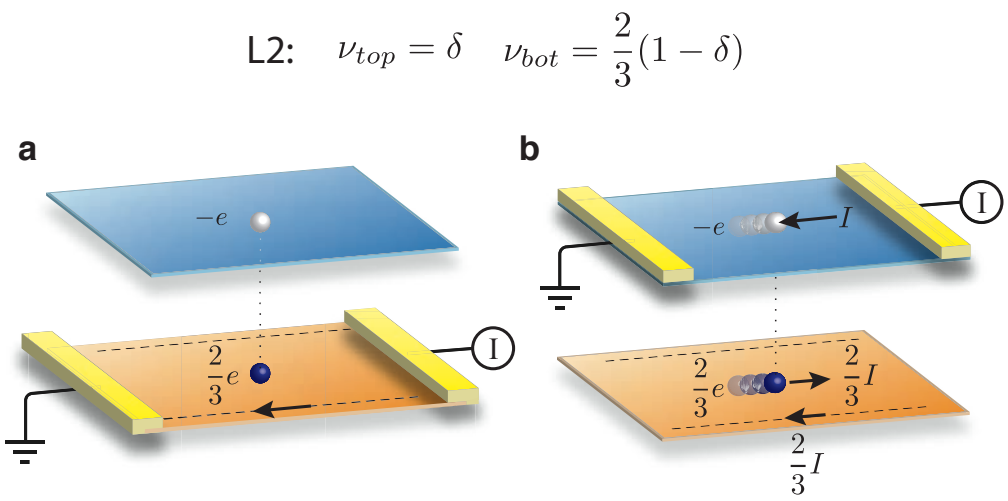

Figure 6.10: Illustrations of quasiparticle pairing for two filling factor configurations (green and red dots in Fig. 6.5). The left is for filling factor along L1 near (2/3, 0), while the right diagram is for near (2/5, 2/5). The circles on the two graphene layers represent quasiparticle excitations with marked electrical charges ($-e, 2/3e, etc.$). These quasiparticle pairs are balanced by the transverse electrical fields on the top and bottom layer (E_{top} and E_{bot} depicted by black arrows).

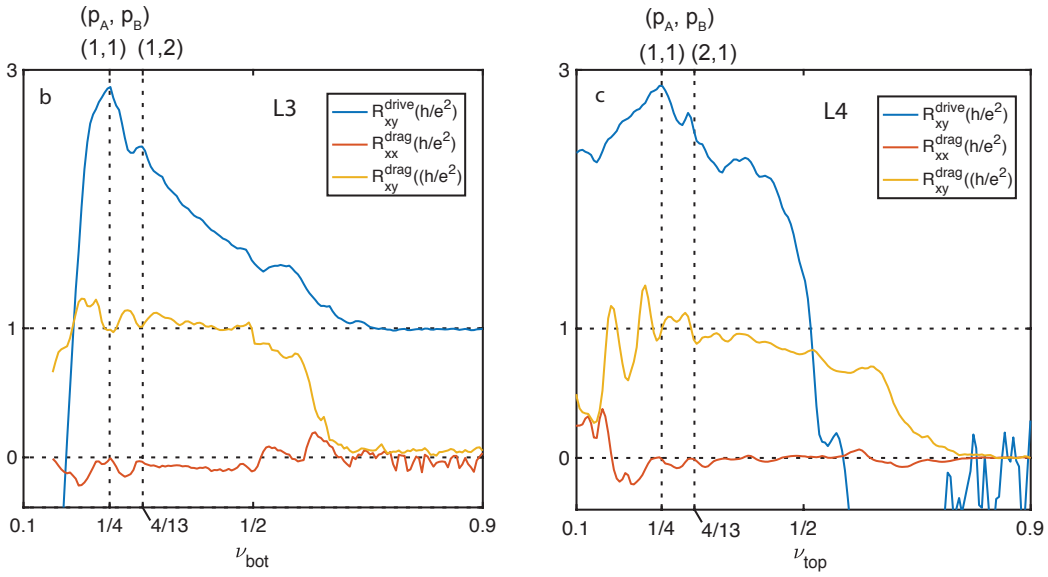

Figure 6.11: Schematic of transport in a semi-quantized state along the line L2, starting from the (0, 2/3) reference state. The dashed line on the edge of the bottom layer represent a 2/3 FQH edge state. Quasiparticles in this model consist of an electron in the nearly-empty top layer (white sphere) bound to a pair of anyons (quasi-holes) with total charge $2e/3$in the bottom layer. (a). When current is driven in the bottom layer, all the current can be carried by the 2/3 edge state (black arrow), while the quasiparticles remain stationary. (b). Current flowing on the top layer is carried solely by the quasiparticles, due to the absence of an edge state on the top layer. Hence, a drive current I in the top layer drags along a current $-2I/3$ in the bottom layer, which must be canceled by an edge current $2I/3$ in the opposite direction. This requires that there be a Hall voltage in the bottom layer, $V_{xy}^{drag} = (2I/3)(3h/2e^2) = I(h/e^2)$. Thus we have quantized drag in this configuration, despite no quantized Hall effect in the top layer.

A

Sample fabrication details

A.1 2D heterostructure Stacking

Here I describe the process of stacking various 2D material layers into a heterostructure. This method assembles the stack without contaminating the critical layers with polymer or solvent, keeping them in their pristine condition. This is achieved by picking up a top hBN layer with a polymer stamp and picking up the subsequent layers with the top hBN. Thus the graphene layers and hBN layers

other than the top layer are never in direct contact with the polymer stamp. At the end of pick-ups, we deposit the stack on the last layer or on a fresh SiO_2/Si substrate. The whole process relies on different behaviors of PPC (Polypropylene carbonate) at different temperatures. Below 30C, PPC acts like a solid, and can be smoothly peel off from a substrate. From 30C to about 70C, PPC goes through a glass transition and is very sticky. It crawls across the substrate when making contact with or detaching from a substrate. At this stage, the contact boundary can be precisely controlled the temperature or z-position of the manipulator. At about 90-100C, PPC totally melts down and become less sticky to the stack, so we can deposit the stack on the substrate.

I first prepare 2D material flakes through mechanical exfoliation. I use Scotch green magic tape for exfoliation. After spreading a single crystal of hBN or graphite on a tape until it can cover the whole area of a SiO_2/Si chip (1.3cm in dimension, Fig. A.1), the tape is taped down on a SiO_2 chip. I scratch the tape using a small glass vial filled with water to make the tape adhere well with the substrate. Then the tape is peeled off the SiO_2 substrate slowly over a couple of minutes. After finding the flakes of desired thickness and geometry, I use non-contact mode AFM to confirm the cleanness of the flakes. Dirty flakes are then abandoned. Graphene layer number is extracted from the contrast of green channel across the graphene edge. 6-8% contrast correspond to a single layer graphene, while 11-15% is for bilayer graphene. hBN with thickness between 20-40nm usually appears blue to green, while thicker flakes looks green to yellow and thinner flakes are purple to blue.

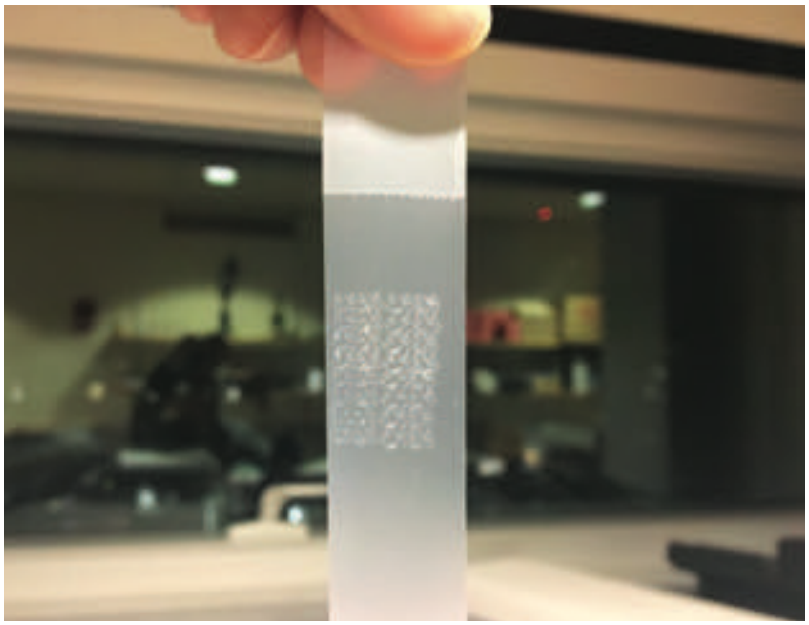

Figure A.1: Scotch tape after spreading hBN crystal on it through repetitive sticking and peeling.

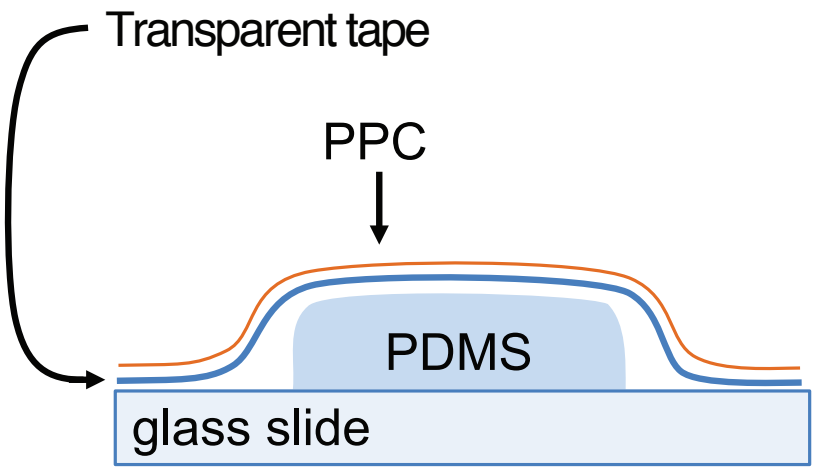

Figure A.2: Structure of the PPC transfer stamp.

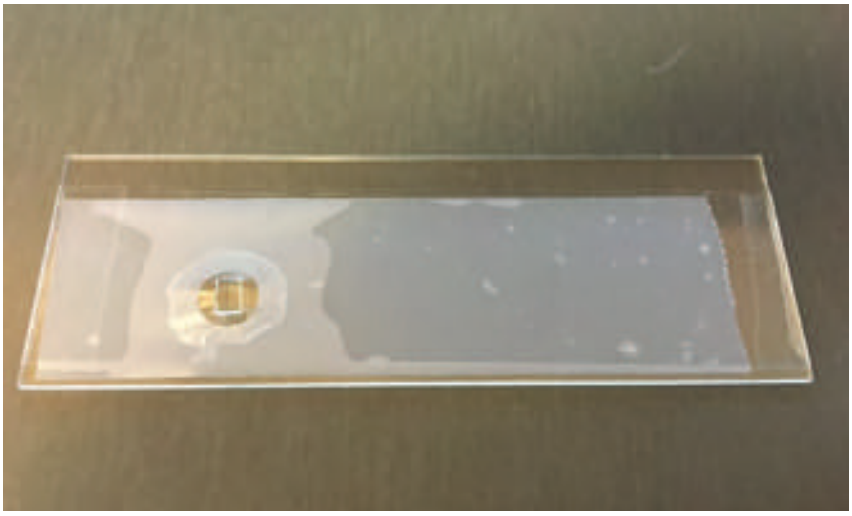

Figure A.3: Image of a transfer stamp on a glass slide.

A.1.1 Preparing transfer stamp

The transfer stamp is made of PPC, transparent tape and PDMS on a glass slide (Fig. A.2,Fig. A.3). PPC is the polymer in direct contact with top hBN layer. The transparent tape presses the PDMS block down on the glass slide and has good adhesion to the PPC film. So PPC will not fall off the PDMS block during pick-up. I use the scotch transparent tape from 3M. The PDMS block provides a elastic base for the transfer stamp which also make it extrude from the glass slide.

First cut a piece of PDMS about $3 \sim 5$mm in size from a pre-made PDMS sheet and lay it down on a clean glass slide. Then we tape a transparent tape on the PDMS block. Last the PPC film is deposited on top. Below, I narrate the procedures of making PDMS sheet and PPC film.

Preparing PDMS

The PDMS is made by mixing the PDMS elastomer with curing agent in 10:1 ratio. I mix them with a dedicated mixer at 2000rpm for one minute. After mixing, there will be a lot of bubbles in the mixture. The bubbles can be removed by setting in a vaccum or defoaming with a centrifuge (2000rpm for 1 min).

After mixing, we pour it onto a Petri dish with glass slides in it. If uniform thickness PDMS is desired, sandwich two cut glass slide pieces between two original glass slides, so PDMS in between will be the same thickness as a glass slide. Then bake it in a oven at 65C for 3 hours.

Preparing PPC (Polypropylene carbonate)

Dissolve 15g PPC in 100mL Anisole, stir it overnight at 60C with a magnetic stir. After PPC completely dissolved, filter it through a 0.2um filters. I found that many 0.2um filters on the market does not work properly. The working one we use are Whatman Autovial syringeless filters with 0.2um PTFE membrane.

After the PPC solution is made, I spin it on a clean silicon chip about 1cm-by-1cm in size. The spinner setting are 1000rpm/s acceleration, 1min duration, and speed usually between 2000-4000rpm. The speed is not critical unless aiming for a specific PPC thickness. After spinning, bake the PPC chips on a hot plate at 90-95C for 5mins or longer to remove all the anisole solvent.

To pave the PPC film on the transparent tape, I use a opaque tape to grab the ppc film and suspend it over a hole on the opaque tape. First punch a hole (about 5mm in diameter) on a green

magic tape using a hole puncher. Cover the PPC chip with the opaque tape and align the hole to a clean area on the PPC. Put down the tape and press all around the hole to make sure the tape adhere to PPC. Carefully peel the tape off the PPC chip until a smaller corner is expose. If the PPC membrane did not come up with the tape, scratch the exposed chip corner with tweezers and put the tape back down on the chip and peel it off again. This should be able to remove the PPC from the silicon chip and suspend it over the hole. If PPC does not come off, it is likely that the silicon chip is dirty. If the PPC over the hole is wrinkled, bake it at 60-80C until it becomes flat. After that, carefully lay it on top of the tranparent tape/PDMS stamp and make good adhesion by pressing on the tape around the suspended PPC. If the PPC is not completely flat, bake it at 60C until it flattens out.

To reuse the silicon chip, sonicate the chips in acetone and then IPA for 10 mins each. Blow dry the chips after sonication.

A.1.2 Cold pickup

Setup

The first hBN layer is usually picked up with so called cold pick-up method. First put the transfer stamp glass slide in the micro-manipulator clamp with the ppc facing down (Fig. A.4). Usually I apply a small tilt on the transfer glass slide so that I know where the stamp will first land on the substracte. Make sure the starting temperature is below 29C. Find the first hBN layer and turn on the vacuum to fix the chip on the stage. For PPC pick up to work, usually the top hBN layer need to be

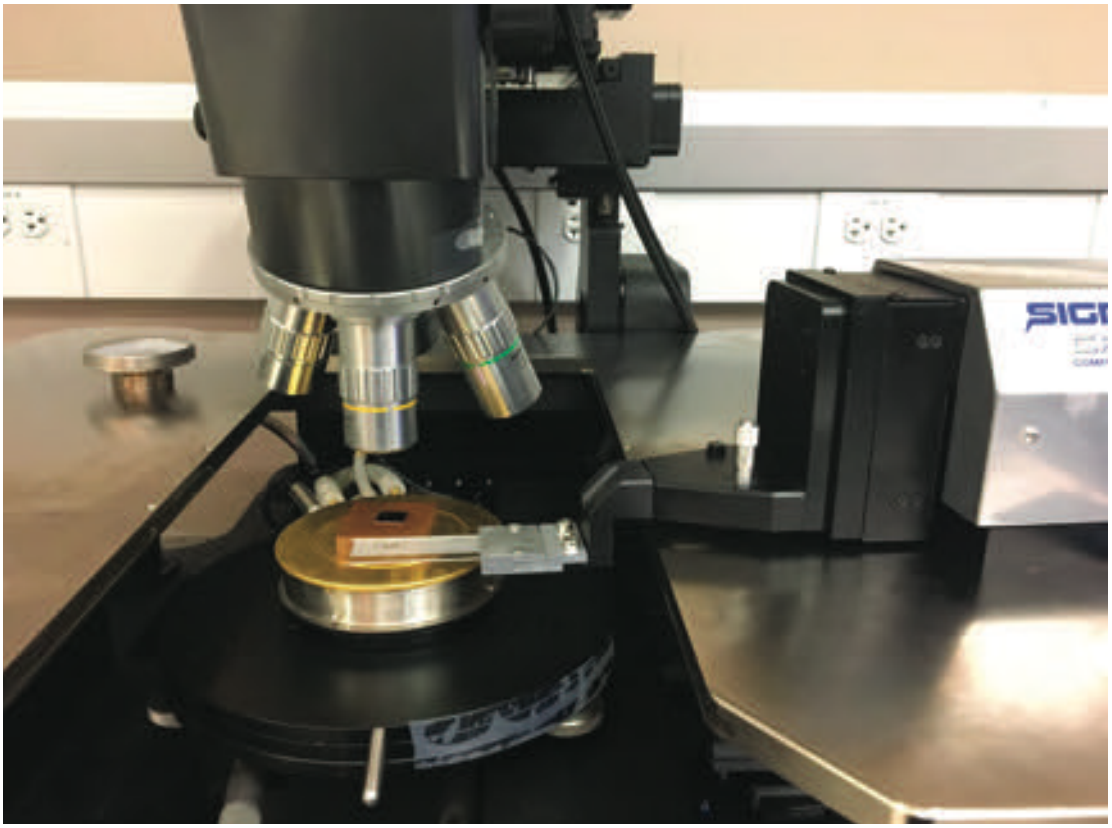

Figure A.4: The transfer stage.

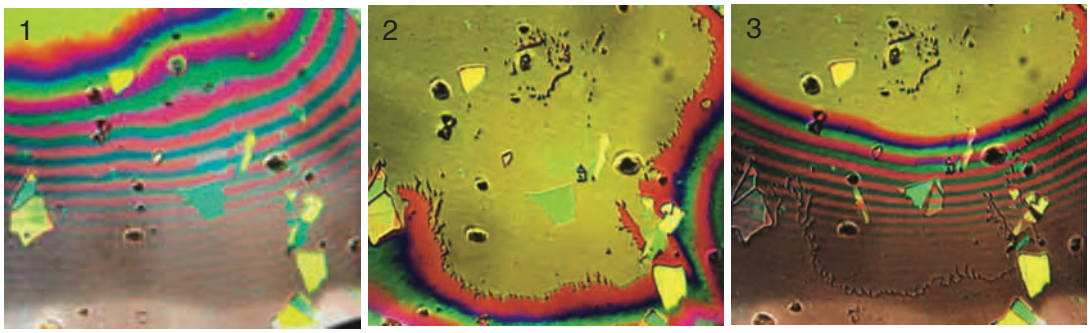

Figure A.5: Cold pick-up of first hBN layer. In the first panel, PPC have yet contacted the hBN (cyan flake near the center). The rainbow colors are the interference pattern between PPC and the substrate. The approaching direction is from top to bottom. On the top left corner, PPC already touched the substrate, which can be seen from the solid gold color. On the second panel, the PPC already made contact with the hBN flake. Third pane, ppc film is been lift-up. Half of the hBN flake is picked up, the picked up part will look almost transparent, while the part not picked up is still cyan.

thicker than 20nm. If the top hBN is thinner than 15nm, it is very difficult to pick up as there is not enough edge for the PPC to grab on. In this situations, stickier transfer polymer such as PC (Polycarbonates) can be used.

Making contact

1. Find a clean area on the PPC stamp and align it with the desired flake.
2. Lowering the transfer stamp until the contact boundary is close to the flaking being picked up.
3. Heat up the substrate to 40-60C until the whole flake is contacted by the stamp. Press down the stamp bit more, as the boundary usually jumps back slightly during peeling off.

Peeling off

1. Now decrease the set temperate to 29C and wait for it to cool down to 29C.
2. Lift up the stamp with a steady speed not to fast nor slow. Ideally we want it to be as slow as possible, but the ppc will stick to the substrate and jumps from one trapped line to the next if going too slowly. So practically, the peeling off is done fairly quickly, over typically 30s to 1min.
3. Most of the time, the flake is then picked up. If not, try this again or approach from a different direction. If part of the flake is picked up while the other part remains on substrate (still stay one piece, Fig. A.5), heating up the stage back to 45C and slowly raise the stamp. As the PPC being peeled off, the part of hBN on the PPC often can drag the remaining part of hBN on the substrate up as well.

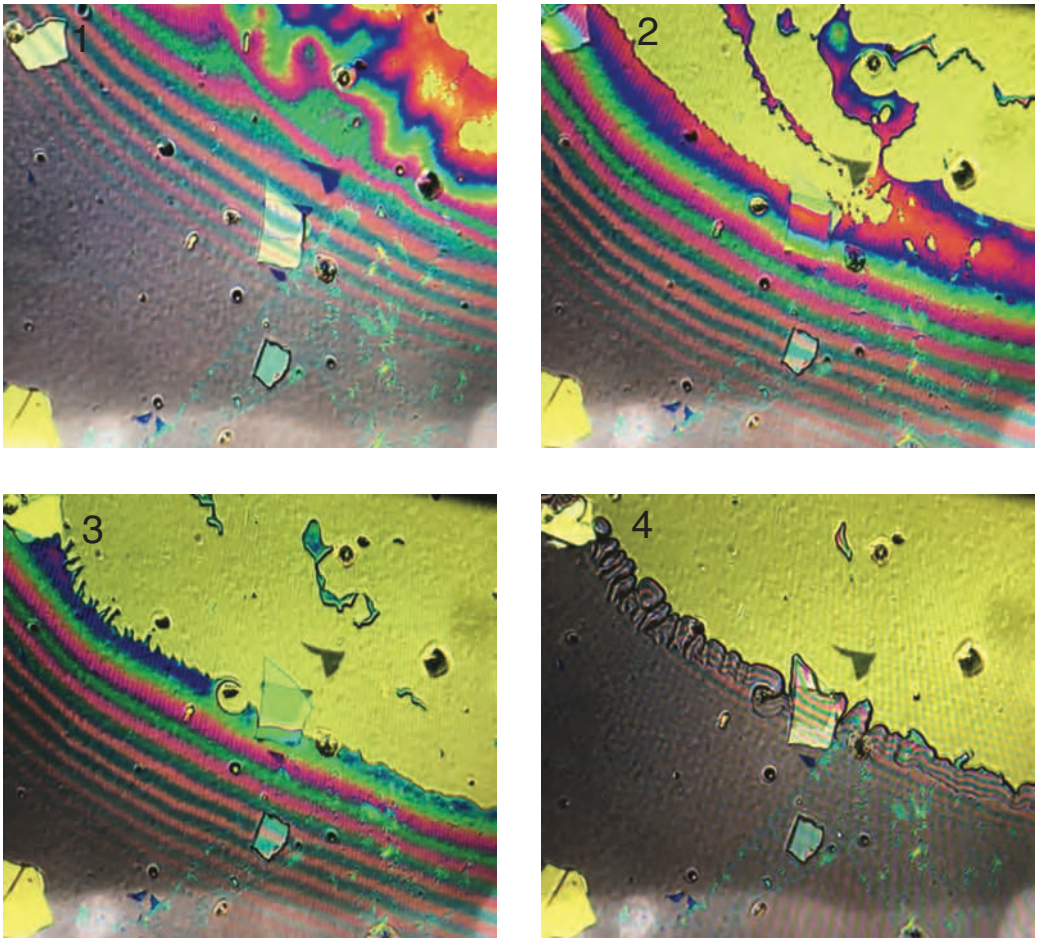

Figure A.6: Hot pickup of first graphite layer with hBN layer on PPC. 1. Align the hBN with the graphite flake before making contact. The white semi-transparent flake in the middle is top hBN, while the graphite is the purple color layer underneath the hBN. 2. hBN just start to contact the graphite flake. 3. The hBN is in full contact with the to-be-picked-up graphite. This is the point I start to lift up the PPC film. 4. The graphite is now picked up.

A.1.3 Hot pickup

Subsequent pick up steps are often done at 40-60C, as it is more controllable and precise than the cold pick-up method. Fig. A.6show the process of picking up graphite with a hBN on PPC stamp. This step is similar to the cold pick-up in many ways. However, there are some key differences as well.

1. Start at 29C, align the picked up flakes with the flake-to-be-picked-up before PPC touches the substrate. Leave some space on the top hBN layer beyond the flake-to-be-picked-up (Fig. A.6 first panel). This means the flake-to-be-picked-up can be fully contacted by the top hBN but at the same time the top hBN is not in full contact with the substrate (third panel in Fig. A.6). This makes sure we can peel the stack off the substrate instead of dropping it down.

2. Heat up the substrate to about 40C and press down on the PPC stamp. Before the two flakes start to touch, check the alignment again. If the alignment is slightly off, move the manipulator to realign the flakes. When the PPC is in contact with substrate, it moves slowly as if it is dragging along on the substrate. At this point, the PPC contact boundary should be quite close to the flakes. If not, press down the stamp more.

3. Increase the temperature and let the PPC slowly makes contact. Be careful not let the two flakes snap onto each other very quick, as they usually tend to do so when flakes first touch. If the contact happens fast, raise the PPC slightly to stop the sudden movement. Let the flakes slowly making contact until the flake-to-be-picked-up made full contact(Fig. A.6 panel 3). This should happen below 70C.

4. Raise the manipulator, before the top hBN is totally dropped onto the substrate again. And keep raising it slowly by hand or auto-clicker (0.3um per 5-10s) until the PPC is completely detached from substrate. The temperature of this step should be 45 55C. The peeling process usually last 10-30 mins.

A.1.4 Depositing the stack

Putting down the stack is similar to the hot pick-up for the contacting part. Align the flakes and slowly heat up to make the contact just as before. However, the desired contact temperature at the stack for this step is above 60C. Higher temperature helps reduce bubbles. Also when putting down, we want the stack to be in complete contact with the substrate instead of leaving a corner or edge up on the PPC (Fig. A.7 left). After full contact, heat the substrate to 100C, at the same time raise the transfer stamp if PPC boundary is moving too far beyond the stack. Then lift the PPC slowly (0.3um per 5-10s), which should now detach from the stack (Fig. A.7 right).

After the PPC is completely peeled off from the substrate, clean the PPC residue by soaking in acetone for 5 mins. And anneal in 350C vaccum annealer for 15 mins. The vacuum level is usually below $1 \times 10^{-6} torr$, but I found it is not critical.

A.2 Nano-fabrication

In this section, I cover methods and recipes for etching the stacking, making edge contacts and fabricating metal gates. Usually device fabrication start with depositing metal alignment marks. I measure the distance from the stack to the left and bottom edge of the substrate and use this coordinate

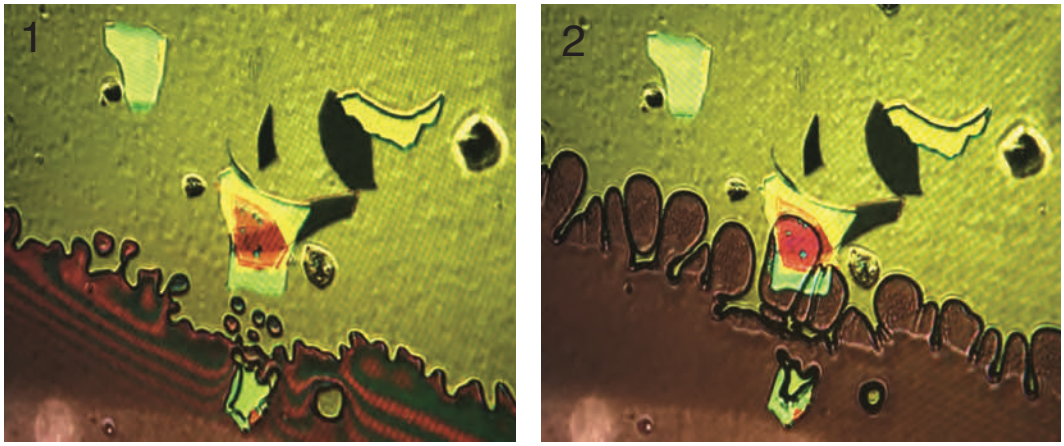

Figure A.7: Dropping down the finished stack at 100C. 1. The stack in the middle is dropped down on the substrate with PPC layer still on top. 2. The PPC is slowly peeled off, and the stack stayed on the substrate.

to place the alignment marks around the sample. For the samples with graphite top gate, top gate is first patterned with HSQ mask and RIE etching. Then the stack is patterned into final geometry with another HSQ mask and etching step. PMMA mask is used for metal deposition for contacts and metal gates. Last if more layer of top gates are needed, a ALD Al_2O_3 layer is deposited over the whole substrate. Additional metal top gates or contact gates are patterned on top of the ALD layer.

A.2.1 PMMA mask and evaporation

For the steps involving PMMA masks (alignment marks, contacts and metal gates), I use a double layer PMMA recipe for easier lift off: 1. Spin PMMA 495 A4 at 2000rpm, 1000rpm/s acceleration for one minute. 2. Bake at 180C for two minutes. 3. Spin PMMA 950 A2 at 4000rpm, 1000rpm/s acceleration for one minute. 4. Bake at 180C for two minutes. Make sure the chip is cool before spinning the second layer and start the spinner right away after dropping the resist to avoid bottom

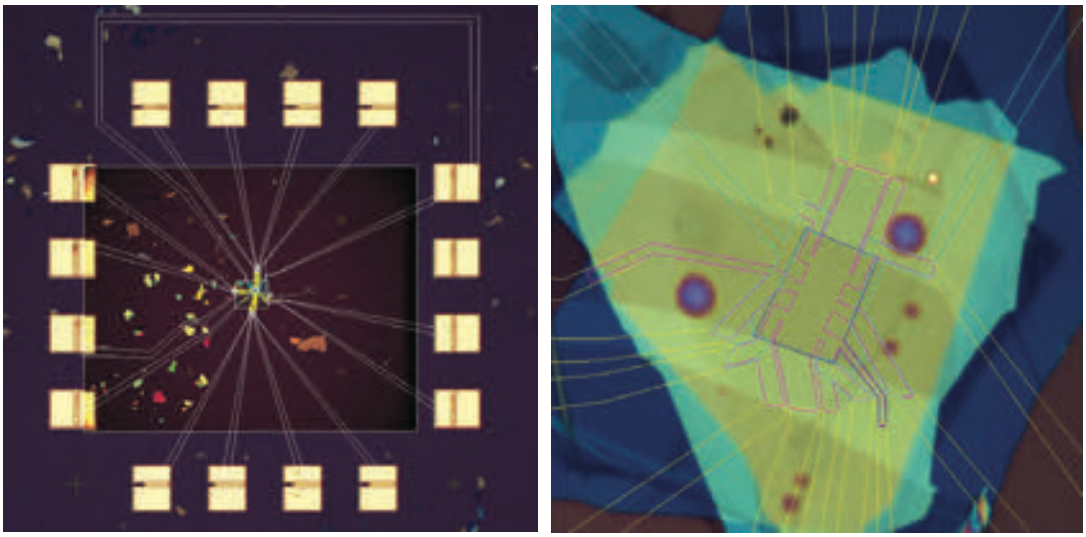

Figure A.8: Fabrication design. Left, overview of big features (about 2mm-by-2mm). Each bonding pad (gold color rectangles) is split into two parts. I bond on the outside pads first, if there SiO2 is punched through during bonding, the outside pads will be unlinked by scratching off the connects between two bonding pads, and inner pads will be used on second attempt. Right, zoomed-in view of the sample. The optical image is taken right after depositing alignment marks. The deep blue color lines are edge of top graphite gate etch mask. The purple color outline is for etching the device into final geometry. The yellow outlines are contacts to graphene layers and graphite gates. The light blue colored lines are for contact gates.

PMMA layer getting dissolved. I write the PMMA mask in Elionix F125 at $2000uC/cm^2$ and 10nm pitch. The PMMA is developed in IPA/MIBK (1:3) developer for 1min before rinsing in IPA.

The metals are then evaporated onto the sample with PMMA masks. For alignment marks and metal gates, the film quality is not critical and good vacuum is not needed. However, for the edge contacts, greater care must be taken as the film quality is critical for good contacts. I use a thermal evaporator for the contacts and let it pump down to low $10^{-7}torr$. To ensure good edge contacts, continuous rotation and a smaller tile angle (5-10deg) can help the metal cover all side of etched stack. A short CHF_3 RIE etch can also help make better contact by exposing a fresh graphene interface.

A.2.2 HSQ mask and etching

HSQ mask is used for the etching steps, as it is a negative resist (written part will remain after development) and it resist etching better than PMMA. Because written HSQ turns into glass and hard to remove, we use a thin PMMA buffer layer below the HSQ mask. First, PMMA 950 A2 is spun on the substrate at 6000rpm for a minute and baked at 180C for two minutes. Then HSQ is spun at 6000rpm as well with no subsequent bake. The HSQ is writting on Elionix F125 as well at $950uC/cm^2$ area dose. It is developed in MF-CD 26 developer for three minutes before rinsed in DI water. HSQ is sensitive to moisture and should be store in a fridge. I pour HSQ from the original bottle to a smaller container after warming up the bottle to room temperature to avoid water condensation. Each time, HSQ is pour out from the smaller container after warming up to room temperature. Both containers should be sealed with a parafilm.

For the top graphite etch, first one minute of O_2 plasma is used to remove the thin PMMA layer

underneath the etch mask. The O_2 plasma have little effect on hBN. Then a plasma with CHF_3 as the main ingredient is used to etch hBN layer but it will stop on the top graphite layer as CHF_3 is not effective in etching graphite. Another run of O_2 etch is used to etch the top graphite and stops at the second hBN layer. HSQ etch mask is then removed by socking in acetone for a few minutes.

For the device etch, O_2 plasma is also run first to remove thin PMMA. And then CHF_3 plasma is used to pattern the rest of the stack including graphene. In certain cases, O_2 and CHF_3 might need to run alternatingly if there is graphite above the contact area. In these cases, make sure CHF_3 is the last etching step.

A.2.3 ALD and contact gates

In order to deposit metal gate above the device (for top gate or contact gates), an insulating layer must be deposited first. Otherwise the overlap between metal gates and graphene edge will short the gates with graphene. I choose Al_2O_3 as the insulating layer. ALD deposition can cover all sides of the device and metal leads, thus is an ideal way of growing the Al_2O_3 layer. However, due to the hydro-phobic nature of hBN and graphene, ALD, which use water as precusor, does not grow on the stack. So I evaporator a thin layer (1-2nm) of aluminum on the stack first. After taking it out of the evaporator, air will oxidize the aluminum to Al_2O_3. This thin layer of Al_2O_3 acts as a seed layer for the rest of ALD Al_2O_3 growth. I usually grow the ALD at 250C for 20nm-30nm.

After the ALD step, an metal gate is deposited with PMMA mask. I always try to minimize the overlap between metal gates and other metal contacts, to reduce the chance of gates leaks with graphene contacts.

B

Theory of interlayer fractional quantum Hall effect

The appendix is relevant theory written by Prof. Bertrand Halperin with minor changes.

B.1 Composite fermion transformation and Hall resistivity

$n_i = (\nu_i B/\phi_0)$ is the electron density in layer i, where $i = (A, B)$ labels the top and bottom layer, respectively. If we attach two intralayer flux quanta and one interlayer flux quantum, the Chern-Simons field seen by composite fermions in layer i is

$$b_i = \phi_0(2n_i + n_{i^*}), \tag{B.1}$$

where i^* denotes the layer opposite to i. After substracting the Chern-Simons field, the remaining magnetic field seen by the CFs in layer i is

$$\Delta_i = B - b_i \tag{B.2}$$

where B is the applied magnetic field. We may then define effective Landau level filling factors for the CFs by

$$p_i \equiv \phi_0 n_i/\Delta_i. \tag{B.3}$$

We can now obtain Eq. 6.1.

We consider an infinite system, where the voltage gradients are produced by uniform electric fields in the respective layers, and we can neglect any contributions due to edge currents arising from differences in the chemical potentials at the two edges. With composite fermion transformation,

currents $\vec{j}_i$ in the two layers will generate Chern-Simons electric fields[97,98]:

$$\vec{e}_i = \phi_0 \hat{z} \times (2\vec{j}_i + \vec{j}_{i*}) \tag{B.4}$$

Then, If an electric field $\vec{E}_i$ is applied to layer i, the composite fermions in layer i will feel an effective electric field

$$\vec{F}_i = \vec{E}_i - \vec{e}_i. \tag{B.5}$$

In the limit of weak electric fields, we use linear response and write

$$E_{i\alpha} = -e \sum_{j,\beta} \hat{\rho}_{i\alpha,j\beta} j_{j\beta}\,, \qquad F_{i\alpha} = -e \sum_{j,\beta} \hat{\rho}^{cf}_{i\alpha,j\beta} j_{j\beta} \tag{B.6}$$

where $\hat{\rho}^{cf}$ is 4×4 resistivity matrix for CFs. Thus we have:

$$\hat{\rho} = \hat{\rho}^{CS} + \hat{\rho}^{cf}, \tag{B.7}$$

B.2 Quantized and Semi-Quantized Fractional Hall States

Fully quantized fractional Hall states can arise if both p_A and p_B are integers. Then, at least within mean field theory, there will be an energy gap for creation of any kind of excitation, and the state should be stable against small changes in the chemical potential of either layer. When there is a complete energy gap, there will be effectively no excited quasiparticles at sufficiently low temperatures in any of the composite-fermion Landau levels, so there will be no dissipation, and the resistivity

matrix will be given by Eq. 6.3.

However, we may also consider a situation where only one of the filling factors, say p_B is an integer. This means that there should be energy gap for changing p_B but not for p_A: the ground state energy should vary continuously with p_A, if p_B is held fixed. With some simple algebra, one can show that the resulting filling factors lie on a straight line, with

$$\nu_A + \alpha\nu_B = 1\,, \qquad \alpha = \frac{2p_B + 1}{p_B}\,. \tag{B.8}$$

We refer to generic states along these lines, at points where only one of the occupation numbers p_A, p_B is integer, as semi-quantized fractional Hall states.

As argued in chapter 6, if the drive current is applied to layer B, there will be no dissipation. In the present language, this is because $\vec{F}_A = 0$, in that case, and the CFs of type B reside in CF-LLs that are completely full. Consequently, we can still use Eq. 6.3 to compute the Hall resistivities. Thus $\hat{\rho}^B_{xy}$ and $\hat{\rho}^{drag}_{xy}$ should still remain quantized, with values $(2 + 1/p_B)$ and 1, respectively. However, if drive current is applied to layer A, then $\vec{F}_A$ will be nonzero, and there will generally be dissipation due to scattering of the CFs by impurities, Therefore, the prediction of Eq. 6.3 that $\hat{\rho}^B_{xy} = (2 + 1/p_A)$ cannot be trusted.

In contrast to the semi-quantized case, we may consider the unquantized case, where both p_A and p_B are non-integer. In this case we have partially filled Landau levels for composite fermions of both species. Now, even in the absence of disorder, composite fermions of the two types will scatter off each other, unless their drift velocities are identical. The velocities will only be equal if

the electrical field is identical in the two layers, which is not the case in the drag experiments we are considering. Thus we would expect to find dissipation even in the absence of impurities.

For unquantized states along the symmetric line $\nu_A = \nu_B$, if we were apply equal current densities in the two layers, the electric fields would also be equal in the two layers. Therefore, in the absence of disorder, there should be no dissipation in this case, and there will be no longitudinal voltage drop in either layer. On the other hand, if the currents are equal and opposite in the two layers, the electric fields should be opposite in the two layers, and there would be dissipation due to the scattering between composite fermions in opposite layers, if p_A and p_B both not integers. In this case, in the absence of impurities, we will have nonzero longitudinal electric fields which are equal and opposite in the two layers.

The longitudinal voltage in a drag experiment, where current flows only in one layer, may be obtained by adding the two previous cases. We see that in the absence of disorder, the longitudinal electric field should remain equal and opposite in the two layers, *i.e.*, for the unquantized states along the symmetry line, we should have $\rho_{xx}^{drag} = -\rho_{xx}^{drive}$. Experimental results along the symmetry line are at least approximately consistent with this expectation, suggesting that scattering between the two types of composite fermions is more important than the scattering by disorder in this case.

B.3 Quasiparticles

For a fully quantized system, with a proper energy gap, the elementary excitations are found to be quasiparticles and quasi-holes, with fractional charges that are precisely quantized in each of the

two layers. As an example, we may consider the gapped symmetric case at $(2/5,\ 2/5)$. Generalizing the Laughlin procedure[85], we may generate a quasiparticle by inserting a zero-diameter solenoid at a point $\vec{r}_0$, and turning on current in the solenoid so that it contains precisely one quantum of magnetic flux. Since we have a symmetric system with total filling $\nu_{tot} = 4/5$, this procedure will expel 2/5 of an electron charge from the vicinity of $\vec{r}_0$ in each layer, and send it to the boundary of the sample. If we now deposit an extra electron at point $\vec{r}_0$ in layer A, we will have created an "A-type" quasiparticle, with 3/5 of an electron charge in layer A, and -2/5 in layer B, for a total charge of -e/5. We may create an "A-type" quasi-hole, with -3/5 of an electron charge in layer A, and 2/5 in layer B, using the reverse procedure, where we change the sign of the flux through the solenoid and remove an electron from layer A. Type-B quasiparticles or quasi-holes can be created in the same way, by adding or subtracting the electron in layer B. By adding or subtracting quasiparticles or quasi-holes of type A, we can shift the filling factors (ν_A, ν_B) along the line L2, with slope -2/3, whereas by adding or subtracting quasiparticles of type B, we move along the line L1, with slope -3/2.

If the density of quasiparticles is sufficiently small, so that they do not overlap, we can continue to talk about quasiparticles with quantized charges. At some point, however, the charge associated with a particular quasiparticle becomes ambiguous, and only the total charge in each layer is well defined. If one progresses far enough from the (2/5,2/5) state along the line L2 with slope -2/3, one will pass through a number of states with $p_B = -2$ and integer p_A. If our CF model is still a correct description of the system, then the ground states should be fully quantized states, with complete energy gaps. Then, if the temperature is well below the energy gap, the charged excitations will be quasiparticles and quasi-holes, with quantized charges, which will generally not be the same as those

at (2/5, 2/5). However, in each case, we can find quasiparticles with minimal total charge and with a ratio of charges of -2/3 between layer B and layer A. For example, at the end point (0,2/3) we would find quasiparticles with charge 1 in layer A and -2/3 in layer B. (We may understand this quasiparticle as a bound state of an electron in the empty layer with a pair of $e/3$ quasi-holes in the layer with $\nu_i = 2/3$.) In fact, it appears that the CF model where each CF sees two flux quanta attached to CFs in the same layer and one for the opposite layer is not the correct description for fractions with $\nu_A \leq \approx 0.2$, but the example illustrates the point. More generally, for fully quantized states located on the the line, we would find quasiparticles whose charges in the two layers are given by

$$q_A = 3q_T\,, \quad q_B = -2q_T\,, \quad q_T = \frac{p_A + 1}{4p_A + 3}\,, \tag{B.9}$$

with q_T being the total charge of the quasiparticle. Thus in all these cases, one could move along the semi-quantized line by adding quasiparticles of the designated type.

Transport properties of a semi-quantized state can be understood in terms of the properties of quasipaprticles, without referring to the motion of CFs. At a point on L2 with ν_{top} slightly less than 2/5, we may describe the ground state as the quantized (2/5,2/5) state, with a nonzero density of type-A quasi-holes. If a current is sent through the bottom layer (layer B), the current can be carried by the quantized background state, which as we have seen will generate a Hall voltage in layer A that is 2/3 the Hall voltage in layer B. Since the type-A quasi-holes have a charge ratio of -3/2, the electric fields in the two layers exert no net force on the quasi-holes. Also, current carried by the background state engenders no longitudinal electric field in either layer. Consequently, it is consistent that the

quasiparticles will not move and there is no diissipation. By contrast, if the current is applied to layer A, the Hall field in layer A will be 3/2 times the field in layer B, so there will be a net force on the quasi-holes. If the quasi-holes are not pinned, they will move under this force and dissipation will result.

B.4 The (3/7, 3/7) State

The discussion above has been concerned with states where at least one of the parameters p_A, p_B is an integer, and the ground state can be understood using a mean field theory of non-interacting CFs. This is not the case for the quantized Hall state at (3/7, 3/7), where $p_A = p_B = -3/2$. Now we have one full effective Landau level, and one half-full level for each species of CF. For the half-full level, we must take into account interactions between the CFs. We shall assume that there is a pairing between particles of one species and holes in the other, so that the wave function for composite fermions in the partly-filled level can be described by the familiar (111) state. Alternatively, we may say that there is a superfluid Bose condensate of excitons formed from the composite fermions. In this state, there can be no difference in the effective electric field $\vec{F}_i$ felt by the CFs in different layers, regardless of any difference in the currents between layers. Moreover, if current is distributed so that the CFs have the same velocity in the two layers, then interactions between the CFs play no role, and the effective field should have the same value as for uncoupled layers, $\vec{F}_i = \hat{z} \times \vec{j}/(p_A + p_B)$, where $\vec{j}$ is the total current density int the two layers. This implies that the Hall resistivity matrix for CFs is given by Eq. 6.4.

We may contrast these results with what one might have found from some alternate models of the (3/7, 3/7) state. For example, one could have supposed that the quantization resulted because CFs in the half-full LLs form Cooper pairs separately within each layer, in analogy with the models that have been proposed to explain the FQH state at $\nu = 5/2$ in GaAs[99]. This would result in a diagonal form for the CF Hall resistivity matrix, identical to that in Eq. 6.3 of the main text. Alternatively, one could have imagined that Cooper pairs are formed between CFs in opposite layers (as opposed to pairing between CFs and holes). This would result in a CF Hall resistance matrix proportional to $\begin{pmatrix} 1 & -1 \\ -1 & 1 \end{pmatrix}$. In either of these cases, the results predicted for the Hall drag resistivity would disagree with our experimental results.

Small deviations from the stable point (3/7, 3,7) along the line where $\nu_{tot} = 6/7$ can be achieved by adding vortex excitations, which have total charge zero but non-zero charge in each layer separately. Although there will be an energy cost for adding these vortices, it is plausible that the energy cost may be smaller than the energy to add a quasiparticle with net charge different from zero. In this case, one should find a valley of relatively stable configurations along the line $\nu_{total} = 6/7$, in the vicinity of (3/7, 3/7). These states are similar to those in the valleys emanating from quantized states with integer p in the sense that they are achieved by adding to the parent state quasiparticles of a single type, which have a fixed ratio of the charge in each layer. Therefore, if the ratio of the electric fields in the two layers is properly chosen, the quasiparticles will not feel a force and can remain stationary, even in the absence of pinning, and there will be no dissipation.

In the present case, the absence of dissipation should occur if the electric fields are equal in the

two layers. If the electric fields unequal, the quasiparticles will move, which will lead to dissipation if there is scattering due to impurities. However, the dissipation would still vanish in the absence of impurities, as there is only one type of quasiparticle, and they would all drift at the same velocity.

We may note that for small deviations from the symmetric point, states along the line $\nu_{total} = 6/7$ can be parametrized by $(p_A = -3/2 + \epsilon,\ p_B = -3/2 - \epsilon)$. However, for larger values of ϵ, the resulting filling factors do not lie on this line but rather on a curve which passes through the points (1,0) and (0,1). In any case, once the deviation from (3/7, 3/7) becomes large, interactions between quasiparticles will be important, and we cannot say much about the resulting state.

In our experiments, we see some evidence for semi-quantized states along a line of slope -1 in the vicinity of the point (3/7, 3/7). However, these states do not extend very far from symmetric filling, and we do not see evidence for curvature of the line.

B.5 Relation to trial wavefunctions

The mean field ground states that we have described in the language of fermions coupled to Chern-Simons fields, have direct counterparts in the language of CF trial wave functions, introduced by Jain[87]. The trial wave function corresponding to a state with CF fillings $(p_A,\ p_B)$ can be written as

$$\Psi = P_{LLL}\Psi_{p_A,p_B}\{z_i, w_k\}\prod_{i<j}(z_i - z_j)^2\prod_{k<l}(w_k - w_l)^2\prod_{i,k}(z_i - w_k), \tag{B.10}$$

where z_i and w_k are the positions of electrons in the two layers, in complex coordinates, $\Psi_{p_A,p_B}\{z_i, w_k\}$ is the wave functions for a set of non-interacting electrons in a state with p_A filled LLs in layer A and

p_B filled LLs in layer B, the operator P_{LLL} represents projection to the lowest LL, and we have omitted the single-particle Gaussian factors.

In the case of our quantized Hall state at (1/4, 1/4), corresponding to $p_A = p_B = 1$, the wave function Ψ_{p_A,p_B} is already confined to the lowest LL, and the projection operator can be omitted. The wave function in this case may be written as

$$\Psi_{331} = \prod_{i<j}(z_i - z_j)^3 \prod_{k<l}(w_k - w_l)^3 \prod_{i,k}(z_i - w_k), \tag{B.11}$$

which is identical to the Halperin (331) wave function for an FQH state with $\nu_{tot} = 1/2$, which is considered a possible model for such observed states in wide GaAs quantum wells.

Another interesting case is generalization of the (3/7,3/7) state to a state with $p_A = p_B = 1/2$. If the function Ψ_{p_A,p_B} is chosen to be the Halperin (111) wave function, which is a description of the interlayer coherent IQH state with equal filling in the two layers, then the final wave function takes the form:

$$\Psi_{332} = \prod_{i<j}(z_i - z_j)^3 \prod_{k<l}(w_k - w_l)^3 \prod_{i,k}(z_i - w_k)^2, . \tag{B.12}$$

This is just the Halperin (332) wave function which was proposed for the ground state at $\nu_{tot} = 2/5$, for a collection of spin-1/2 electrons with negligible Zeeman splitting.

C

Anomalous drag in bilayer graphene double-layer under zero magnetic field

C.1 Sign reversal of Coulomb drag in double bilayer graphene

The Coulomb drag measurements in double bilayer graphene under zero magnetic field were motivated by searching of an exciton condensate phase. Instead, an unexpected drag signal arises. As

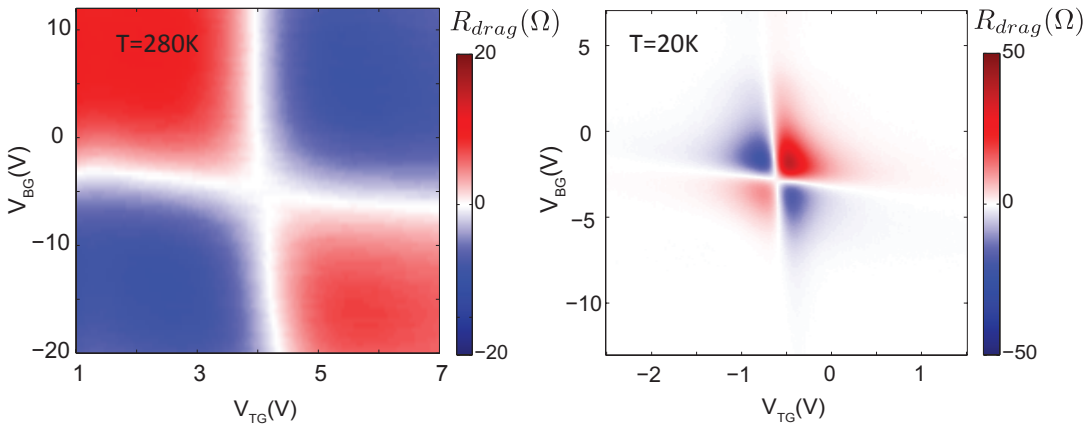

Figure C.1: Coulomb drag in bilayer graphene double-layer at high and low temperatures under zero magnetic field. In both measurements, the drag signal is divided into four quadrants by charge neutral lines of the top and bottom layers. The neutrality point is shifted between two measurements as they are taken from two different thermal cycles.

discussed in the introduction, longitudinal drag resistance due to momentum transfer or exciton condensation is negative when carrier types of both layers are the same and is positive when the two layers have opposite carrier types. This is indeed what was observed at relative high temperatures in bilayer graphene double layer (Fig. C.1 left).

However, upon cooling down, the sign of the drag signal reversed (Fig. C.1 right), i.e., is positive when both layers have the same carrier type and vice versa. And this reversed drag signal, which we call negative drag as it is negative of what is expected, become more pronounced at lower temperatures. The transition between normal drag and negative drag usually happens in the temperature range of 100-200K.

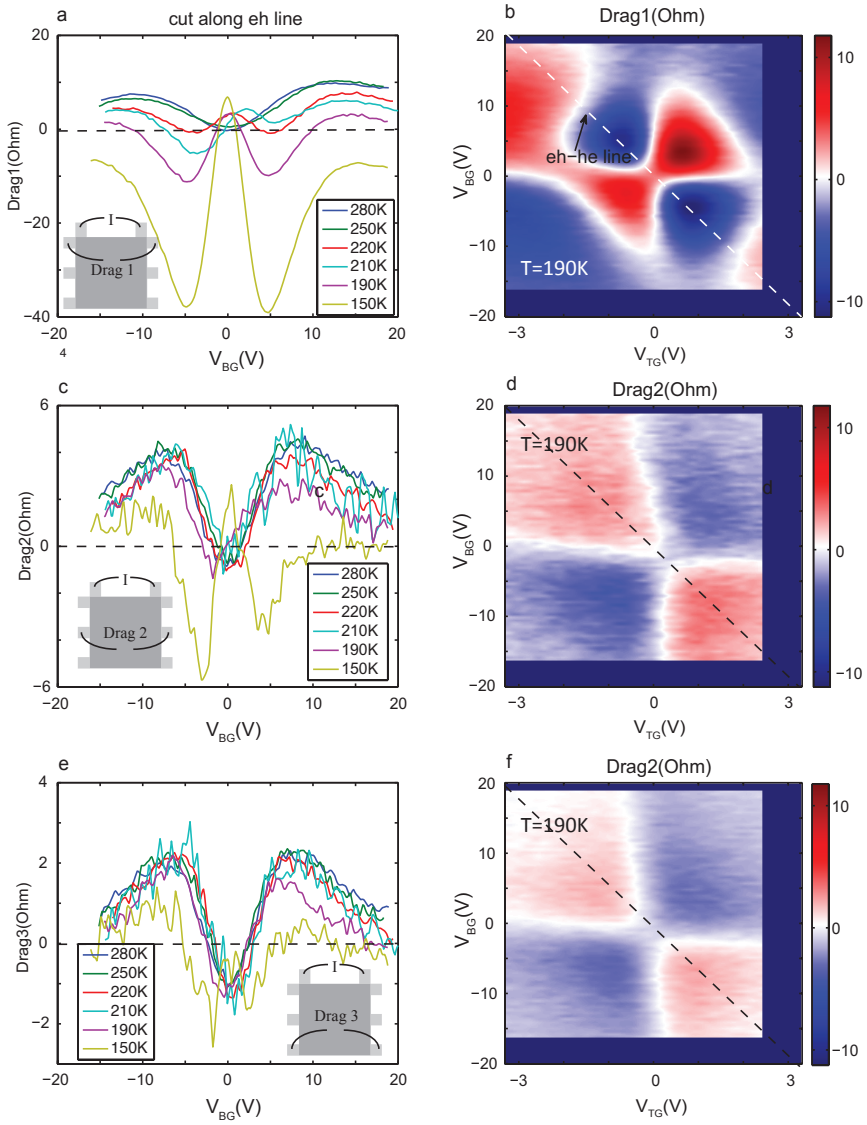

Figure C.2: Negative drag effect in different measurement geometry. In the local setup (panel b), negative drag effect already dominate at low densities under 190K, while drag sign of non-local setups (d and f) are still normal across all density range. a, c, e, drag along e-h linecut, where we can see the sign reversal occurs at 220K in the local setup, which becomes 150K for drag 2. The sign reversal for drag3 happens at an even lower temperature than 150K. a, c, e insets, corresponding measurement geometries.

C.2 Possible cause of the negative drag

Further investigation shows that the crossover temperature from normal drag to negative drag depends on the measurement geometry (Fig. C.2). For the local drag setup (Drag 1), where voltage leads in the drag layer are closest to current leads on the drive layer, the transition temperature is the highest. And below the crossover temperatures (at 150K), the anomalous drag is much stronger (order of 10 times) in the local setup comparing with non-local setups (Drag 2 and Drag 3). This large difference cannot be simply explained by the geometric factor. The first appearance of negative drag in the local setup and the fast decay of negative drag signal away from current leads suggests that the negative drag is an interface effect between contacts and graphene. We do note that upon cooling to even lower temperature (<20K), the difference of drag resistance from different configurations becomes smaller, recovering a geometric factor effect.

A possible explanation to these observations can be found in the energy drag mechanism (Fig. C.3). Energy drag describes the drag effect caused by energy transfer in between two graphene layers and were proposed to explain the Coulomb drag effect observed at double neutrality point in graphene double layers[34,36]. Here in our experiment, the locality of negative drag signal suggests it is related to the interface between current carrying graphene layer and drive layer contacts. I thus propose the following explaination:

On the drive layer, drive current creates a heating or cooling effect at the interface between graphene and metal contacts due to the Peltier effect (Fig. C.3). This creates a temperature gradient in the drive layer, which is transmitted to drag layer through interlayer energy transfer, resulting in a tem-

perature gradient on the drag layer as well. On the drag layer, temperature gradient generates thermoelectric voltage through Seebeck effect.

Assuming perfect thermo-equilibration between layers, we have the drag resistance:

$$\rho_{drag} = \frac{\Pi_{drive} S_{drag}}{\kappa_{drive} + \kappa_{drag}} = \frac{\S_{drive} S_{drag}}{L(\sigma_{drive} + \sigma_{drag})} \tag{C.1}$$

, in which Π is the Peltier coefficient, S is the Seebeck coefficient, κ is thermal conductances. Using the relationship between Peltier and Seebeck coefficient as well as the Wiedemann–Franz law, second half of eq. C.1 can be obtained. This proposed explanation first provides the correct sign for negative drag effect as can be seen in Fig. C.3, which is positive when both layers are doped the same. Also it explains the locality of negative drag signal in the medium temperature range as the temperature gradient is very local due to thermal equilibration by phonons away from the contact interface. When phonons fade away at lower temperatures (<20K), the temperature gradients can expand further and generate negative drag in the non-local configurations as well. Lastly, momentum drag signal dies off as T^2 when temperature is lowered but the Seeback coefficient decays slower than T. As can be seen in the published study of thermoelectric effect in graphene[100], S/T becomes larger at lower temperatures. This will make the energy drag more pronounced at lower temperatures comparing with momentum drag, agreeing with the observed temperature dependence. In following samples, we used longer graphene leads, which separates the graphene-metal interface further away from the channel and suppresses the negative drag effect.

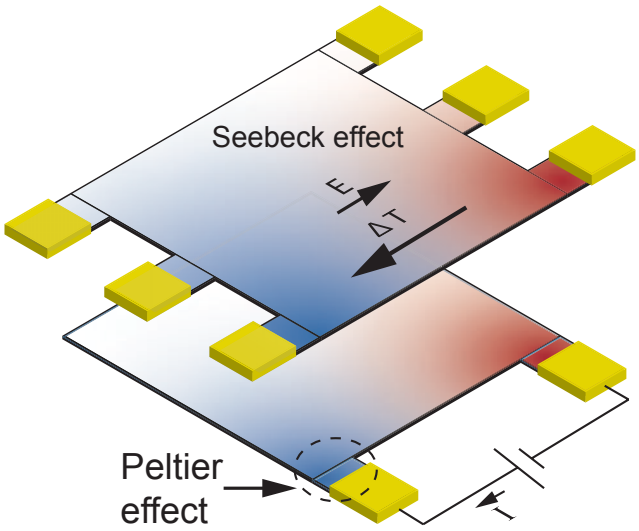

Figure C.3: Schematic of energy drag. Gold color blocks represent metal contacts. Red (blue) color represents higher (lower) temperature.

References

[1] P W Anderson. More Is Different. *Science*, 177(4047):393–396, 1972. ISSN 0036-8075. doi: 10.1126/science.177.4047.393. URL http://www.sciencemag.org/cgi/doi/10.1126/science.177.4047.393.

[2] Yuanbo Zhang, Yan-Wen Tan, Horst L. Stormer, and Philip Kim. Experimental observation of the quantum Hall effect and Berry's phase in graphene. *Nature*, 438(7065):201–204, nov 2005. ISSN 0028-0836. doi: 10.1038/nature04235. URL http://www.nature.com/doifinder/10.1038/nature04235.

[3] K S Novoselov, A K Geim, S V Morozov, D Jiang, M I Katsnelson, I V Grigorieva, S V Dubonos, and A A Firsov. Two-dimensional gas of massless Dirac fermions in graphene. *Nature*, 438(7065):197–200, 2005.

[4] Yuanbo Zhang, Tsung-Ta Tang, Caglar Girit, Zhao Hao, Michael C Martin, Alex Zettl, Michael F Crommie, Y Ron Shen, and Feng Wang. Direct observation of a widely tunable bandgap in bilayer graphene. *Nature*, 459(7248):820–3, jun 2009. ISSN 1476-4687. doi: 10.1038/nature08105. URL http://dx.doi.org/10.1038/nature08105.

[5] Andrea F. Young and Philip Kim. Quantum interference and Klein tunnelling in graphene heterojunctions. *Nature Physics*, 5(3):222–226, mar 2009. ISSN 1745-2473. doi: 10.1038/nphys1198. URL http://www.nature.com/articles/nphys1198.

[6] C. R. Dean, A. F. Young, P. Cadden-Zimansky, L. Wang, H. Ren, K. Watanabe, T. Taniguchi, P. Kim, J. Hone, and K. L. Shepard. Multicomponent fractional quantum Hall effect in graphene. *Nature Physics*, 7(9):693–696, may 2011. ISSN 1745-2473. doi: 10.1038/nphys2007. URL http://dx.doi.org/10.1038/nphys2007.

[7] A. F. Young, C. R. Dean, L. Wang, H. Ren, P. Cadden-Zimansky, K. Watanabe, T. Taniguchi, J. Hone, K. L. Shepard, and P. Kim. Spin and valley quantum Hall ferromagnetism in graphene. *Nature Physics*, 8(7):550–556, may 2012. ISSN 1745-2473. doi: 10.1038/nphys2307. URL http://dx.doi.org/10.1038/nphys2307.

[8] C R Dean, L Wang, P Maher, C Forsythe, F Ghahari, Y Gao, J Katoch, M Ishigami, P Moon, M Koshino, T Taniguchi, K Watanabe, K L Shepard, J Hone, and P Kim. Hofstadter's butterfly and the fractal quantum Hall effect in moiré superlattices. *Nature*, 497(7451):598–602, may 2013. ISSN 1476-4687. doi: 10.1038/nature12186. URL http://dx.doi.org/10.1038/nature12186.

[9] B Hunt, J D Sanchez-Yamagishi, A F Young, M Yankowitz, B J LeRoy, K Watanabe, T Taniguchi, P Moon, M Koshino, P Jarillo-Herrero, and R C Ashoori. Massive Dirac fermions and Hofstadter butterfly in a van der Waals heterostructure. *Science (New York, N.Y.)*, 340(6139):1427–30, jun 2013. ISSN 1095-9203. doi: 10.1126/science.1237240. URL http://www.sciencemag.org/content/340/6139/1427.

[10] L A Ponomarenko, R V Gorbachev, G L Yu, D C Elias, R Jalil, A A Patel, A Mishchenko, A S Mayorov, C R Woods, J R Wallbank, M Mucha-Kruczynski, B A Piot, M Potemski, I V Grigorieva, K S Novoselov, F Guinea, V I Fal'ko, and A K Geim. Cloning of Dirac fermions in graphene superlattices. *Nature*, 497(7451):594–7, may 2013. ISSN 1476-4687. doi: 10.1038/nature12187. URL http://dx.doi.org/10.1038/nature12187.

[11] Thiti Taychatanapat, Kenji Watanabe, Takashi Taniguchi, and Pablo Jarillo-Herrero. Electrically tunable transverse magnetic focusing in graphene. *Nature Physics*, 9(4):225–229, apr 2013. ISSN 1745-2473. doi: 10.1038/nphys2549. URL http://www.nature.com/articles/nphys2549.

[12] P. Maher, C. R. Dean, a. F. Young, T. Taniguchi, K. Watanabe, K. L. Shepard, J. Hone, and P. Kim. Evidence for a spin phase transition at charge neutrality in bilayer graphene. *Nature Physics*, 9(3):154–158, jan 2013. ISSN 1745-2473. doi: 10.1038/nphys2528. URL http://www.nature.com/doifinder/10.1038/nphys2528.

[13] Patrick Maher, Lei Wang, Yuanda Gao, Carlos Forsythe, Takashi Taniguchi, Kenji Watanabe, Dmitry Abanin, Zlatko Papić, Paul Cadden-Zimansky, James Hone, Philip Kim, and Cory R Dean. Bilayer graphene. Tunable fractional quantum Hall phases in bilayer graphene. *Science (New York, N.Y.)*, 345(6192):61–4, jul 2014. ISSN 1095-9203. doi: 10.1126/science.1252875. URL http://www.sciencemag.org/content/345/6192/61.short.

[14] A. F. Young, J. D. Sanchez-Yamagishi, B. Hunt, S. H. Choi, K. Watanabe, T. Taniguchi, R. C. Ashoori, and P. Jarillo-Herrero. Tunable symmetry breaking and helical edge transport in a

graphene quantum spin Hall state. *Nature*, 505(7484):528–532, jan 2014. ISSN 0028-0836. doi: 10.1038/nature12800. URL http://www.nature.com/articles/nature12800.

[15] B. M. Hunt, J. I.A. Li, A. A. Zibrov, L. Wang, T. Taniguchi, K. Watanabe, J. Hone, C. R. Dean, M. Zaletel, R. C. Ashoori, and A. F. Young. Direct measurement of discrete valley and orbital quantum numbers in bilayer graphene. *Nature Communications*, 8(1), jul 2017. ISSN 20411723. doi: 10.1038/s41467-017-00824-w. URL http://arxiv.org/abs/1607.06461.

[16] J. I.A. Li, T. Taniguchi, K. Watanabe, J. Hone, and C. R. Dean. Excitonic superfluid phase in double bilayer graphene. *Nature Physics*, 13(8):751–755, may 2017. ISSN 17452481. doi: 10.1038/NPHYS4140. URL http://www.nature.com/doifinder/10.1038/nphys4140.

[17] a. H. Castro Neto, N. M. R. Peres, K. S. Novoselov, and a. K. Geim. The electronic properties of graphene. *Reviews of Modern Physics*, 81(1):109–162, jan 2009. ISSN 0034-6861. doi: 10.1103/RevModPhys.81.109. URL http://link.aps.org/doi/10.1103/RevModPhys.81.109.

[18] Edward McCann and Mikito Koshino. The electronic properties of bilayer graphene. pages 1–27, may 2012. URL http://arxiv.org/abs/1205.6953v1.

[19] L Wang, I Meric, P Y Huang, Q Gao, Y Gao, H Tran, T Taniguchi, K Watanabe, L M Campos, D a Muller, J Guo, P Kim, J Hone, K L Shepard, and C R Dean. One-dimensional electrical contact to a two-dimensional material. *Science (New York, N.Y.)*, 342(6158):614–7, nov 2013. ISSN 1095-9203. doi: 10.1126/science.1244358. URL http://www.ncbi.nlm.nih.gov/pubmed/24179223.

[20] A. A. Zibrov, C. Kometter, H. Zhou, E. M. Spanton, T. Taniguchi, K. Watanabe, M. P. Zaletel, and A. F. Young. Tunable interacting composite fermion phases in a half-filled bilayer-graphene Landau level. *Nature*, 549(7672):360–364, sep 2017. ISSN 14764687. doi: 10.1038/nature23893. URL http://www.nature.com/doifinder/10.1038/nature23893.

[21] a K Geim and I V Grigorieva. Van der Waals heterostructures. *Nature*, 499(7459):419–25, jul 2013. ISSN 1476-4687. doi: 10.1038/nature12385. URL http://www.ncbi.nlm.nih.gov/pubmed/23887427.

[22] Pulickel Ajayan, Philip Kim, and Kaustav Banerjee. Two-dimensional van der Waals materials. *Physics Today*, 69(9):38–44, sep 2016. ISSN 00319228. doi: 10.1063/PT.3.3297. URL http://physicstoday.scitation.org/doi/10.1063/PT.3.3297.

[23] J.P. Eisenstein. Exciton Condensation in Bilayer Quantum Hall Systems. *Annual Review of Condensed Matter Physics*, 5(1):159–181, mar 2014. ISSN 1947-5454. doi: 10.1146/annurev-conmatphys-031113-133832. URL http://www.annualreviews.org/doi/abs/10.1146/annurev-conmatphys-031113-133832.

[24] G H Lee. Electron tunneling through atomically flat and ultrathin hexagonal boron nitride. *Appl. Phys. Lett.*, 99:243114, 2011. URL http://dx.doi.org/10.1063/1.3662043.

[25] L Britnell. Field-effect tunneling transistor based on vertical graphene heterostructures. *Science*, 335:947–950, 2012. URL http://dx.doi.org/10.1126/science.1218461.

[26] B. N. Narozhny and A. Levchenko. Coulomb drag. *Reviews of Modern Physics*, 88(2): 025003, may 2016. ISSN 0034-6861. doi: 10.1103/RevModPhys.88.025003. URL http://link.aps.org/doi/10.1103/RevModPhys.88.025003.

[27] MJ Kellogg. Thesis: Evidence for excitonic superfluidity in a bilayer two-dimensional electron system. 2005, 2005. URL http://thesis.library.caltech.edu/3080/.

[28] Antti-Pekka Jauho and Henrik Smith. Coulomb drag between parallel two-dimensional electron systems. *Physical Review B*, 47(8):4420–4428, feb 1993. ISSN 0163-1829. doi: 10.1103/PhysRevB.47.4420. URL https://link.aps.org/doi/10.1103/PhysRevB.47.4420.

[29] T J Gramila, J P Eisenstein, A H MacDonald, L N Pfeiffer, and K W West. Mutual friction between parallel two-dimensional electron systems. *Phys. Rev. Lett.*, 66:1216–1219, 1991. URL http://dx.doi.org/10.1103/PhysRevLett.66.1216.

[30] P. Solomon, P. Price, D. Frank, and D. La Tulipe. New phenomena in coupled transport between 2D and 3D electron-gas layers. *Physical Review Letters*, 63(22):2508–2511, nov 1989. ISSN 0031-9007. doi: 10.1103/PhysRevLett.63.2508. URL http://link.aps.org/doi/10.1103/PhysRevLett.63.2508.

[31] U Sivan, P M Solomon, and H Shtrikman. Coupled electron-hole transport. *Phys. Rev. Lett.*, 68:1196–1199, 1992. URL http://dx.doi.org/10.1103/PhysRevLett.68.1196.

[32] R. V. Gorbachev, a. K. Geim, M. I. Katsnelson, K. S. Novoselov, T. Tudorovskiy, I. V. Grigorieva, a. H. MacDonald, S. V. Morozov, K. Watanabe, T. Taniguchi, and L. a. Ponomarenko. Strong Coulomb drag and broken symmetry in double-layer graphene. *Na-*

ture Physics, 8(12):896–901, oct 2012. ISSN 1745-2473. doi: 10.1038/nphys2441. URL http://www.nature.com/doifinder/10.1038/nphys2441.

[33] S Kim. Coulomb drag of massless fermions in graphene. *Phys. Rev. B*, 83:161401, 2011. URL http://dx.doi.org/10.1103/PhysRevB.83.161401.

[34] M. Titov, R. V. Gorbachev, B. N. Narozhny, T. Tudorovskiy, M. Schütt, P. M. Ostrovsky, I. V. Gornyi, A. D. Mirlin, M. I. Katsnelson, K. S. Novoselov, A. K. Geim, and L. A. Ponomarenko. Giant Magnetodrag in Graphene at Charge Neutrality. *Physical Review Letters*, 111(16):166601, oct 2013. ISSN 0031-9007. doi: 10.1103/PhysRevLett.111.166601. URL http://link.aps.org/doi/10.1103/PhysRevLett.111.166601.

[35] Kayoung Lee, Jiamin Xue, David C. Dillen, Kenji Watanabe, Takashi Taniguchi, and Emanuel Tutuc. Giant Frictional Drag in Double Bilayer Graphene Heterostructures. *Physical Review Letters*, 117(4):046803, jul 2016. ISSN 10797114. doi: 10.1103/PhysRevLett.117.046803. URL http://link.aps.org/doi/10.1103/PhysRevLett.117.046803.

[36] Justin C.W. Song and Leonid S. Levitov. Hall drag and magnetodrag in graphene. *Physical Review Letters*, 111(12):126601, sep 2013. ISSN 00319007. doi: 10.1103/PhysRevLett.111.126601. URL http://link.aps.org/doi/10.1103/PhysRevLett.111.126601.

[37] Justin C W Song and Leonid S. Levitov. Hall drag and magnetodrag in graphene. *Physical Review Letters*, 111(12):1–5, mar 2013. ISSN 00319007. doi: 10.1103/PhysRevLett.111.126601. URL http://arxiv.org/abs/1303.3529v1.

[38] P B Littlewood, P R Eastham, J M J Keeling, F M Marchetti, B D Simons, and M H Szymanska. Models of coherent exciton condensation. *Journal of Physics: Condensed Matter*, 16 (35):S3597–S3620, sep 2004. ISSN 0953-8984. doi: 10.1088/0953-8984/16/35/003. URL http://stacks.iop.org/0953-8984/16/i=35/a=003.

[39] A A High, J R Leonard, A T Hammack, M M Fogler, L V Butov, A V Kavokin, K L Campman, and A C Gossard. Spontaneous coherence in a cold exciton gas. *Nature*, 483(7391): 584–8, mar 2012. ISSN 1476-4687. doi: 10.1038/nature10903. URL http://dx.doi.org/10.1038/nature10903.

[40] J A Seamons, C P Morath, J L Reno, and M P Lilly. Coulomb drag in the exciton regime in electron-hole bilayers. *Phys. Rev. Lett.*, 102:26804, 2009. URL http://dx.doi.org/10.1103/PhysRevLett.102.026804.

[41] Hongki Min, Rafi Bistritzer, Jung-Jung Su, and A. MacDonald. Room-temperature superfluidity in graphene bilayers. *Physical Review B*, 78(12):121401, sep 2008. ISSN 1098-0121. doi: 10.1103/PhysRevB.78.121401. URL http://link.aps.org/doi/10.1103/PhysRevB.78.121401.

[42] Maxim Kharitonov and Konstantin Efetov. Electron screening and excitonic condensation in double-layer graphene systems. *Physical Review B*, 78(24):241401, dec 2008. ISSN 1098-0121. doi: 10.1103/PhysRevB.78.241401. URL http://link.aps.org/doi/10.1103/PhysRevB.78.241401.

[43] A. Perali, D. Neilson, and A. R. Hamilton. High-Temperature Superfluidity in Double-Bilayer Graphene. *Physical Review Letters*, 110(14):146803, apr 2013. ISSN 0031-9007. doi: 10.1103/PhysRevLett.110.146803. URL http://link.aps.org/doi/10.1103/PhysRevLett.110.146803.

[44] M Zarenia, A Perali, D Neilson, and F M Peeters. Enhancement of electron-hole superfluidity in double few-layer graphene. *Scientific reports*, 4:7319, jan 2014. ISSN 2045-2322. doi: 10.1038/srep07319. URL http://www.nature.com/srep/2014/141208/srep07319/full/srep07319.html.

[45] Bertrand I. Halperin. Theory of the quantized Hall conductance. *Helv. Phys. Acta 56:75–104*, 56:75–104, 1983.

[46] I. B. Spielman, J. P. Eisenstein, L. N. Pfeiffer, and K. W. West. Resonantly enhanced tunneling in a double layer quantum hall ferromagnet. *Physical Review Letters*, 84 (25):5808–5811, jun 2000. ISSN 00319007. doi: 10.1103/PhysRevLett.84.5808. URL http://link.aps.org/doi/10.1103/PhysRevLett.84.5808.

[47] M Kellogg, I B Spielman, J P Eisenstein, L N Pfeiffer, and K W West. Observation of quantized Hall drag in a strongly correlated bilayer electron system. *Physical review letters*, 88 (12):126804, mar 2002. ISSN 0031-9007. doi: 10.1103/PhysRevLett.88.126804. URL http://journals.aps.org/prl/abstract/10.1103/PhysRevLett.88.126804.

[48] D Nandi, a D K Finck, J P Eisenstein, L N Pfeiffer, and K W West. Exciton condensation and perfect Coulomb drag. *Nature*, 488(7412):481–4, aug 2012. ISSN 1476-4687. doi: 10.1038/nature11302. URL http://www.ncbi.nlm.nih.gov/pubmed/22914164.

[49] E Tutuc, M Shayegan, and D A Huse. Counterflow measurements in strongly correlated GaAs hole bilayers: Evidence for electron-hole pairing. *Phys. Rev. Lett.*, 93:36802, 2004. URL http://dx.doi.org/10.1103/PhysRevLett.93.036802.

[50] M Kellogg, J P Eisenstein, L N Pfeiffer, and K W West. Vanishing Hall resistance at high magnetic field in a double-layer two-dimensional electron system. *Phys. Rev. Lett.*, 93:36801, 2004. URL http://dx.doi.org/10.1103/PhysRevLett.93.036801.

[51] X. Feng, S. Zelakiewicz, H. Noh, T. Ragucci, T. Gramila, L. Pfeiffer, and K. West. Negative Electron Drag and Holelike Behavior in the Integer Quantum Hall Regime. *Physical Review Letters*, 81(15):3219–3222, oct 1998. ISSN 0031-9007. doi: 10.1103/PhysRevLett.81.3219. URL http://link.aps.org/doi/10.1103/PhysRevLett.81.3219.

[52] J. Lok, S. Kraus, M. Pohlt, W. Dietsche, K. von Klitzing, W. Wegscheider, and M. Bichler. Spin effects in the magnetodrag between double quantum wells. *Physical Review B*, 63(4): 041305, jan 2001. ISSN 0163-1829. doi: 10.1103/PhysRevB.63.041305. URL http://link.aps.org/doi/10.1103/PhysRevB.63.041305.

[53] Felix von Oppen, Steven Simon, and Ady Stern. Oscillating Sign of Drag in High Landau Levels. *Physical Review Letters*, 87(10):106803, aug 2001. ISSN 0031-9007. doi: 10.1103/PhysRevLett.87.106803. URL http://link.aps.org/doi/10.1103/PhysRevLett.87.106803.

[54] N P R Hill, J T Nicholls, E H Linfield, M Pepper, D a Ritchie, a R Hamilton, and G a C Jones. Frictional drag between parallel two-dimensional electron gases in a perpendicular magnetic field. *Journal of Physics: Condensed Matter*, 8(39):L557–L562, 1996. ISSN 0953-8984. doi: 10.1088/0953-8984/8/39/001. URL http://stacks.iop.org/0953-8984/8/i=39/a=001?key=crossref.693c77a893bf8cee9948ac71e358873c.

[55] Alex Kamenev and Y Oreg. Coulomb drag in normal metals and superconductors: Diagrammatic approach. *Physical Review B*, 52(10), 1995. URL http://journals.aps.org/prb/abstract/10.1103/PhysRevB.52.7516.

[56] K Flensberg, BYK Hu, AP Jauho, and JM Kinaret. Linear-response theory of Coulomb drag in coupled eletron systems. *Physical Review B*, 52(20), 1995. URL http://journals.aps.org/prb/abstract/10.1103/PhysRevB.52.14761.

[57] B. Narozhny and I. Aleiner. Mesoscopic Fluctuations of the Coulomb Drag. *Physical Review Letters*, 84(23):5383–5386, jun 2000. ISSN 0031-9007. doi: 10.1103/PhysRevLett.84.5383. URL http://link.aps.org/doi/10.1103/PhysRevLett.84.5383.

[58] B. Narozhny, I. Aleiner, and Ady Stern. Mesoscopic Fluctuations of the Coulomb Drag at ν=1/2. *Physical Review Letters*, 86(16):3610–3613, apr 2001. ISSN 0031-9007. doi: 10.1103/PhysRevLett.86.3610. URL http://link.aps.org/doi/10.1103/PhysRevLett.86.3610.

[59] Qijin Chen, Jelena Stajic, Shina Tan, and K. Levin. BCS–BEC crossover: From high temperature superconductors to ultracold superfluids. *Physics Reports*, 412(1):1–88, jun 2005. ISSN 0370-1573. doi: 10.1016/J.PHYSREP.2005.02.005. URL https://www.sciencedirect.com/science/article/pii/S0370157305001067.

[60] Mohit Randeria and Edward Taylor. Crossover from Bardeen-Cooper-Schrieffer to Bose-Einstein Condensation and the Unitary Fermi Gas. *Annual Review of Condensed Matter Physics*, 5(1):209–232, mar 2014. ISSN 1947-5454. doi: 10.1146/annurev-conmatphys-031113-133829. URL http://www.annualreviews.org/doi/10.1146/annurev-conmatphys-031113-133829.

[61] T. Bourdel, L. Khaykovich, J. Cubizolles, J. Zhang, F. Chevy, M. Teichmann, L. Tarruell, S. J. J. M. F. Kokkelmans, and C. Salomon. Experimental Study of the BEC-BCS Crossover Region in Lithium 6. *Physical Review Letters*, 93(5):050401, jul 2004. ISSN 0031-9007. doi: 10.1103/PhysRevLett.93.050401. URL https://link.aps.org/doi/10.1103/PhysRevLett.93.050401.

[62] C. A. Regal, M. Greiner, and D. S. Jin. Observation of Resonance Condensation of Fermionic Atom Pairs. *Physical Review Letters*, 92(4):040403, jan 2004. ISSN 0031-9007. doi: 10.1103/PhysRevLett.92.040403. URL https://link.aps.org/doi/10.1103/PhysRevLett.92.040403.

[63] M. Bartenstein, A. Altmeyer, S. Riedl, S. Jochim, C. Chin, J. Hecker Denschlag, and R. Grimm. Collective Excitations of a Degenerate Gas at the BEC-BCS Crossover. *Physical Review Letters*, 92(20):203201, may 2004. ISSN 0031-9007. doi: 10.1103/PhysRevLett.92.203201. URL https://link.aps.org/doi/10.1103/PhysRevLett.92.203201.

[64] M. W. Zwierlein, C. A. Stan, C. H. Schunck, S. M. F. Raupach, A. J. Kerman, and W. Ketterle. Condensation of Pairs of Fermionic Atoms near a Feshbach Resonance. *Physical Re-*

view Letters, 92(12):120403, mar 2004. ISSN 0031-9007. doi: 10.1103/PhysRevLett.92.120403. URL https://link.aps.org/doi/10.1103/PhysRevLett.92.120403.

[65] M. G. Ries, A. N. Wenz, G. Zürn, L. Bayha, I. Boettcher, D. Kedar, P. A. Murthy, M. Neidig, T. Lompe, and S. Jochim. Observation of pair condensation in the Quasi-2D BEC-BCS Crossover. *Physical Review Letters*, 114(23):230401, jun 2015. ISSN 10797114. doi: 10.1103/PhysRevLett.114.230401. URL https://link.aps.org/doi/10.1103/PhysRevLett.114.230401.

[66] M. Baldo, U. Lombardo, and P. Schuck. Deuteron formation in expanding nuclear matter from a strong coupling BCS approach. *Physical Review C*, 52(2):975–985, aug 1995. ISSN 0556-2813. doi: 10.1103/PhysRevC.52.975. URL https://link.aps.org/doi/10.1103/PhysRevC.52.975.

[67] Kazunori Itakura. Structure change of Cooper pairs in color superconductivity Crossover from BCS to BEC? *Nuclear Physics A*, 715:859c–862c, mar 2003. ISSN 0375-9474. doi: 10.1016/S0375-9474(02)01523-3. URL https://www.sciencedirect.com/science/article/pii/S0375947402015233.

[68] Lingjie Du, Xinwei Li, Wenkai Lou, Gerard Sullivan, Kai Chang, Junichiro Kono, and Rui-Rui Du. Evidence for a topological excitonic insulator in InAs/GaSb bilayers. *Nature Communications*, 8(1):1971, dec 2017. ISSN 2041-1723. doi: 10.1038/s41467-017-01988-1. URL http://www.nature.com/articles/s41467-017-01988-1.

[69] Z. Zhu, R. D. McDonald, A. Shekhter, B. J. Ramshaw, K. A. Modic, F. F. Balakirev, and N. Harrison. Magnetic field tuning of an excitonic insulator between the weak and strong coupling regimes in quantum limit graphite. *Scientific Reports*, 7(1):1733, dec 2017. ISSN 2045-2322. doi: 10.1038/s41598-017-01693-5. URL http://www.nature.com/articles/s41598-017-01693-5.

[70] D. Jérome, T. M. Rice, and W. Kohn. Excitonic Insulator. *Physical Review*, 158(2):462–475, jun 1967. ISSN 0031-899X. doi: 10.1103/PhysRev.158.462. URL https://link.aps.org/doi/10.1103/PhysRev.158.462.

[71] J.L. Tallon and J.W. Loram. The doping dependence of T* – what is the real high-Tc phase diagram? *Physica C: Superconductivity*, 349(1-2):53–68, jan 2001. ISSN 0921-4534. doi: 10.1016/S0921-4534(00)01524-0. URL https://www.sciencedirect.com/science/article/pii/S0921453400015240?via{%}3Dihub.

[72] Mohit Randeria, Ji Min Duan, and Lih Yir Shieh. Bound states, Cooper pairing, and Bose condensation in two dimensions. *Physical Review Letters*, 62(9):981–984, feb 1989. ISSN 00319007. doi: 10.1103/PhysRevLett.62.981. URL https://link.aps.org/doi/10.1103/PhysRevLett.62.981.

[73] Tom Timusk and Bryan Statt. The pseudogap in high-temperature superconductors: an experimental survey. Technical report, 1999. URL http://iopscience.iop.org/article/10.1088/0034-4885/62/1/002/pdf.

[74] Inti Sodemann, Itamar Kimchi, Chong Wang, and T. Senthil. Composite fermion duality for half-filled multicomponent Landau levels. *Physical Review B*, 95(8):085135, feb 2017. ISSN 2469-9950. doi: 10.1103/PhysRevB.95.085135. URL https://link.aps.org/doi/10.1103/PhysRevB.95.085135.

[75] Gunnar Möller, Steven H. Simon, and Edward H. Rezayi. Trial wave functions for ν=1/2+1/2 quantum Hall bilayers. *Physical Review B*, 79(12):125106, mar 2009. ISSN 1098-0121. doi: 10.1103/PhysRevB.79.125106. URL https://link.aps.org/doi/10.1103/PhysRevB.79.125106.

[76] Jason Alicea, Olexei I. Motrunich, G. Refael, and Matthew P. A. Fisher. Interlayer Coherent Composite Fermi Liquid Phase in Quantum Hall Bilayers. *Physical Review Letters*, 103(25):256403, dec 2009. ISSN 0031-9007. doi: 10.1103/PhysRevLett.103.256403. URL https://link.aps.org/doi/10.1103/PhysRevLett.103.256403.

[77] E. Tutuc and M. Shayegan. Interaction and disorder in bilayer counterflow transport at filling-factor one. *Physical Review B*, 72(8):081307, aug 2005. ISSN 1098-0121. doi: 10.1103/PhysRevB.72.081307. URL https://link.aps.org/doi/10.1103/PhysRevB.72.081307.

[78] E. Tutuc, M. Shayegan, and D. A. Huse. Counterflow measurements in strongly correlated GaAs hole bilayers: Evidence for electron-hole pairing. *Physical Review Letters*, 93(3):036802–1, jul 2004. ISSN 00319007. doi: 10.1103/PhysRevLett.93.036802. URL http://link.aps.org/doi/10.1103/PhysRevLett.93.036802.

[79] T. S. Lay, Y. W. Suen, H. C. Manoharan, X. Ying, M. B. Santos, and M. Shayegan. Anomalous temperature dependence of the correlated ν=1 quantum Hall effect in bilayer electron systems. *Physical Review B*, 50(23):17725–17728, dec 1994. ISSN 01631829. doi:

10.1103/PhysRevB.50.17725. URL https://link.aps.org/doi/10.1103/PhysRevB.50.17725.

[80] Xiaomeng Liu, Kenji Watanabe, Takashi Taniguchi, Bertrand I. Halperin, and Philip Kim. Quantum Hall drag of exciton condensate in graphene. *Nature Physics*, 13(8):746–750, may 2017. ISSN 17452481. doi: 10.1038/NPHYS4116. URL http://www.nature.com/doifinder/10.1038/nphys4116.

[81] S. M. Girvin and A. H. MacDonald. Multicomponent Quantum Hall Systems: The Sum of Their Parts and More. In *Perspectives in Quantum Hall Effects*, pages 161–224. Wiley-VCH Verlag GmbH, Weinheim, Germany, 2007. ISBN 9783527617258. doi: 10.1002/9783527617258.ch5. URL http://doi.wiley.com/10.1002/9783527617258.ch5http://dx.doi.org/10.1002/9783527617258.ch5{%}5Cnhttp://onlinelibrary.wiley.com/doi/10.1002/9783527617258.ch5/summary.

[82] Steven M Girvin. The Kosterlitz-Thouless Phase Transition. *Boulder School Lecture*, pages 1–15, 2000. ISSN 1079-7114. URL http://boulderschool.yale.edu/sites/default/files/files/kosterlitz-thouless.pdf.

[83] B. I. Halperin and David R. Nelson. Resistive transition in superconducting films. *Journal of Low Temperature Physics*, 36(5-6):599–616, sep 1979. ISSN 0022-2291. doi: 10.1007/BF00116988. URL http://link.springer.com/10.1007/BF00116988.

[84] D. C. Tsui, H. L. Stormer, and A. C. Gossard. Two-dimensional magnetotransport in the extreme quantum limit. *Physical Review Letters*, 48(22):1559–1562, may 1982. ISSN 00319007. doi: 10.1103/PhysRevLett.48.1559. URL https://link.aps.org/doi/10.1103/PhysRevLett.48.1559.

[85] R. B. Laughlin. Anomalous quantum Hall effect: An incompressible quantum fluid with fractionally charged excitations. *Physical Review Letters*, 50(18):1395–1398, may 1983. ISSN 00319007. doi: 10.1103/PhysRevLett.50.1395. URL https://link.aps.org/doi/10.1103/PhysRevLett.50.1395.

[86] Tapash Chakraborty and Pekka Pietiläinen. Fractional quantum hall effect at half-filled landau level in a multiple-layer electron system. *Physical Review Letters*, 59(24):2784–2787, 1987. ISSN 00319007. doi: 10.1103/PhysRevLett.59.2784. URL https://arxiv.org/pdf/1502.01340.pdf.

[87] Jainendra Jain. *Composite fermions*, volume 9780521862. Cambridge University Press, Cambridge, 2007. ISBN 9780511607561. doi: 10.1017/CBO9780511607561. URL http://ebooks.cambridge.org/ref/id/CBO9780511607561.

[88] J. K. Jain. Composite-fermion approach for the fractional quantum Hall effect. *Physical Review Letters*, 63(2):199–202, jul 1989. ISSN 00319007. doi: 10.1103/PhysRevLett.63.199. URL https://link.aps.org/doi/10.1103/PhysRevLett.63.199.

[89] B. I. Halperin. Statistics of Quasiparticles and the Hierarchy of Fractional Quantized Hall States. *Physical Review Letters*, 52(18):1583–1586, apr 1984. ISSN 0031-9007. doi: 10.1103/PhysRevLett.52.1583. URL https://link.aps.org/doi/10.1103/PhysRevLett.52.1583.

[90] D. Yoshioka, A. H. MacDonald, and S. M. Girvin. Fractional quantum Hall effect in two-layered systems. *Physical Review B*, 39(3):1932–1935, jan 1989. ISSN 01631829. doi: 10.1103/PhysRevB.39.1932. URL https://link.aps.org/doi/10.1103/PhysRevB.39.1932.

[91] V. W. Scarola and J. K. Jain. Phase diagram of bilayer composite fermion states. *Physical Review B - Condensed Matter and Materials Physics*, 64(8):853131–8531310, aug 2001. ISSN 01631829. doi: 10.1103/PhysRevB.64.085313. URL https://link.aps.org/doi/10.1103/PhysRevB.64.085313.

[92] Maissam Barkeshli and Xiao-Gang Wen. Non-Abelian two-component fractional quantum Hall states. *Physical Review B*, 82(23):233301, 2010. ISSN 1098-0121. doi: 10.1103/PhysRevB.82.233301. URL https://journals.aps.org/prb/pdf/10.1103/PhysRevB.82.233301https://link.aps.org/doi/10.1103/PhysRevB.82.233301.

[93] Scott Geraedts, Michael P. Zaletel, Zlatko Papić, and Roger S. K. Mong. Competing Abelian and non-Abelian topological orders in $\nu = 1/3 + 1/3$ quantum Hall bilayers. *Physical Review B*, 91(20):205139, may 2015. ISSN 1098-0121. doi: 10.1103/PhysRevB.91.205139. URL https://link.aps.org/doi/10.1103/PhysRevB.91.205139.

[94] Y. W. Suen, L. W. Engel, M. B. Santos, M. Shayegan, and D. C. Tsui. Observation of a =1/2 fractional quantum Hall state in a double-layer electron system. *Physical Review Letters*, 68 (9):1379–1382, mar 1992. ISSN 00319007. doi: 10.1103/PhysRevLett.68.1379. URL http://link.aps.org/doi/10.1103/PhysRevLett.68.1379.

[95] J. P. Eisenstein, G. S. Boebinger, L. N. Pfeiffer, K. W. West, and Song He. New fractional quantum Hall state in double-layer two-dimensional electron systems. *Physical Review Letters*, 68(9):1383–1386, mar 1992. ISSN 00319007. doi: 10.1103/PhysRevLett.68.1383. URL http://link.aps.org/doi/10.1103/PhysRevLett.68.1383.

[96] Song He, S Das Sarma, and X. C. Xie. Quantized Hall effect and quantum phase transitions in coupled two-layer electron systems. *Physical Review B*, 47(8):4394–4412, 1993. ISSN 01631829. doi: 10.1103/PhysRevB.47.4394. URL https://journals.aps.org/prb/pdf/10.1103/PhysRevB.47.4394.

[97] Ana Lopez and Eduardo Fradkin. Fractional quantum Hall effect and Chern-Simons gauge theories. *Physical Review B*, 44(10):5246–5262, sep 1991. ISSN 0163-1829. doi: 10.1103/PhysRevB.44.5246. URL https://link.aps.org/doi/10.1103/PhysRevB.44.5246.

[98] Bertrand I. Halperin, Patrick A. Lee, and Nicholas Read. Theory of the half filled Landau level. *Phys. Rev. B*, 47(12):7312–7343, mar 1993. ISSN 0163-1829. doi: 10.1103/PhysRevB.47.7312. URL https://link.aps.org/doi/10.1103/PhysRevB.47.7312.

[99] N. Read and Dmitry Green. Paired states of fermions in two dimensions with breaking of parity and time-reversal symmetries and the fractional quantum Hall effect. *Physical Review B - Condensed Matter and Materials Physics*, 61(15):10267–10297, apr 2000. ISSN 1550235X. doi: 10.1103/PhysRevB.61.10267. URL https://link.aps.org/doi/10.1103/PhysRevB.61.10267.

[100] Fereshte Ghahari, Hong-Yi Xie, Takashi Taniguchi, Kenji Watanabe, Matthew S. Foster, and Philip Kim. Enhanced Thermoelectric Power in Graphene: Violation of the Mott Relation by Inelastic Scattering. *Physical Review Letters*, 116(13):136802, mar 2016. ISSN 0031-9007. doi: 10.1103/PhysRevLett.116.136802. URL https://link.aps.org/doi/10.1103/PhysRevLett.116.136802.